NOTICE

The quality of this microform is heavily dependent upon the quality of the original thesis submitted for microfilming. Every effort has been made to ensure the highest quality of reproduction possible.

If pages are missing, contact the university which granted the degree.

Some pages may have indistinct print especially if the original pages were typed with a poor typewriter ribbon or if the university sent us an inferior photocopy.

Reproduction in full or in part of this microform is governed by the Canadian Copyright Act, R.S.C. 1970, c. C-30, and subsequent amendments.

AVIS

La qualité de cette microforme dépend grandement de la qualité de la thèse soumise au microfilmage. Nous avons tout fait pour assurer une qualité supérieure de reproduction.

S'il manque des pages, veuillez communiquer avec l'université qui a conféré le grade.

La qualité d'impression de certaines pages peut laisser à désirer, surtout si les pages originales ont été dactylographiées à l'aide d'un ruban usé ou si l'université nous a fait parvenir une photocopie de qualité inférieure.

La reproduction, même partielle, de cette microforme est soumise à la Loi canadienne sur le droit d'auteur, SRC 1970, c. C-30, et ses amendements subséquents.

Timing Recovery for Continuous Phase Modulation Transmitted over Fast Flat-Fading Channels

by

François Patenaude

A thesis submitted to the
School of Graduate Studies and Research
in partial fulfillment of the requirements for the degree of

Master of Applied Science

Ottawa-Carleton Institute for Electrical Engineering

Department of Electrical Engineering
Faculty of Engineering
University of Ottawa

NOTICE

The quality of this microform is heavily dependent upon the quality of the original thesis submitted for microfilming. Every effort has been made to ensure the highest quality of reproduction possible.

If pages are missing, contact the university which granted the degree.

Some pages may have indistinct print especially if the original pages were typed with a poor typewriter ribbon or if the university sent us an inferior photocopy.

AVIS

La qualité de cette microforme dépend grandement de la qualité de la thèse soumise au microfilmage. Nous avons tout fait pour assurer une qualité supérieure de reproduction.

S'il manque des pages, veuillez communiquer avec l'université qui a conféré le grade.

La qualité d'impression de certaines pages peut laisser à désirer, surtout si les pages originales ont été dactylographiées à l'aide d'un ruban usé ou si l'université nous a fait parvenir une photocopie de qualité inférieure.

ISBN 0-315-60579-0

UNIVERSITÉ D'OTTAWA
UNIVERSITY OF OTTAWA

A mes parents,
en remerciement pour l'éducation
que vous m'avez donnée.

On ne connaît que les choses que l'on apprivoise, dit le renard. Les hommes n'ont plus le temps de rien connaître. Ils achètent des choses toute faites chez les marchands. Mais comme il n'existe point de marchand d'amis, les hommes n'ont plus d'amis. Si tu veux un ami, apprivoise-moi !

Saint-Exupéry

ABSTRACT

The problem of deriving symbol synchronization information from the received signal for a class of bandwidth efficient continuous phase modulation (CPM) schemes transmitted over a fast flat-fading channel is studied. The modulation class considered is M-ary CPM with a modulation index $h=1/M$. A particular synchronizer structure which generates a tone at the symbol rate in a manner which automatically cancels the fading phase effects is proposed and analyzed in detail. The practical aspects of implementing this synchronizer using digital signal processing methods are discussed. Finally, simulation results showing the root mean square jitter produced by this synchronizer for a few well-known cases of modulation and fading channel parameters are presented to illustrate the performances of the system.

ACKNOWLEDGMENTS

My first grateful thanks are dedicated to my two supervisors, Dr. J. H. Lodge and Dr. P. Galko. Their countless comments, remarks, and observations have been an inestimable source of learning. The experience acquired during the elaboration of this thesis is perhaps the most appreciated input from them. I am also very grateful to Dr. T. Aboulnasr who welcomed me at the University of Ottawa and who supported me during my first year. This thesis would not have been possible either without the help and corrections to the English provided by my supervisors.

I am deeply indebted to the following institutions for their financial and technical support:

- the Natural Sciences and Engineering Research Council (NSERC),
- the Communications Research Centre (CRC),
- les Fonds pour la Formation de Chercheurs et l'Aide à la Recherche (FCAR),
- the School of Graduate Studies and Research.

Finally, the encouragements received from my friends, Roseline Laplante, Guy Beaulieu and Yvon Thibaudeau have been extremely motivating.

TABLE of CONTENTS

LIST of FIGURES

LIST of TABLES

LIST of ACRONYMS

AWGN: Additive white Gaussian noise

CPM: Continuous phase modulation

DFT: Discrete Fourier transform

FFF: Fast flat-fading

FM: Frequency modulation

IDFT: Inverse DFT

I-Q: Inphase-quadrature

ISI: Inter-symbol interference

N3CR: Nyquist III cosine rolloff

NBPF: Narrow bandpass filter

MAP: Maximum a *Posteriori*

MLSE: Maximum likelihood sequence estimation

MSK: Minimum shift keying

PAM: Pulse amplitude modulation

PM: Phase modulation

PSD: Power spectral density

RMS: Root mean square

SNR: Signal-to-noise ratio

TSNR: Tone to self-noise ratio

US: Uncorrelated scattering

WSS: Wide-sense stationary

WSSUS: Wide-sense stationary uncorrelated scattering

Chapter 1

INTRODUCTION

The evolution of communications over the last three decades has given birth to a tremendous varieties of modulation schemes, signal processing techniques and system configurations. Associated with this progress is the diversity of applications developed over the years to fulfill the growing demand for communications all over the world. At the same time, changes in the economics of digital technologies and the flexibility inherent to discrete systems have lead to a pronounced shift towards digital communication systems.

Fortunately, the mathematical foundation for digital communication had been established by Shannon [1]-[3] in the late 40's. This provided an understanding of the fundamental limitations on the performance of digital communication systems and through this some of the goals in the design of these systems. A great deal of effort has been expended to find means of approaching the limits set by Shannon and others for efficient communications. The results of this extensive effort can be seen today in the assortment of digital systems available to transmit and receive information. Among the most popular, are the digital cable telephone networks, the line-of-sight radio systems, the digital satellite communication systems, and the land-mobile radio systems. This thesis deals primarily with a difficulty found in digital communications, especially here in digital land-mobile and satellite-mobile radio systems, and specifically with the practical problem of determining timing information from the received signal which is necessary for successful recovery of the data. The introduction presents the three major components related to the thesis i.e., the fading channel, the modulation scheme, and the synchronization problem.

In [4], Lee defines mobile radio communications as a "radio communication link between two terminals of which one or both are in motion or halted at unspecified locations and of which one may actually be a fixed terminal such as a base station". This definition applies to satellite communications, and even more so to the planned systems for mobile-satellite communications [5][6]. Mobile communications is in general associated with time-varying channels. The radio transmission system must be designed to insure reliable transfer of information despite the channel variations. The first step toward understanding the mobile radio channel, is to examine a few basic characteristic of such channels.

1.1 Mobile Radio Channel

The mobile radio channel is characterized by a time-varying structure inherent to many non-man made propagation medium. The fluctuations are called short-term changes if the duration is much shorter or in the order of the shortest period of interest to the communication application (typically the symbol period). Long-term changes occur relatively slowly and relate to time periods of an hour, a day, a month or even seasonal.

To explain the behavior of the channel, a theory based on unmodulated radio frequency carriers affected by multipath propagation has been constructed. Because of geography, the signal propagation between the transmitting and receiving points usually occurs over several different paths. Each signal path is characterized by an attenuation, a phase change and a delay which depend on the nature of the scatterers and the path length. Therefore, the received signal can be seen as a sum of a finite number of attenuated and shifted version of the transmitted signal. A small change in a path length relative to the carrier wavelength will result in a delay change that will produce a significant carrier phase change for that component of the received signal. Since the length of the paths and the scatterers vary randomly, the received signal changes randomly in amplitude and in radio frequency phase. Therefore the general approach taken is to characterize the time-varying multipath channel statistically. When the number of paths is large and all of comparable magnitude, the received signal

envelope can be shown to follow (with the direct path) a Rician probability density function and the radio frequency carrier-phase a known probability density function [8]. The number of paths necessary (no line-of-sight path) to observe a close similarity for the envelope and phase with the above distribution is as few as six sine waves with independently fluctuating random phase. In certain conditions, the delays between the paths are small and it is appropriate to model the channel as a multiplicative noise process. For engineering purposes, the Rician statistics are expected to be a very good approximation for the resulting envelope fluctuations under multipath propagation. These statistics correspond to the short term fading mentioned above. The resulting envelope mean is associated with the long-term fading and is modeled by a random variable having a log-normal probability density function (log-normal shadowing) [10]. In this thesis, only the short-term fading is considered for the analysis and the design. Rayleigh (a special case of Rician) statistics are assumed to characterize the envelope statistics throughout most of this thesis.

Given the channel characteristics, a natural question to ask is what modulation scheme is most appropriate in this environment. We shall briefly consider this question next.

1.2 Modulation

Digital modulation techniques have also found many applications in mobile communications in the last few years. Transmission through the mobile radio channel results in distortion of the transmitted signal in both the amplitude and the phase, making some digital schemes more attractive than others. Furthermore, nonlinearities are often encountered in mobile transmitter equipment necessitated by the need for power efficiency and physical constraints. For these reasons, it is recognized that constant envelope modulation schemes are highly suitable for this kind of application. Thus schemes like M-ary frequency shift keying are candidates for use in time-varying nonlinear channels. Another practical constraint in mobile communications arises from the difficulty in designing a good carrier recovery circuit because of the rapid carrier-phase changes due to multipath. Non-coherent systems represent a potential solution to this problem at the expense of some degradation in

the probability of error [15]. For example, in the Advanced Mobile Phone Service system, binary frequency shift keying with discriminator detection [7][10] is used. However because of the increasing demand and interest in mobile communications, new bandwidth efficient constant envelope modulation schemes are needed which have higher transmission capacity.

One approach to decrease the signal bandwidth is by the use of digital frequency modulation with continuous phase. An important class of such modulation techniques is the class of techniques known as continuous phase modulation (CPM) [11],[17],[18]. These techniques are generally instances of nonlinear modulation with the properties of generating signals with a constant-envelope and continuous-phase. The average power spectrum of several CPM signals have been shown to have good main lobe characteristics as well as acceptable small sidelobes to minimize co-channel interference [12]. CPM signals are often classified according to the pulse shape used to smooth the frequency or/and phase transitions. Nyquist proposed three criteria [13] for distortionless baseband transmission. The pulse shapes resulting from these criteria of importance in the context of CPM are those -tisfying Nyquist third criterion [21] which have interesting properties similar to Nyquist I criterion in linear modulation. Because of this interesting property, attention will be paid to CPM Nyquist III pulse shaping in the context of a fading channel.

In order for successful detection to occur, any digital CPM detector has to acquire and maintain symbol synchronization This thesis will investigate the synchronization problem in the given signal environment.

1.3 Synchronization

Applied to digital communication, synchronization can be defined as the alignment in time of frequency and time. The hierarchy of synchronization levels is usually divided in four categories: network, frame, symbol and carrier synchronization. Network synchronization is concerned with system access time, and frequency-time distribution among various subsystems. The format under which the

data bit stream is transmitted is called a block, a packet, or a frame. It is of importance to know when the frame is beginning and ending so that proper reconstruction of the message is achieved. Frame synchronization addresses this problem. Network and frame synchronization problems are usually solved by multiplexing messages, words or bits solely for synchronization purposes. The next level is symbol synchronization and the problem is basically to determine the instants in time when the modulation may change states. From the implementation point of view, a timing signal is required to convert the continuous-time signal into a discrete-time sequence of data symbols. The last level is carrier-phase synchronization where restoration of the carrier in frequency and phase is carried out from a carrier-suppressed waveform. The restoration of the carrier-phase is not always needed. For example the non-coherent detection techniques mentioned earlier for the fading channels do not need phase alignment of the carrier.

This thesis is concerned with the problem of symbol synchronization. More specifically, we are concerned with the "self-synchronization problem" where we try to recover symbol timing directly from the received data-bearing signal (as opposed to data-aided synchronization recovery techniques or the use of a separate synchronization signal). Synchronization recovery is usually handled in two phases: in the first instance we try to acquire the initial synchronization "lock" in what is termed the "acquisition mode", which is followed by procedures which try to refine and maintain the synchronization lock in the "tracking mode". Acquisition of synchronization must be performed at the start of a transmission and whenever the system loses lock. It is usually accomplished with the aid of a preamble of a specific known pattern of symbols to speed the process of acquiring lock and thereby improve the system's efficiency. In tracking mode, the task is different in that the synchronization recovery system is only trying to follow the small and slow variations that occur in the symbol timing clock. The discussion of synchronization recovery here is limited to a discussion of synchronization recovery in tracking mode.

1.4 Objectives and Organization

The task of determining optimum timing schemes is a very difficult one and is not pursued at length in this thesis. Instead most of the discussion on synchronizers here is concerned with the analysis of a particular synchronizer structure which seems to posses a variety of good properties for the modulation schemes of interest in this thesis. These modulation schemes are those of CPM with modulation index of $h=1/M$ for $M=2$, 4, and 8 specifically. This synchronizer represents a modification to an approach taken by de Buda [14]. The aim of this thesis is to consider these schemes in the context of a fast flat-fading channel with additive white Gaussian noise and relative to other synchronizers, and to characterize the synchronizer's performance. It is shown that under appropriate conditions the synchronizer will recover symbol timing with errors which are only a small fraction of the symbol period.

The discussion in this thesis is organized in a further four chapters. Chapter 2 presents a detailed background discussion of the channel characteristics, modulation involved and the potential of the different CPM schemes for self-synchronization. Chapter 3 then discusses the principles of operation of the proposed synchronizer in the envisaged environment, its parameters, and its analysis. Chapter 4 then provides some simulation results on the performance of the synchronizer. Finally, Chapter 5 concludes with the results achievable for the defined system and indicates some improvements that may ameliorate the overall performance. Future work in the domain of digital mobile communication is also discussed. ■

Chapter 2

SYSTEM DESCRIPTION

After the qualitative discussion of Chapter 1, it is important to describe formally the mobile radio channel, the modulation scheme and the symbol synchronization problem. The sections describing the channel and the modulation scheme of interest are intended mainly as background theory while the section on symbol synchronization contains some results on the power available for timing purposes for several types of CPM signal. These results highlight the relationship between the power available for timing and certain general parameters specifying the CPM signals. First the signal representation, used throughout this thesis, will be introduced.

2.1 Representation of Bandpass Signals

In the analysis of communication signals, real-valued bandpass processes are often described in terms other than their ordinary time-domain form. With the appropriate choice of representation of these signals, the analysis of the signals often simplifies and becomes more general. A very useful representation expresses the signal in terms of its lowpass equivalent. It is appropriate to briefly discuss this representation since extensive use of it is made throughout the thesis.

2.1.1 Equivalent Lowpass Representation

Consider the real-valued bandpass signal $s(t)$ bandlimited to $(f_0 - W/2, f_0 + W/2)$. This signal can always be written as

$$s(t) = \sqrt{2}\ \tilde{u}(t) \cos\left[2\pi f_0 t + \theta(t)\right], \tag{2.1.1}$$

where the two lowpass signals $\bar{u}(t)$ and $\theta(t)$ are the envelope and phase of $s(t)$ respectively, with f_0 the carrier frequency. The signal $s(t)$ is called a narrowband bandpass signal, or simply a bandpass signal if the condition $W \ll f_0$ is met. It is assumed that this condition is true for many of the signals treated in this thesis. A second representation can be obtained by expansion of the cosine in (2.1.1), leading to

$$\begin{aligned} s(t) &= \sqrt{2}\ \bar{u}(t) \cos\theta(t) \cos 2\pi f_0 t - \sqrt{2}\ \bar{u}(t) \sin\theta(t) \sin 2\pi f_0 t \\ &= \sqrt{2}\ u_I(t) \cos 2\pi f_0 t - \sqrt{2}\ u_Q(t) \sin 2\pi f_0 t, \end{aligned} \tag{2.1.2}$$

where $u_I(t)=\bar{u}(t) \cos\theta(t)$ and $u_Q(t)=\bar{u}(t) \sin\theta(t)$. Now, defining

$$u(t) = u_I(t) + j u_Q(t) \tag{2.1.3}$$

$$= \bar{u}(t)\, e^{j\theta(t)}, \tag{2.1.4}$$

where $\bar{u}(t)$ is the module of $u(t)$, and $\theta(t)=\arg[u(t)]$. It is easy to show [15] that

$$s(t) = \sqrt{2}\ \Re\Big[\ u(t)\ e^{j2\pi f_0 t}\ \Big], \tag{2.1.5}$$

where $u(t)$ is called the complex envelope or equivalent lowpass representation of $s(t)$ with inphase component $u_I(t)$ and quadrature component $u_Q(t)$, and $\Re[\cdot]$ denotes the real part of $[\cdot]$. It is important to note that the power of $u(t)$ is double that of $s(t)$. The three representations (2.1.1), (2.1.2) and (2.1.5) can be used either for deterministic signals or sample functions of a stochastic process. In the second case, it is useful to relate the second order statistics of the bandpass stochastic process to those of its equivalent lowpass form. Let $s(t)$ be a real-valued bandpass stationary stochastic process with zero mean; then $u_I(t)$ and $u_Q(t)$ are also zero mean. With the assumptions of stationarity and zero mean, it can be shown [15] that

$$R_{ss}(\tau) = \Re\Big[\ R_{uu}(\tau)\ e^{j2\pi f_0 \tau}\ \Big], \tag{2.1.6}$$

where $R_{ss}(\tau)$ and $R_{uu}(\tau)$ are the autocorrelation functions of the real-valued signal $s(t)$ and the complex envelope $u(t)$, respectively. Thus, the autocorrelation of a bandpass process can be represented in a complex envelope form also. This result implies that the power spectral density (PSD) function of $s(t)$ is related to the PSD of its complex envelope $u(t)$ by [15]

$$S_{ss}(f) = \tfrac{1}{2}\left[\, S_{uu}(f-f_0) + S_{uu}(-f-f_0) \,\right], \tag{2.1.7}$$

because of the Fourier transform pair between the autocorrelation $R(\tau)$ and the PSD $S(f)$, namely

$$R(\tau) = \int_{-\infty}^{\infty} S(f)\, e^{j2\pi f\tau}\, df \tag{2.1.8a}$$

$$S(f) = \int_{-\infty}^{\infty} R(\tau)\, e^{-j2\pi f\tau}\, d\tau. \tag{2.1.8b}$$

Now, given that the autocorrelation and PSD of the equivalent lowpass process $u(t)$ are known, it is possible to determine the autocorrelation and PSD of the response $v(t)$ of a deterministic linear time-invariant system with impulse response $c(t)$ to such an input process. Fig. 2.1 illustrates the situation with $C(f)$ the Fourier transform of $c(\tau)$. Using basic linear system and stochastic process theory, it can be shown that

$$m_v = m_u\, C(0), \tag{2.1.9}$$

$$R_{vv}(\tau) = c(\tau) \star c^*(-\tau) \star R_{uu}(\tau), \tag{2.1.10}$$

$$S_{vv}(f) = S_{uu}(f)\, |C(f)|^2, \tag{2.1.11}$$

where $\star$ denotes convolution and $*$ denotes complex conjugation. By looking at (2.1.11) it can be seen that the PSD of a random process can be altered in a predetermined way using a linear filter. If the process $u(t)$ is Gaussian, then it is found that $v(t)$ is also Gaussian. We shall make use of this important property in the system analysis.

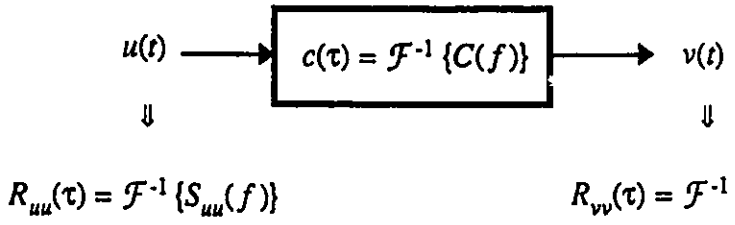

Fig. 2.1. Linear transformation of a random process.

2.1.2 Probability Density Function for Equivalent Lowpass Stochastic Processes

The random signals encountered in this thesis originate from two groups of processes: random modulation and noise. Random modulation processes result from modulating a carrier with a random signal which in turn depends on "random" data. While the "random" data probability density function might be known, the resulting modulated signal probability density function at time $t \in [0,T]$ is not trivial to find in general. Often the modulating signal statistics are partly characterized in terms of the autocorrelation function or PSD, particularly in the case considered here where the modulation scheme is nonlinear. For noise processes which are assumed to be stationary, the probability density function is a simple way to represent the random signal statistics. The probability density function of a real Gaussian random variable X is given by

$$p_X(x) = \frac{1}{\sqrt{2\pi}\,\sigma}\, e^{\frac{-(x-m)^2}{2\sigma^2}} \tag{2.1.12}$$

where m is the mean and σ^2 the variance of X. Now, suppose that X is a random variable describing the state of a given real Gaussian random process $x(t)$ at time t. Then we can define a complex Gaussian random process

$$z(t) = z_I(t) + j z_Q(t) \tag{2.1.13}$$

where $z_I(t)$ and $z_Q(t)$ are real and independent stochastic processes associated to the real independent Gaussian random processes $Z_I(t)$, $Z_Q(t)$ with mean m and variance σ^2 at time t. The joint probability density function $p_{Z_I Z_Q}(z_I, z_Q)$ is, of course, Gaussian and is often used to represent complex Gaussian noise. We can also define a real-valued scalar probability density function of the complex random variable Z to describe the complex random process $z(t)$, namely

$$p_Z(z) = \frac{1}{\pi\sigma_z^2}\, e^{\frac{-|z-m_z|^2}{\sigma_z^2}}. \tag{2.1.14}$$

This probability density function also has a Gaussian shape but with mean $m_z = \sqrt{2}m\, e^{j\pi/4}$ and variance $\sigma_z^2 = 2\sigma^2$. The complex Gaussian process can be expressed in terms of a random envelope $\Xi(t)$

and a random phase $\theta(t)$ as seen in the previous section. The joint probability density function of the modulus $\bar{z}(t)$ and the phase $\theta(t)$ is given [45] by

$$p_{\bar{z}\theta}(\bar{z},\theta) = \begin{cases} \frac{\bar{z}}{\pi\sigma_z^2} e^{\frac{-(\bar{z}^2+|m_z|^2)}{\sigma_z^2}} e^{\frac{2|m_z|\bar{z}\cos(\theta-\pi/4)}{\sigma_z^2}}, & \bar{z} \geq 0 \\ & 0 \leq \theta \leq 2\pi; \\ 0, & \text{elsewhere,} \end{cases} \tag{2.1.15}$$

where m_z and σ_z^2 are the mean and variance of $z(t)$ respectively. The marginal probability density function of $\bar{z}$ and θ when $m_z=0$ are known to be given by Rayleigh and uniform densities

$$p_{\bar{z}}(\bar{z}) = \begin{cases} \frac{2\bar{z}}{\sigma_z^2} e^{\frac{-\bar{z}^2}{\sigma_z^2}}, & \bar{z} \geq 0; \\ 0, & \text{elsewhere;} \end{cases} \tag{2.1.16}$$

$$p_\theta(\theta) = \begin{cases} 1/2\pi, & 0 \leq \theta \leq 2\pi; \\ 0, & \text{elsewhere.} \end{cases} \tag{2.1.17}$$

Furthermore $\bar{z}$ and θ are independent and thus the joint probability density function $p_{\bar{z}\theta}(\bar{z},\theta)$ is simply the product of $p_{\bar{z}}(\bar{z})$ and $p_\theta(\theta)$. More generally, the probability density function of $\bar{z}$ is found to be given by a Rician distribution

$$p_{\bar{z}}(\bar{z}) = \begin{cases} \frac{2\bar{z}}{\sigma_z^2} e^{\frac{-(\bar{z}^2+|m_z|^2)}{\sigma_z^2}} I_0\left(\frac{2|m_z|\bar{z}}{\sigma_z^2}\right), & \bar{z} \geq 0; \\ 0, & \text{elsewhere,} \end{cases} \tag{2.1.18}$$

and θ is found to have a distribution

$$p_\theta(\theta) = \begin{cases} \frac{1}{2\pi}\, e^{\frac{-|m_z|^2[1+\sin^2(\theta-\pi/4)]}{2\sigma_z^2}}\, D_{-2}\Big(-\frac{\sqrt{2}|m_z|}{\sigma_z}\cos(\theta-\pi/4)\Big), & 0 \le \theta \le 2\pi; \\ 0, & \text{elsewhere,} \end{cases} \tag{2.1.19}$$

where $I_0(\cdot)$ is the zeroth-order modified Bessel function of the first kind and $D_{-2}(\cdot)$ is the parabolic cylinder function [45]. The envelope and the phase of $z(t)$ are no longer independent. Thus the study of non-zero mean complex Gaussian process is significantly more involved mathematically than the zero mean case.

2.2 Fading and Dispersive Radio Channels

The discussion in §1.1 on mobile channels introduced the reader to the kind of channel of interest here and presented a few general concepts. The same concepts will now be described in a more formal way to facilitate quantitative evaluation of the distortion associated with the channel. The description is based on a structural representation of the impulse response [9][15].

2.2.1 Channel Impulse Response and Channel Transfer Function

The goal here is to describe a model for the channel in a way that will permit the determination of the response of the channel to a known transmitted signal, defined in the time or frequency domain. A classical way to model a radio channel is to associate with it a linear time-varying filter with a randomly time-varying impulse response and/or random transfer function. This approach leads to a statistical characterization based on the properties of an operator representing the channel.

Consider the transmitted signal

$$s(t) = \sqrt{2}\,\Re\Big[\, u(t)\, e^{j2\pi f_0 t}\,\Big]. \tag{2.2.1}$$

Suppose that under multipath phenomena, the received signal is composed of attenuated and delayed

versions of the transmitted signal. Then

$$r'(t) = \sum_n \rho_n(t)\, s(t-\tau_n-t_0), \tag{2.2.2}$$

where $\rho_n(t)$ and τ_n are real random variables representing the attenuation and delay associated with the nth path and t_0 is some convenient representative value of the total propagation time. By a shift in the time origin for the received signal it can be assumed that t_0 is zero without loss of generality. Under the assumptions of §2.1 and substituting (2.2.1) into (2.2.2), $r'(t)$ can then be written

$$r'(t) = \sqrt{2}\,\Re\left[\, v'(t)\, e^{j2\pi f_0 t}\,\right] = \sqrt{2}\,\Re\left\{\left(\sum_n \rho_n(t)\, u(t-\tau_n)\, e^{-j2\pi f_0 \tau_n}\right) e^{j2\pi f_0 t}\right\}. \tag{2.2.3}$$

The expression (2.2.3) implies distinguishable paths corresponding to very distinct scatterers. In several actual channels of interest, the scatters (paths) are not distinguishable and it is more appropriate to think about a continuously distributed scattering. With this approach a sum of random processes becomes a single random process whose complex envelope signal can be written as

$$v'(t) = \int_{-\infty}^{\infty} \rho(\tau;t)\, u(t-\tau)\, e^{-j2\pi f_0 \tau}\, d\tau, \tag{2.2.4}$$

where $\rho(\tau;t)$ is the complex attenuation at delay τ and time t. Note from (2.2.4) that the discrete multipath components have been transformed into continuous multipath components in the τ variable. This explains why the attenuation is now τ dependent. It is easy to see that the complex envelope impulse response[1] of the channel is

$$c(\tau;t) = \rho(\tau;t)\, e^{-j2\pi f_0 \tau}. \tag{2.2.5}$$

The dependence of $c(\tau;t)$ on τ represents the usual filter response variable while the t dependence indicates that the impulse response changes with time. From the statistical point of view, this impulse response is often modeled as a complex-valued Gaussian random process in the t variable under the assumption that a sufficiently large number of paths contribute to the received signal in (2.2.2) [9]. From §2.1.2, if $c(\tau;t)$ is a zero mean complex-valued Gaussian process, then its envelope is

[1] Note here that the impulse response concept is used in a time-varying environment which is more general than the notion encountered for the time-invariant systems.

Rayleigh distributed and its phase has a uniform distribution in the interval $[0,2\pi]$. When $c(\tau;t)$ is non-zero mean, then the envelope of $c(\tau;t)$ (in the t variable) has a Rician probability density function and its phase distribution follows (2.1.19). The Fourier transform of $c(\tau;t)$ in the τ variable represents the equivalent lowpass transfer function[2] of the bandpass channel and can also be modeled as a complex-valued Gaussian process because of the linear property of the Fourier transform. Therefore,

$$C(f;t) = \int_{-\infty}^{\infty} c(\tau;t)\ e^{-j2\pi f\tau}\ d\tau \tag{2.2.6}$$

and in $C(f;t)$, f represents the offset from the nominal band center frequency f_0 and t again indicates that the equivalent lowpass transfer function is time-varying.

2.2.2 Autocorrelation Function of the Complex Envelope Impulse Response and Transfer Function

$C(f;t)$ and $c(\tau;t)$ are two stochastic processes defined over two-dimensional parameter spaces. It is of interest to determined the autocorrelation function of those two processes in an attempt to characterize the channel. First, let the space-time autocorrelation function be defined as

$$R_{cc}(\tau_1,\tau_2;t_1,t_2) = \mathbb{E}\Big\{c(\tau_1;t_1)c^*(\tau_2;t_2)\Big\}, \tag{2.2.7}$$

where $\mathbb{E}\{\cdot\}$ denotes expected value of $\{\cdot\}$, and the frequency-time autocorrelation function defined as

$$R_{CC}(f_1,f_2;t_1,t_2) = \mathbb{E}\Big\{C(f_1;t_1)C^*(f_2;t_2)\Big\}. \tag{2.2.8}$$

These two autocorrelation functions are the bases for further characterization of the processes $c(\tau;t)$ and $C(f;t)$. Interpretation of both (2.2.7) and (2.2.8) is a bit tedious, but they can provide distortion measurements of the transmitted signal in τ and in f at time t. From relationship (2.2.6), $R_{cc}(\tau_1,\tau_2;t_1,t_2)$ and $R_{CC}(f_1,f_2;t_1,t_2)$ are related by a two-dimensional Fourier transform. Explicitly

$$R_{cc}(\tau_1,\tau_2;t_1,t_2) = \int_{-\infty}^{\infty}\int_{-\infty}^{\infty} R_{CC}(f_1,f_2;t_1,t_2)\ e^{j2\pi(f_2\tau_2-f_1\tau_1)}\ df_1\ df_2 \tag{2.2.9a}$$

[2]Same remark as footnote 1 with the transfer function concept.

$$R_{CC}(f_1,f_2;t_1,t_2) = \int_{-\infty}^{\infty}\int_{-\infty}^{\infty} R_{cc}(\tau_1,\tau_2;t_1,t_2)\, e^{j2\pi(f_1\tau_1 - f_2\tau_2)}\, d\tau_1\, d\tau_2. \qquad (2.2.9b)$$

To this point, no assumptions have been made about the processes $c(\tau;t)$ and $C(f;t)$ other than that they are complex-valued Gaussian processes in the t variable. Three assumptions can be made that will simplify the correlation functions and will give an intuitive interpretation of the space-time and frequency-time autocorrelation functions. Namely,

1) Wide-sense stationary channel (WSS channel): When the input signal is stationary, the output signal is also stationary. This is a simple result based on the linear assumption for the channel.
2) Uncorrelated scattering channel (US channel): The signal at delay τ_1 is uncorrelated with the signal at delay τ_2. This assumption can be justified using the same arguments leading to the complex Gaussian nature of $c(\tau;t)$ in the t variable [9].
3) Wide-sense stationary uncorrelated scattering channel (WSSUS channel): Both assumptions 1) and 2) are applied.

In most radio channels, assumption 3) is realistic [15] and the rest of the analysis will be based on it. The impact on the space-time autocorrelation function is to reduce it to a bitemporal function

$$R_{cc}(\tau_1,\tau_2;t+\Delta t,t) = \begin{cases} R_{cc}(\tau;\Delta t), & \tau=\tau_1=\tau_2; \\ 0, & \tau_1\neq\tau_2, \end{cases} \qquad (2.2.10)$$

where $\Delta t = t_1 - t_2$ and $t = t_2$. $R_{cc}(\tau;\Delta t)$ represents the channel average output power as a function of the delay τ and the difference time observation instant Δt. The special case $\Delta t = 0$ gives the channel average output power at time t, delay τ, and is thus the variance of $c(\tau;t)$

$$R_{cc}(\tau;0) = \mathbb{E}\left\{|c(\tau;t)|^2\right\} = R_{cc}(\tau). \qquad (2.2.11)$$

$R_{cc}(\tau)$ is named the multipath intensity profile and the value over which it is non-negligible[3] is called the multipath spread of the channel and will be denoted T_m. Turning now to the frequency-time

[3] The non-negligible range of an autocorrelation function is often based upon the range in which the normalized correlation coefficient exceeds 0.5 [10].

autocorrelation function, it can be shown using (2.2.9b) and assumption 3) that

$$R_{CC}(f_1,f_2;t+\Delta t,t) = R_{CC}(\Delta f;\Delta t). \tag{2.2.12}$$

$R_{CC}(\Delta f;\Delta t)$ is stationary in both time t and frequency f (in f due to the US channel condition). $R_{CC}(\Delta f;\Delta t)$ represents the average power of 2 tones separated by Δf as a function of the observation time difference Δt. Looking again at the special case $\Delta t=0$ leads to the two-frequency autocorrelation function $R_{CC}(\Delta f)$. This function provides a measure of the frequency coherence of the channel and the bandwidth over which the function is non-negligible is called the coherence bandwidth, denoted B_C. B_C represents the bandwidth over which all signal components fade "together", and $C(f;t)$ is the random frequency response of an all-pass filter (over B_C) that applies to all signal components. The Fourier transform pair of (2.2.9) can be simplified to give prominence to the link between $R_{cc}(\tau)$ and $R_{CC}(\Delta f)$

$$R_{cc}(\tau) = \int_{-\infty}^{\infty} R_{CC}(\Delta f)\, e^{j2\pi\Delta f\tau}\, df \tag{2.2.13}$$

$$R_{CC}(\Delta f) = \int_{-\infty}^{\infty} R_{cc}(\tau)\, e^{-j2\pi\Delta f\tau}\, d\tau. \tag{2.2.14}$$

As a result, the reciprocal of the coherence bandwidth can be approximated using the multipath spread,

$$T_m \approx \frac{1}{B_C}. \tag{2.2.15}$$

2.2.3 Channel Time Variations and the Scattering Function

In the last section, the characterization of the channel was examined in the τ and f variables of $c(\tau;t)$ and $C(f;t)$ respectively. This lead to the multipath intensity profile and the two-frequency autocorrelation which characterize the channel. In this section, the effect of time variations of the structure of the channel will be described.

Starting with $R_{CC}(\Delta f;\Delta t)$ and setting $\Delta f=0$ (single spectral position) gives the time autocorrelation function $R_{CC}(\Delta t)$. This function describes the time dynamics of the process and the

value over which it is significantly different from zero is termed the coherence time T_c. The Fourier transform of $R_{CC}(\Delta f;\Delta t)$ with respect to Δt is a two-dimensional frequency function given by

$$S_{CC}(\Delta f;\nu) = \int_{-\infty}^{\infty} R_{CC}(\Delta f;\Delta t)\, e^{-j2\pi\nu\Delta t}\, d\Delta t. \tag{2.2.16}$$

This function is named the Doppler cross-power spectral density and little is said in the literature on the interpretation of this function. The special case $\Delta f=0$ provides however significant amount of information on the frequency shifting introduced by the channel. Indeed, unless $R_{CC}(0;\Delta t)$ is constant, $S_{CC}(0;\nu)$ will display a spectrum called the Doppler spectrum with fading bandwidth B_d. A pure sine wave sent through such a channel will be received as a non-monochromatic waveform. In general, the channel response to any signal contains frequencies not present in the transmission. Clearly, because of relation (2.2.16), the coherent time and the fading bandwidth are approximately related by

$$T_c \approx \frac{1}{B_d}. \tag{2.2.17}$$

The same result could have been obtained starting with $R_{cc}(\tau;\Delta t)$ but it is easier to visualize the individual results proceeding with $R_{CC}(\Delta f;\Delta t)$. Therefore, the Fourier transform of $R_{cc}(\tau;\Delta t)$ in the Δt, yields

$$S_{cc}(\tau;\nu) = \int_{-\infty}^{\infty} R_{cc}(\tau;\Delta t)\, e^{j2\pi\nu\Delta t}\, d\Delta t, \tag{2.2.18}$$

which is called the scattering function and provides a measure of the average power of the random processes, perturbing the channel, as a function of the multipath delay τ and the Doppler frequency ν. It contains all the information needed to predict the nature of the distortion in power due to the time-varying channel.

The inverse Fourier transform relationships of (2.2.16) and (2.2.18) can be written as well as a Fourier transform pair between $S_{cc}(\tau;\nu)$ and $S_{CC}(\Delta f;\nu)$. Because there are four distinct variables τ, Δt, ν, Δf as well as special cases of the functions involving these variables, it is difficult to follow the different relationships between all these functions. A summary is presented in Fig. 2.2 linking the

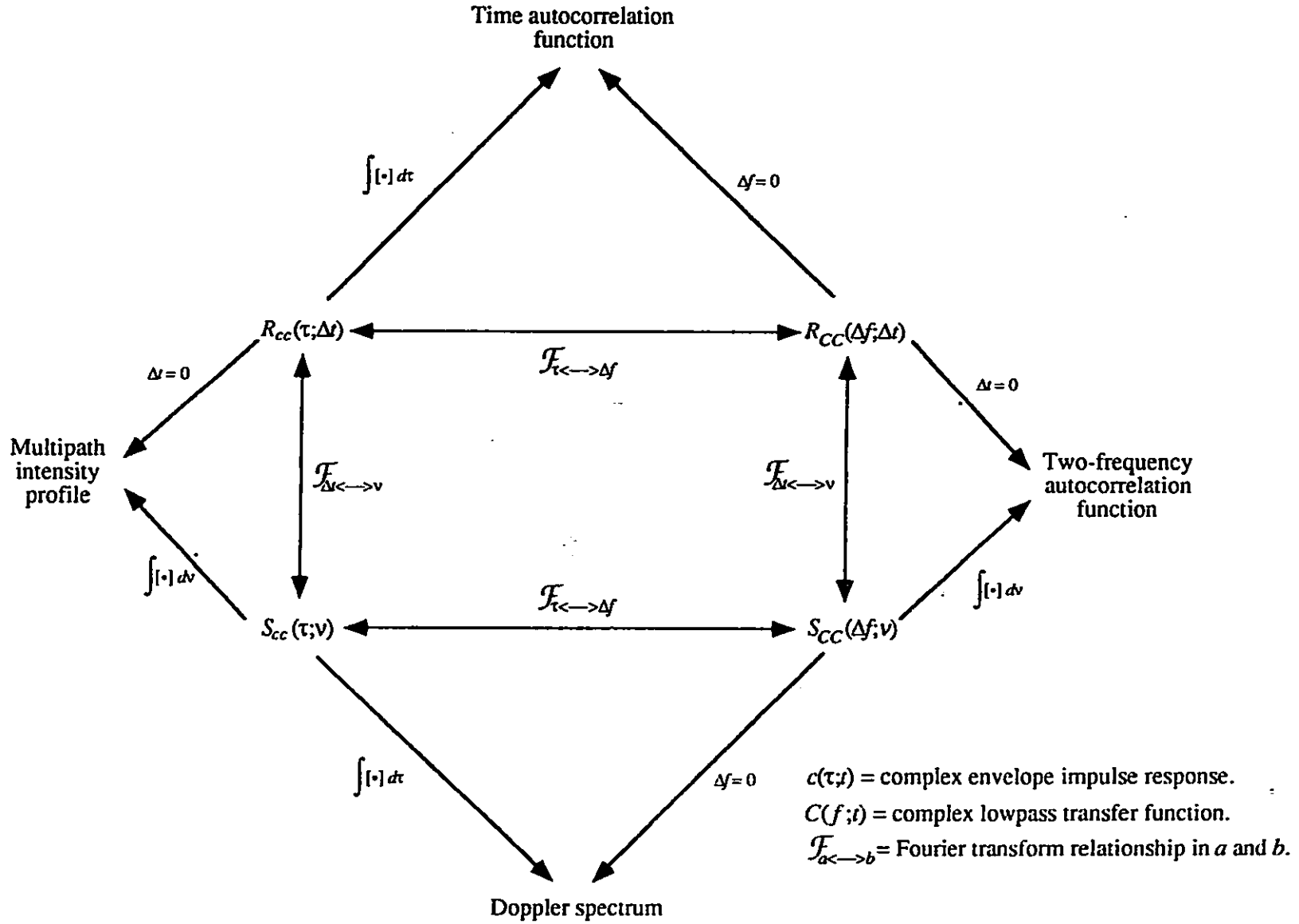

Fig. 2.2. Link between channel description functions.

different functions discussed in the last two sections, which hopefully will help keep the relationships clear.

2.2.4 Channel Classification and System Channel Model

The statistical characterization of the channel presented in §2.2.2 and §2.2.3 is applicable to most channels in radio communication systems. The important factor to know here is the extent to which these channel fluctuations affect the transmitted signal. As an example, a time-invariant channel is one in this form with an infinite coherence time and zero multipath spread. In general, channel distortion is a function of the transmitted signal bandwidth and time duration (symbol period). The bandwidth W and symbol period T of the transmitted signal relative to the channel parameters, derived from the statistical characterization, determine the class or the type of channel of interest and the approximations made to simplify the analysis. Looking at the different possibilities, Table 1 summarizes the classification adopted for this thesis.

Table 1. Channel classification.

		Frequency	
		Flat	Selective
Time	Slow	$\left[\begin{array}{c} W \ll B_C \\ \text{or} \\ T \gg T_m \end{array}\right]$ and $\left[\begin{array}{c} T \ll T_c \\ \text{or} \\ W \gg B_d \end{array}\right]$	$\left[\begin{array}{c} W \approx B_C \\ \text{or} \\ T \approx T_m \end{array}\right]$ and $\left[\begin{array}{c} T \ll T_c \\ \text{or} \\ W \gg B_d \end{array}\right]$
	Fast	$\left[\begin{array}{c} W \ll B_C \\ \text{or} \\ T \gg T_m \end{array}\right]$ and $\left[\begin{array}{c} T \approx T_c \\ \text{or} \\ W \approx B_d \end{array}\right]$	$\left[\begin{array}{c} W \approx B_C \\ \text{or} \\ T \approx T_m \end{array}\right]$ and $\left[\begin{array}{c} T \approx T_c \\ \text{or} \\ W \approx B_d \end{array}\right]$

Once the class in which the channel falls is determined, a simplified model can be adopted on which analysis can be based. In the case of interest here, the carrier frequency is expected to be in the low gigahertz band i.e., ≃1-10 GHz. A small variation in the path length will cause a significant carrier-phase change causing broadening of the transmitted signal, and consequently a fast fading environment is representative. The symbol rate, however, will be fairly low, (less than 10 kbaud/s) and the multipath delay difference is expected to be very small because the scatters are usually located near the receiver in mobile communications. Consequently, the multipath spread should be negligible. The channel of interest here can thus be classified as a fast flat-fading (FFF) channel.

The model for such a channel is relatively easy to derived. Using the assumption that $T \gg T_m$, $c(\tau;t)$ can be expressed as

$$c(\tau;t) = \begin{cases} |c(t)|\, e^{j\theta(t)} = c(t), & \tau = 0; \\ 0, & \tau \neq 0. \end{cases} \tag{2.2.19}$$

Substituting (2.2.19) into (2.2.4) yields

$$v'(t) = u(t)\, |c(t)|\, e^{j\theta(t)} = u(t)\, c(t)\,. \tag{2.2.20}$$

If the lowpass equivalent additive noise contribution $n(t)$ is also considered, the lowpass equivalent for the total received signal can be written as

$$v(t) = u(t)\, c(t) + n(t). \tag{2.2.21}$$

Remember that $c(t)$ is modeled as a complex Gaussian process, and if $c(t)$ is non-zero mean, one can write $c(t)=m_c+c'(t)$ with $c'(t)$ being a complex Gaussian process with zero-mean. Equation (2.2.21) can then be rewritten in a normalized way such that

$$v(t) = u(t)\left[1 + c'(t)\right] + n(t). \tag{2.2.22}$$

The real received signal will then be given by

$$r(t) = s(t)\left[0.707 + h'(t)\right] + w(t), \tag{2.2.23}$$

where $h'(t)$ and $w(t)$ are the real signals associated with the complex envelope $c'(t)$ and $n(t)$

respectively. Figure 2.3 illustrates this general Rician equivalent lowpass FFF channel model and as it can be seen, the transformation process of Fig. 2.1 has been used to model $c'(t)$. As a final note, a Rician channel is often specified in terms of the K factor defined as the average power in the fading components over the average power in the steady component. In terms of the Gaussian process $c(t)$ in (2.2.19), this definition is equivalent to the reciprocal of the ratio $|m_c|^2/\sigma_c^2$ in the probability density function of $|c(t)|$ and $\theta(t)$ (see §2.1). The K factor is then the ratio of the variance to the mean square of the real Gaussian process used that describes $c(t)$.

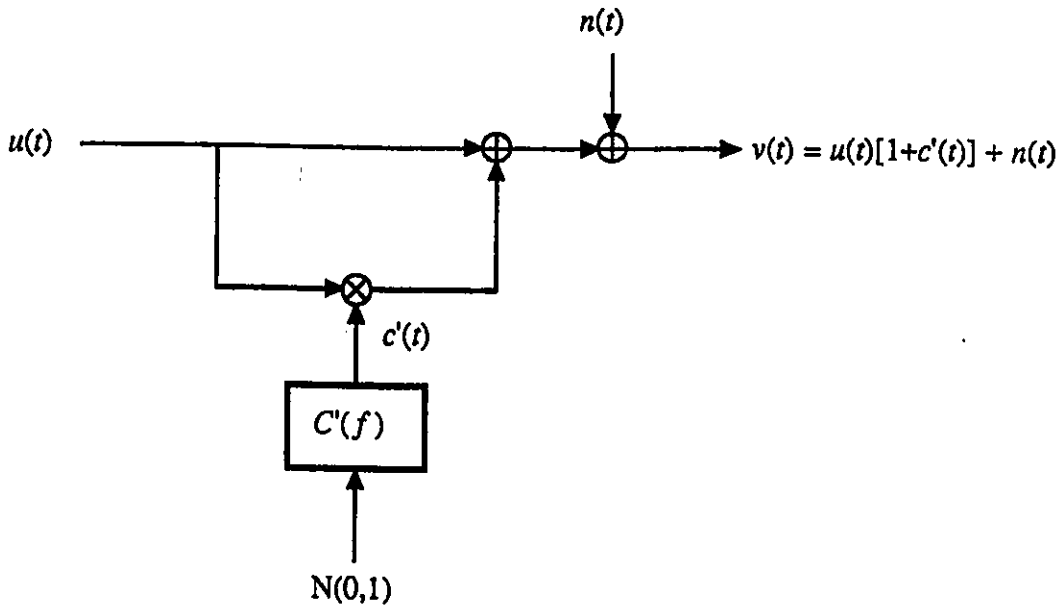

Fig. 2.3. Rician fast flat-fading channel model.

2.3 Modulation Scheme

2.3.1 Continuous Phase Modulation

The transmitted signal generated by CPM can be written as [11][12]

$$s(t) = \sqrt{\frac{2E}{T}} \cos\left[2\pi f_0 t + \phi(t,\underline{a}) + \phi_0\right], \tag{2.3.1}$$

where f_0 is the carrier frequency (assuming $f_0 T \gg 1$), ϕ_0 is the "starting angle" (which is set to zero without loss of generality), E represents the energy per symbol, T is the symbol period, and $\phi(t,\underline{a})$ is the continuous time excess-phase function corresponding to a data stream $\{\ldots, a_{-1}, a_0, a_1, a_2, \ldots\}$ denoted by $\underline{a}$. The excess-phase function can be expressed in the form

$$\phi(t,\underline{a}) = 2\pi h \int_0^t \sum_i a_i\, g(\tau - iT)\, d\tau, \tag{2.3.2}$$

where h is the modulation index, and the a_i's are the data symbols taken from a set of M possible symbol values $\pm 1, \pm 3, \ldots, \pm(M-1)$ (M is normally a power of 2 but can be any positive integer), and $g(t)$ is the frequency pulse shape. The function $g(t)$ is assumed to be non-zero only over the finite interval $0 \le t \le LT$ for some integer L, and to meet the equality constraint

$$\int_0^{LT} g(t)\, dt = \frac{1}{2}. \tag{2.3.3}$$

While the analysis will be kept as general as possible, binary ($M=2$), quaternary ($M=4$) and 8-ary ($M=8$) CPM schemes will be primarily considered here. The frequency pulse shape $g(t)$ plays an important role in many aspects of a CPM system performance including timing recovery and therefore, it is going to be an important function in this study. Using the finite pulse length condition, (2.3.2) can be written to highlight the memory introduced in the phase of a CPM signal. The phase $\phi(t,\underline{a})$ during the interval $nT \le t \le (n+1)T$ for a rational modulation index $h = 2k/p$ (k and p relatively prime) is given by

$$\phi(t,\underline{a}) = 2\pi h \int_0^t \sum_{i=n-L+1}^{n} a_i\, g(\tau - iT)\, d\tau + \left[\pi h \sum_{i=0}^{n-L} a_i\right]_{\text{modulo } 2\pi}. \tag{2.3.4}$$

The first term represents the present symbol and the past symbols that still have an influence on the state transitions. The $L-1$ last symbols represent a memory built into the signal and can be used to improve spectral efficiency and reduce error symbol probability. The second term in (2.3.4) represents the past symbols that have no effect on the present state transition and can only assume p different values. A state is a possible value of $\phi(t,\underline{a})$ at the sampling instant modulo 2π and is defined as a vector $(\varpi_{-n}, a_{n-1}, a_{n-2}, \ldots, a_{n-L+1})$ that can have $pM^{(L-1)}$ values at most with ϖ_{-n} representing the second term in (2.3.4). Note that even if some symbols do not have any influence on the present state transition they still affect the phase state.

The complex envelope representation can be exploited to define a baseband CPM signal $u(t,\underline{a})$ that is going to be used extensively in the analysis throughout the thesis. Using (2.1.1) and (2.1.5), equation (2.3.1) becomes

$$s(t,\underline{a}) = \sqrt{2}\,\Re\left\{\sqrt{P}\; e^{j\phi(t,\underline{a})}\; e^{j2\pi f_0 t}\right\}, \tag{2.3.5}$$

where $P=E/T$ and from which it is found using (2.1.4)

$$u(t,\underline{a}) = \sqrt{P}\; e^{j\phi(t,\underline{a})}. \tag{2.3.6}$$

This baseband constant envelope signal can be interpreted as an FM or PM signal because of the phase continuity. The generation of $u(t,\underline{a})$ can be considered as being the output of either of two conceptual CPM baseband modulators as shown in Fig. 2.4 . In the case of the FM-modulator the signal at the input of the multiplier is $\sum_i a_i\, g(t-iT)$, a pulse amplitude modulation (PAM) signal. The real signal $s(t,\underline{a})$ is obtain by multiplying $u(t,\underline{a})$ by $e^{j2\pi f_0 t}$ and taking only the real part. One possible approach to implement (2.3.5) is to take advantage of equation (2.1.2) and implement an inphase-quadrature (I-Q) modulator with input $\phi(t,\underline{a})$ and output $s(t,\underline{a})$.

As with other modulation schemes, signal design plays an important role in many practical aspects of system performance. The classification of CPM signals is usually done according to one of the parameters previously described, (i.e. $g(t)$, h or L). A subclass often encountered is "full response signalling". This term refers to the case where $L=1$, while "partial response signalling" refers to the

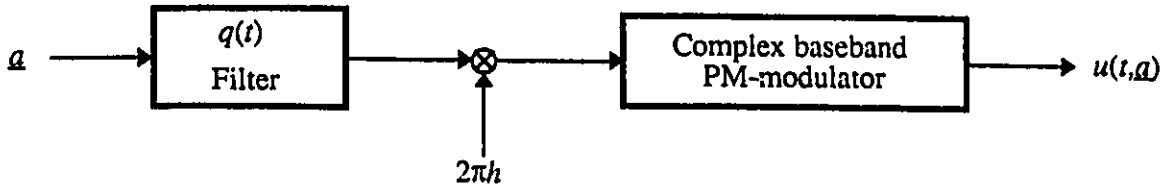

a) PM conceptual view

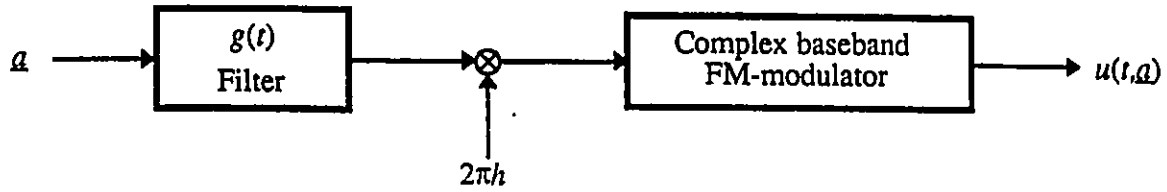

b) FM conceptual view

Fig. 2.4. Conceptual CPM baseband modulators.

case where $L>1$ [17][18]. This partitioning of CPM schemes is simple but can lead to confusion for certain pulse shapes, as will be seen later, because of the context in which the expression "partial response" is usually employed. Commonly, schemes are also defined according to the pulse shape $g(t)$ (as opposed to just the pulse shape duration). A widely used family of pulse shape is the LREC family defined by

$$g_{LREC}(t) = \begin{cases} \frac{1}{2LT}, & 0 \le t \le LT; \\ 0, & \text{elsewhere.} \end{cases} \tag{2.3.7}$$

Other common pulse shapes are defined in Appendix A. The most well-known CPM scheme using this pulse shape is probably minimum shift keying (MSK) which employs a 1REC pulse with $h=1/2$. A more general class of signals is the MSK-like [29] scheme ($L=1$, $h=1/2$ with any pulse shape) some members of which can achieve better spectral roll-off at the expense of a wider main lobe compared to MSK [12]. Continuous phase frequency shift keying (1REC with any h) has also been widely studied.

Note that MSK is a particular case of both MSK-like and continuous phase frequency shift keying schemes. Many others schemes can be found in the literature which differ in the pulse shape $g(t)$ used. Now that the transmitted signal is well-defined, attention is turned toward the other end of the system, the receiver.

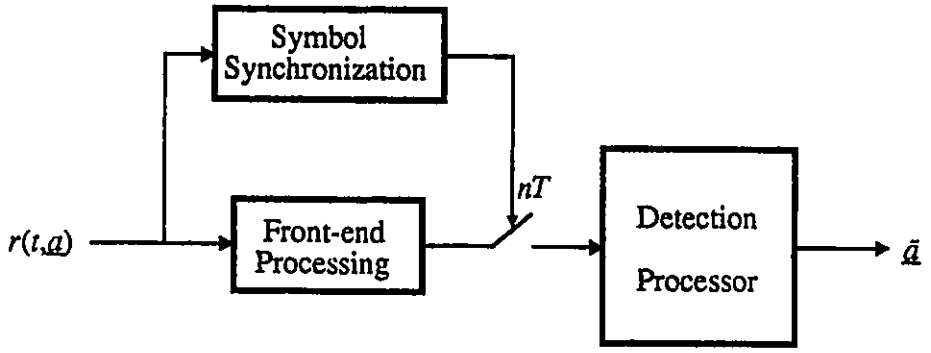

Fig. 2.5. General receiver structure.

Optimum coherent demodulation of CPM can be accomplish by means of the maximum likelihood sequence estimation (MLSE) procedure. The receiver structure consist of a bank of linear filters sampled every symbol interval, which produce the information used by the Viterbi algorithm to perform the MLSE. This receiver is very complex, often not realizable because the complexity grows exponentially with signal memory. For the additive white Gaussian noise (AWGN) channel with high signal-to-noise ratio (SNR), an interesting alternative is the coherent linear I-Q receiver. Also, non-coherent receivers are often considered because they tend to be simpler, and less expensive. For example, the differential and discriminator detection techniques are commonly used as they are more robust to fading and phase noise. In contrast to the MLSE receiver, these receivers operate mostly on a symbol-by-symbol basis and are thus suboptimum even within the non-coherent receiver class. These two techniques are nonetheless used in mobile communications to avoid carrier-phase recovery as discussed in Chapter 1 [4]. A common point to all these receivers is that they require symbol

synchronization to perform the detection. Since the purpose of this thesis is not to look at a particular receiver, a general receiver structure is presented in Fig. 2.5 where it is shown that the timing clock is derived from the signal itself. In this figure, $r(t)$ is the received signal, nT the sampling instants and $\tilde{a}$ the detected symbols. In §2.4, a general approach to estimate the timing instant will be presented.

2.3.2 Nyquist Pulse Shaping

The pulse shape defined in the preceding section can have any form as long as it meets the constraint (2.3.3). The use of pulse shaping techniques to improve different aspects of modulation scheme such as PAM can also be applied to CPM since it is a PAM signal which feeds the FM modulator in the FM conceptualization of CPM. Nyquist pulse shapes [13] for distortionless transmission are often used in PAM and application to CPM is logical although the interpretation is now quite different. The three criteria formulated by Nyquist will be briefly summarized.

Let a Nyquist filter be defined by its impulse response $g_m(t)$ and its frequency response $G_m(f)$ where m=1,2,3 specify Nyquist I, II or III criterion. If this filter is excited by a sequence of weighted delta functions $[a_i\delta(t)]$ at rate $1/T$, then the output signal $y(t)$ can be written

$$y(t) = \sum_i a_i\, g_m(t-iT). \tag{2.3.8}$$

The Nyquist criterion are just constraints on $g_m(t)$ to achieve certain goals for $y(t)$. The constraints that the three criteria represent on $y(t)$ are [20], [21]:

Nyquist I: Constraint ensuring $y(t)$ has undistorted amplitude at the sampling instant $t=nT$,

Nyquist II: Constraint ensuring $y(t)$ has undistorted pulse width,

Nyquist III: Constraint ensuring $y(t)$ has undistorted pulse area in a time unit T.

Each of these constraints can be translated into a constraint on the time-domain or frequency-domain of the pulse shape. These equivalences are summarized on the next page:

Nyquist criterion	Time-domain requirement	Frequency-domain requirement	
I	$g_1(iT) = \begin{cases} 1, & i=0 \\ 0, & i\neq 0 \end{cases}$	$\sum_{i=-\infty}^{\infty} G_1(f-\frac{i}{T}) = T$	(2.3.9)
II	$g_2(\frac{2i-1}{2}T) = \begin{cases} 1/2, & i=0,1 \\ 0, & i\neq 0,1 \end{cases}$	$\sum_{i=-\infty}^{\infty} (-1)^i\, G_2(f-\frac{i}{T}) = T\cos\pi fT$	(2.3.10)
III	$\int_{(2i-1)\frac{T}{2}}^{(2i+1)\frac{T}{2}} g_3(t)\,dt = \begin{cases} 1, & i=0 \\ 0, & i\neq 0 \end{cases}$	$\int_{-\infty}^{\infty} G_3(f)\,\mathrm{sinc}(fT)\,e^{j2\pi fiT}\,df = \begin{cases} T, & i=0 \\ 0, & i\neq 0 \end{cases}$	(2.3.11)

with i integers and $\mathrm{sinc}(fT) = \frac{\sin\pi fT}{\pi fT}$. From these equivalences, it is easy to find pulses satisfying the various criteria with additional constraints imposed on the bandwidth of the pulses. It can readily be seen that if a pulse is restricted to a spectrum $[-W, W]$, then there are an infinite number of pulses satisfying these criteria if $W>1/2T$, but only one pulse when $W=1/2T$ and none for $W<1/2T$. The minimum bandwidth simultaneous solutions of Nyquist I and II, Nyquist II and III have been found in [20],[22].

An interesting relationship derived in [21] links bandlimited Nyquist I and III pulse definitions in the frequency domain as follows:

$$G_3(f) = \frac{G_1(f)}{\mathrm{sinc}(fT)}. \tag{2.3.11}$$

This relationship can be very useful since a lot of Nyquist I filters are known and thus have a Nyquist III representation. The expression is simple in the frequency-domain and has an equivalence in the time-domain in a form of infinite series representation [23]

$$g_3(t) = \sum_{k=-\infty}^{\infty} \frac{1}{2W}\, b(\frac{k}{2W})\, g_1\Big\{2W(t-\frac{k}{2W})\Big\}, \tag{2.3.12a}$$

where $W\in[1/2T, 1/T]$ is the one-sided bandwidth of $G_3(f)$ and

$$\frac{1}{2W}\, b\left(\frac{k}{2W}\right) = \frac{4W}{T}\int_0^{\pi/2} \frac{x\cos(2kx)}{\sin(2Wx)}\, dx\,. \tag{2.3.12b}$$

This expression has been found using the sampling arguments and the case $B=1/2T$ represents the minimum bandwidth solution[4]. Often this expression is of limited usefulness because of the infinite sum (although it can be well approximated by including only a few values of k) and the more complicated time domain representation of Nyquist I pulse shapes. To end this section, Fig. 2.6 shows the Nyquist III Cosine Rolloff (N3CR) pulse shape in the time and frequency domain. This pulse is defined as (see Appendix A for other Nyquist III pulse shape definitions)

$$G_{N3CR}(f) = \frac{G_{N1CR}(f)}{\mathrm{sinc}(fT)}, \tag{2.3.13}$$

where

$$G_{N1CR}(f) = \begin{cases} \frac{1}{2}, & |f| \le \frac{1-\alpha}{2T}; \\ \frac{1}{2}\cos^2\left\{\frac{\pi}{2\alpha}\left(|f| + \frac{\alpha-1}{2T}\right)\right\}, & \frac{1-\alpha}{2T} \le |f| \le \frac{1+\alpha}{2T}; \\ 0, & \text{elsewhere,} \end{cases} \tag{2.3.14}$$

with $\alpha\in[0,1]$ the excess bandwidth. In general $g(t)$ decays faster with increasing excess bandwidth. Note in Fig. 2.6a that the pulse shapes meet at the same point on each side of the main lobe in the interval $-0.5<t/T<-0.5$ and that in Fig. 2.6b they meet also at $fT=0.5$.

2.3.3 Nyquist III Pulse Shaping in CPM

The significance of pulses satisfying Nyquist first criterion has been recognized in baseband transmission systems. In the context of CPM however, due to the integration of the PAM signal in forming the excess-phase function, pulses satisfying Nyquist third criterion become important. Nyquist III pulses exhibit nice properties making them an attractive choice for bandwidth efficient mobile communications systems.

[4] In this case $g_3(t)$ can be represented as an infinite sum of scaled and delayed versions of a sinc function. The similitude in shape between sinc(t) and $g_3(t)$ becomes more and more pronounced away from the main peak.

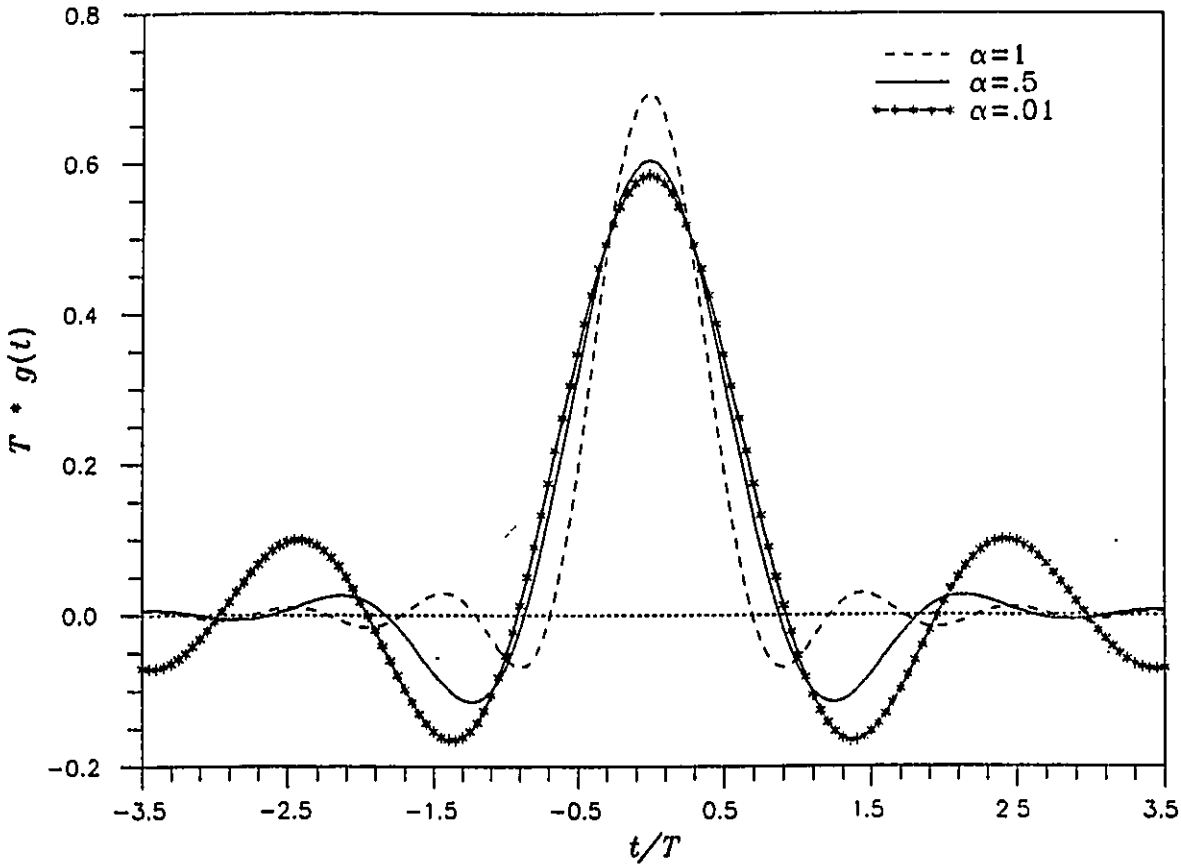

a) Time-domain

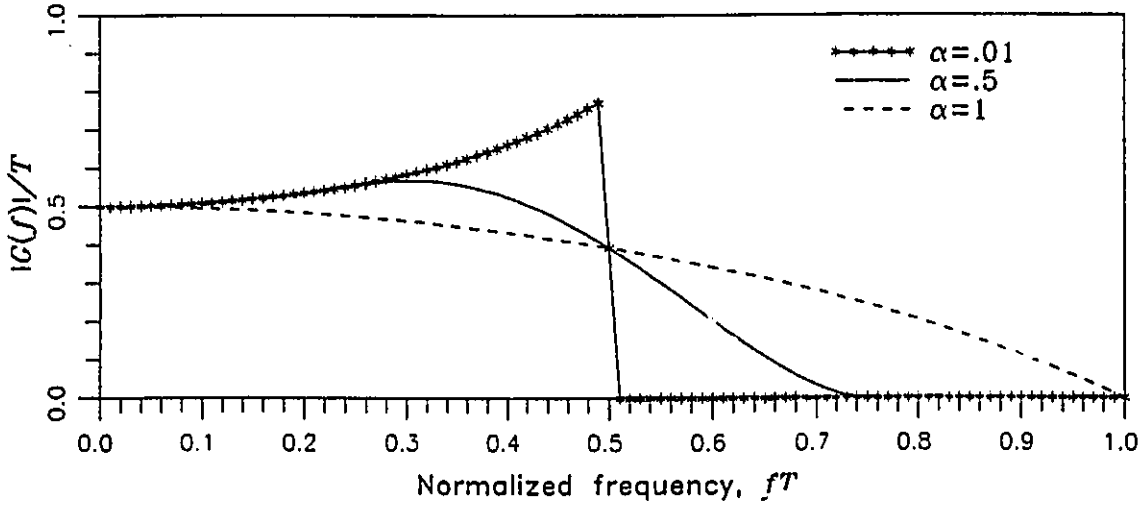

b) Frequency-domain

Fig. 2.6. N3CR pulse shape with α=.01, .5, and 1.

The first property associated with Nyquist III CPM is its nice phase behavior at the sampling instant. To see this, $g_3(t)$ is defined for CPM. According to constraint (2.3.3), $g_3(t)$ is of finite duration and therefore truncation to L symbol intervals must be done on the ideal pulse shape. Now shifting $g_3(t)$ to the right by $LT/2$ makes it causal and symmetric about the main peak (desirable properties in most systems although not conceptually necessary). The frequency pulse $g_3(t)$ is thus of odd length and must be properly scaled to meet (2.3.3). Looking now at $q(t)$ defined as

$$q(t) = \int_{-\infty}^{t} g(\tau)\, d\tau. \tag{2.3.15}$$

Fig. 2.7 shows the particular case of N3CR L=7 (7N3CR) and reveals the phase pulse values at the sampling instant. Observe that the phase response values at iT (i integers) are zero before the interval $\frac{L+1}{2}$ and 1/2 after it. This feature is characteristic of all Nyquist III waveforms, and is equivalent to the periodic zero-crossings of the Nyquist I criterion. The phase values at the sampling instant for a CPM signal associated with Nyquist III pulse shape will only be due to a single symbol interval even though the pulse shape is of length greater than one. This is an inter-symbol interference (ISI) free behavior at the sampling instant. For binary signalling with h=1/2, this class of signal is referred as MSK-type modulation [25]. The multilevel case has a similar equivalence where the modulation index is fixed to $1/M$. Here, the interest in mainly in the results for this type of scheme but the system description and analysis will be kept as general as possible so that other classes of signals can be studied in the same way. A second nice property of Nyquist III signalling comes from the length of the pulse shape which permits achievement of good side lobe reduction, similar to partial response schemes. Thus Nyquist III signalling combines the advantage of no ISI full response signalling with some of the bandwidth efficiency of partial response. The bandwidth efficiency of Nyquist III CPM with h=1/2 has been investigated in [22] where promising applications are shown for these schemes. A third advantageous property is highlighted in §2.4 .

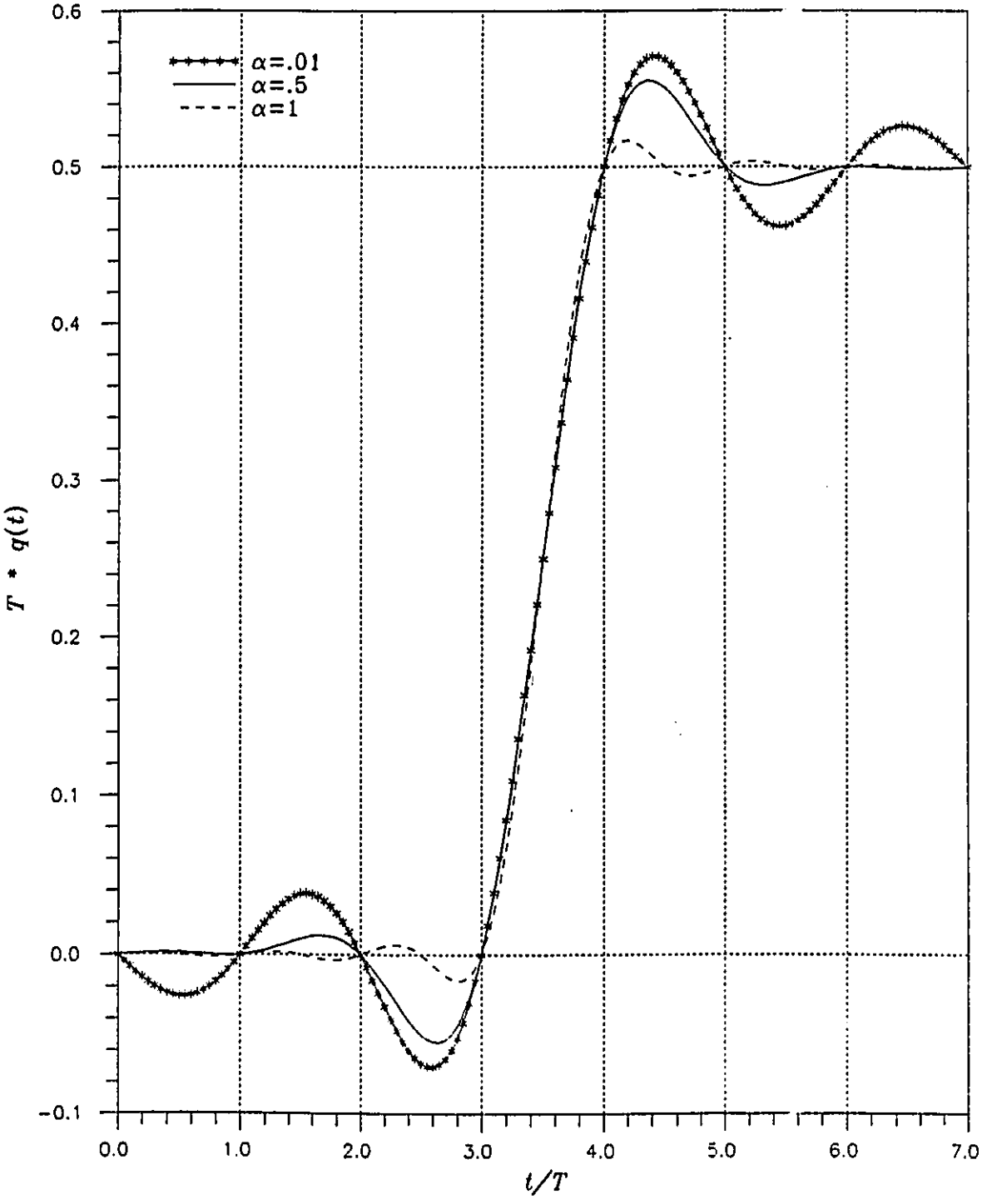

Fig. 2.7. CPM 7N3CR phase pulse shape with α=.01, .5, and 1.

As far as demodulation is concerned, the optimum coherent receiver remains the MLSE procedure because of the memory introduced in the modulated signal. A potentially attractive non-coherent receiver might be the differential detector because of the full response characteristic of the modulated signal [16]. Most of the work on Nyquist III based CPM is related to Tamed Frequency Modulation (TFM) [26]-[28] and generalized MSK [25][29].

2.3.4 Autocorrelation Function and Average Power Spectral Density of a CPM Signal

The problem of computing the spectrum of an FM signal has been considered in the past and several methods have been developed. For digital FM, there are basically the following three theoretical approachs to solve the problem:

1) the direct approach [31]: where the Fourier transformations of the segments of a transmitted signal are calculated. For each frequency the magnitude is squared, averaged, divided by the segment length, and then the limit is evaluated as the length increases towards infinity. This is simply express as

$$S(f) = \lim_{NT \to \infty} \frac{\mathbb{E}\left\{|\mathcal{F}[s_{NT}(t)]|^2\right\}}{NT}, \tag{2.3.17}$$

with $\mathcal{F}[\cdot]$ denoting Fourier transform of $[\cdot]$ and

$$s_{NT}(t) = \begin{cases} s(t), & t \in [0, NT]; \\ 0, & \text{elsewhere.} \end{cases}$$

From the computational point of view, this method can be very time consuming and for this reason was not considered.

2) the Markov chain approach [32]: where a finite Markov chain model is derived for $s(t)$ characterized by its state probability and transition probability distribution. Once this characterization is found, it is possible to express $S(f)$ as defined in (2.3.17) directly in terms of those distributions.

3) the autocorrelation function approach [33][34]: where the autocorrelation of the average signal

with respect to the data is evaluated, a time average over one symbol period is performed and finally a Fourier transformation as defined in (2.1.8) is computed to get the average power spectral density (PSD). This method is computationally efficient and it was found to be appropriate for the kind of analysis dealt with here, i.e., correlation and spectrum of a signal passed through deterministic systems.

2.3.4.1 Autocorrelation function

In §2.1, it was seen that a bandpass signal and its autocorrelation can be represented in a complex envelope form. Recall that the complex envelope of a CPM signal is given by

$$u(t,\underline{a}) = \sqrt{P}\ e^{j\phi(t,\underline{a})}. \tag{2.3.18}$$

In preparation for looking at the autocorrelation function, let us examine the expected value of this signal with respect to the data sequence. Assuming that the symbols are independent and M is even, it is found that

$$m_u(t) = \mathbb{E}\Big\{u(t,\underline{a})\Big\} = \mathbb{E}\Big\{e^{j\phi(t,\underline{a})}\Big\} = \mathbb{E}\Big\{e^{\,j2\pi h\int_0^t \sum_i a_i\, g(\tau-iT)\,d\tau}\Big\},$$

$$m_u(t) = \prod_i \sum_{\substack{k=-(M-1)\\ k\ \text{odd}}}^{(M-1)} P_k\ e^{j2\pi hkq(t-iT)}, \tag{2.3.19}$$

where P_k is the *a priori* probability that $a_i=k$. Now, assuming that a CPM signal has wide sense cyclostationary second order statistic in t with period T [12][19], the interval $0\le t\le T$ can be exclusively studied without loss of generality. Also when $i>0$, $q(t-iT)=0$ and when $i\le L$, $q(t-iT)=1/2$. Thus, (2.3.19) can be simplified to

$$m_u(t) = \prod_{i=1-L}^{0} \sum_{\substack{k=-(M-1)\\ k\ \text{odd}}}^{(M-1)} P_k\ e^{j2\pi hkq(t-iT)} \times \lim_{i\to\infty} \left(\sum_{\substack{k=-(M-1)\\ k\ \text{odd}}}^{(M-1)} P_k\ e^{j\pi hk}\right)^i. \tag{2.3.20}$$

For non-integral h and practical symbol probability distribution, the value in the parenthesis, labelled C_a can easily be seen to have a modulus less than unity from the triangle inequality. Thus, the expected value reduces to 0. When h is an integer it is found that

$$C_a = \sum_{\substack{k=-(M-1) \\ k \text{ odd}}}^{(M-1)} P_k \, e^{j\pi hk} = \begin{cases} +1, & h \text{ even integer;} \\ -1, & h \text{ odd integer,} \end{cases} \tag{2.3.21}$$

and consequently, the case where h is even reduces to find the expected value of a product of L terms. The case of h odd seems to lead to the failure of the limit to exist due to the sign alternation. This result only implies that the phase changes due to old data are odd multiple of π radians. As a result, the value of $m_u(t)$ in the interval $iT \le t \le (i+1)T$ is the sign reverse value of $m_u(t)$ in the interval $(i-1)T \le t \le iT$. Therefore, it can be concluded that $m_u(t)$ is periodic with period T when h is an even integer and with period $2T$ when h is odd integer. This is an important result that will be used later in the synchronizer description. Note that although $u(t,\underline{a})$ is a cyclostationary process, no periodic waveforms are present in $u(t,\underline{a})$ when h is non-integer.

Consider now the autocorrelation function $R_{uu}(t_1,t_2)$ with respect to the data sequence,

$$R_{uu}(t_1,t_2) = \mathbb{E}\left\{ u(t_1,\underline{a})\; u^*(t_2,\underline{a}) \right\} \tag{2.3.22}$$

$$= \mathbb{E}\left\{ e^{j2\pi h \sum_i a_i \, q(t_1 - iT)} \; e^{-j2\pi h \sum_i a_i \, q(t_2 - iT)} \right\}$$

$$R_{uu}(t_1,t_2) = \prod_i \sum_{\substack{k=-(M-1) \\ k \text{ odd}}}^{(M-1)} P_k \, e^{j2\pi hk\left[q(t_1 - iT) - q(t_2 - iT)\right]}. \tag{2.3.23}$$

The purpose of this function is ultimately to compute the power spectral density (PSD). The usual approach for cyclostationary processes consists to average the process with respect to a uniformly distributed random shift $t \in [0,T]$ to generate a stationary process [35]. This approach shall be used for most of the power spectral analysis while for the signal analysis the cyclostationary form will be kept for reasons that will become obvious later. It is known that the statistics of a cyclostationary process

$u(t,\underline{a})$ are periodic along $t_1-t_2=\tau$. Thus setting $t_1=t+\tau$ and $t_2=t$ yields the new function

$$R_{uu}(\tau) = \left\langle \prod_i \sum_{\substack{k=-(M-1) \\ k \text{ odd}}}^{(M-1)} P_k \, e^{j2\pi hk\left[q(t+\tau-iT)-q(t-iT)\right]} \right\rangle_t, \tag{2.3.24}$$

where $\langle\cdot\rangle_t$ denotes average with respect to t uniformly distributed $[0,T]$. Using the finite length constraint of $g(t)$, (2.3.4) and the fact that $\Re[R_{uu}(\tau)]=\Re[R_{uu}(-\tau)]$, $\Im[R_{uu}(\tau)]=-\Im[R_{uu}(-\tau)]$ where $\Im[\cdot]$ denotes imaginary part of $[\cdot]$, the infinite product of (2.3.24) can be reduced to [34]

$$R_{uu}(\tau) = \frac{1}{T}\int_0^T \prod_{i=1-L}^{m+1} \sum_{\substack{k=-(M-1) \\ k \text{ odd}}}^{(M-1)} P_k \, e^{j2\pi hk\left[q(t+\tau-(i-m)T)-q(t-iT)\right]} \, dt \tag{2.3.25}$$

$$\tau = \tau' + mT \tag{2.3.26}$$

with $0\le\tau'<T$, and $m=0,\ 1,\ 2,\ \ldots,\ \infty$. This expression is valid for any CPM signal as long as the data are uncorrelated. A useful property of (2.3.25) is derived in [33] where it is shown that $R_{uu}(\tau)$ can be written in the form

$$R_{uu}(\tau) = R_{uu}(\tau' + mT) = C_a^{m-L}\, \mathcal{R}(\tau'), \tag{2.3.27}$$

when $m\ge L$ (i.e., it is separable in the arguments m and τ'). The function $\mathcal{R}(\tau')$ corresponds to (2.3.25) in the interval $LT\le\tau<(L+1)T$. This means that $R_{uu}(\tau)$ only has to be calculated in the interval $0\le\tau\le(L+1)T$ to know the value of the function from 0 to infinity. The value of $R_{uu}(\tau)$ from $(L+1)T$ to infinity can be subtracted from its value in the interval $LT\le\tau<(L+1)T$. To understand the impact of (2.3.27) on the interpretation of $R_{uu}(\tau)$ it is appropriate to go back to $R_{uu}(t_1,t_2)$ where it is known in general that

$$R_{uu}(t_1,t_2) = C_{uu}(t_1,t_2) + m_u(t_1)\, m_u^*(t_2), \tag{2.3.28}$$

where $C_{uu}(t_1,t_2)$ is the autocovariance function of $u(t)$. This simply means that $R_{uu}(t_1,t_2)$ is formed out of a continuous part (i.e., the autocovariance function) and a periodic part (i.e., the product of the means). Since we are interested in stationary processes we can define two stationarized processes in the

same way that we have defined $R(\tau)$, namely

$$R_{con}(\tau) \equiv \left\langle C_{uu}(t+\tau,t) \right\rangle_t, \tag{2.3.29}$$

and

$$R_{dis}(\tau) \equiv \left\langle m_u(t+\tau)\, m_u^*(t) \right\rangle_t \tag{2.3.30}$$

that allow to write

$$R_{uu}(\tau) = R_{con}(\tau) + R_{dis}(\tau)\,. \tag{2.3.31}$$

Two cases of (2.3.31) can be identified: case A $m_u(t)=0$ (h non-integer) and case B $m_u(t)\neq 0$ (h integer). By inspection of (2.3.25) (2.3.27) and (2.3.31), the characteristics of $R_{uu}(\tau)$ become apparent and they are summarized below:

case A: - $R_{uu}(\tau)$ is real and has duration of $(L+1)T$ if the a_i's are evenly distributed.

- $R_{uu}(\tau)$ is complex and has infinite duration if the a_i's are not evenly distributed. The value of $R_{uu}(\tau)$ for $\tau > LT$ has a geometric decay from symbol interval to symbol interval, given by C_a^{m-L} $m \geq L$.

case B: - The duration of $R_{con}(\tau)$ is LT.

- $R_{dis}(\tau)$ has period $2T$ if h is odd and period T if h is even. This can easily be seen with $C_a = \pm 1$ in (2.3.27).

- Both $R_{con}(\tau)$ and $R_{dis}(\tau)$ are complex if the a_i's are not evenly distributed.

The value of $R_{con}(\tau)$ and $R_{dis}(\tau)$ can easily be computed using (2.3.25). Since $R_{con}(\tau)=0$ for $\tau > LT$, $R_{dis}(\tau)$ in $LT<\tau<(L+1)T$ can be computed and its periodic property can be used to extend it over all τ. Since $R_{dis}(\tau)$ is now completely known, the continuous part can be computed using

$$R_{con}(\tau) = \begin{cases} R_{uu}(\tau) - R_{dis}(\tau), & |\tau| \leq LT; \\ 0, & |\tau| > LT. \end{cases} \tag{2.3.32}$$

An example of case A for MSK with symbol probability distribution $P_{-1}=.25$, $P_{+1}=.75$ is shown in

Fig. 2.8. It can be seen that (2.3.27) holds with $C_a=j/2$. Figure 2.9 shows case B for binary 3N3CR $h=1$ with equally distributed a'_is. For $\tau>LT$, observe that $R_{dis}(\tau)=R_{uu}(\tau)$ with a periodicity of $2T$.

2.3.4.2 Average power spectral density

Consider the computation of the PSD of a baseband CPM signal using the autocorrelation function. Since $u(t)$ is not stationary, it is necessary to average the autocorrelation along $\tau=t_1-t_2$ to form an average representation of $R_{uu}(t_1,t_2)$. The Fourier transform pair of (2.1.8) can now be used to get what will be referred to as the average PSD $S_{uu}(f)$. The numerical solution for $S_{uu}(f)$ depends on which case is being dealt with, i.e., case A (h integer) or case B (h non-integer). It has been shown in [33][34] that for case A, the exact expression for the average PSD is given by

$$S_{uu}(f) = 2\,\Re\left\{\int_0^{LT} R_{uu}(\tau)\,e^{-j2\pi f\tau}\,d\tau + \frac{e^{-j2\pi fLT}}{1-C_a\,e^{-j2\pi fT}}\int_0^{T} R_{uu}(\tau+LT)\,e^{-j2\pi f\tau}\,d\tau\right\}. \tag{2.3.33}$$

This expression was derived from (2.3.25) and is valid under the same constraints. For the B case, since $R_{con}(\tau)$ is of length LT and $R_{dis}(\tau)$ is periodic

$$S_{con}(f) = 2\,\Re\left\{\int_0^{LT} R_{con}(\tau)\,e^{-j2\pi f\tau}\,d\tau\right\}, \tag{2.3.34}$$

$$S_{dis}(f) = \sum_{i=-\infty}^{\infty} |d_i|^2\,\delta(f-\tfrac{i}{T_{dis}}), \tag{2.3.35}$$

where the $|d_i|^2$ are the Fourier series coefficients given by

$$|d_i|^2 = \frac{1}{T_{dis}}\int_0^{T_{dis}} R_{dis}(\tau)\,e^{-j\left(\frac{2\pi i\tau}{T_{dis}}\right)}\,d\tau\,. \tag{2.3.36}$$

The cycle period T_{dis}, equals T or $2T$ according to whether h is even or odd, and of course $S_{uu}(f)=S_{con}(f)+S_{dis}(f)$. Figures 2.10 and 2.11[5] show the average PSD of the examples illustrated in Figs. 2.9 and 2.10 representing case A and B respectively.

[5]Formally $S_{con}(f)$ and $S_{dis}(f)$ cannot be shown on the same graph since $S_{dis}(f)$ is not a density. In this graph, the amplitude of the spectral lines of $S_{dis}(f)$ are set to be equal to the integral of the delta function at that frequency and represents the power at that frequency.

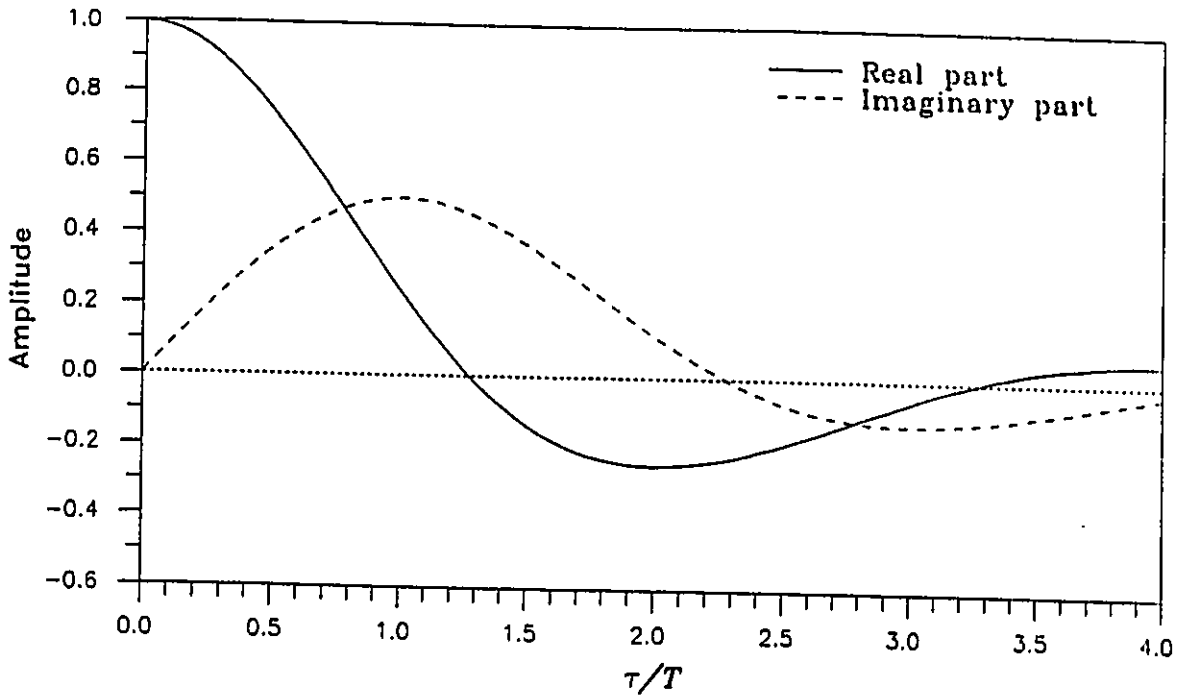

Fig. 2.8. MSK autocorrelation function with symbol probability P_{-1}=.25, P_{+1}=.75.

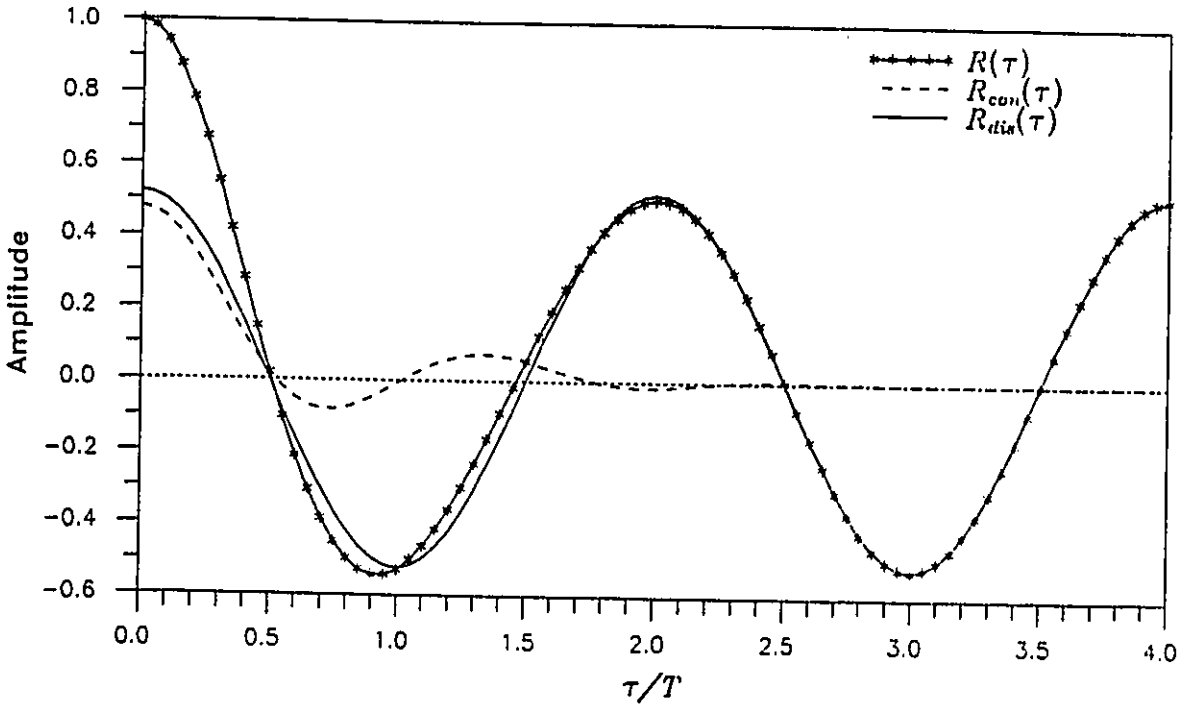

Fig. 2.9. Binary 3N3CR autocorrelation function with equally distributed data, h=1 and α=0.5.

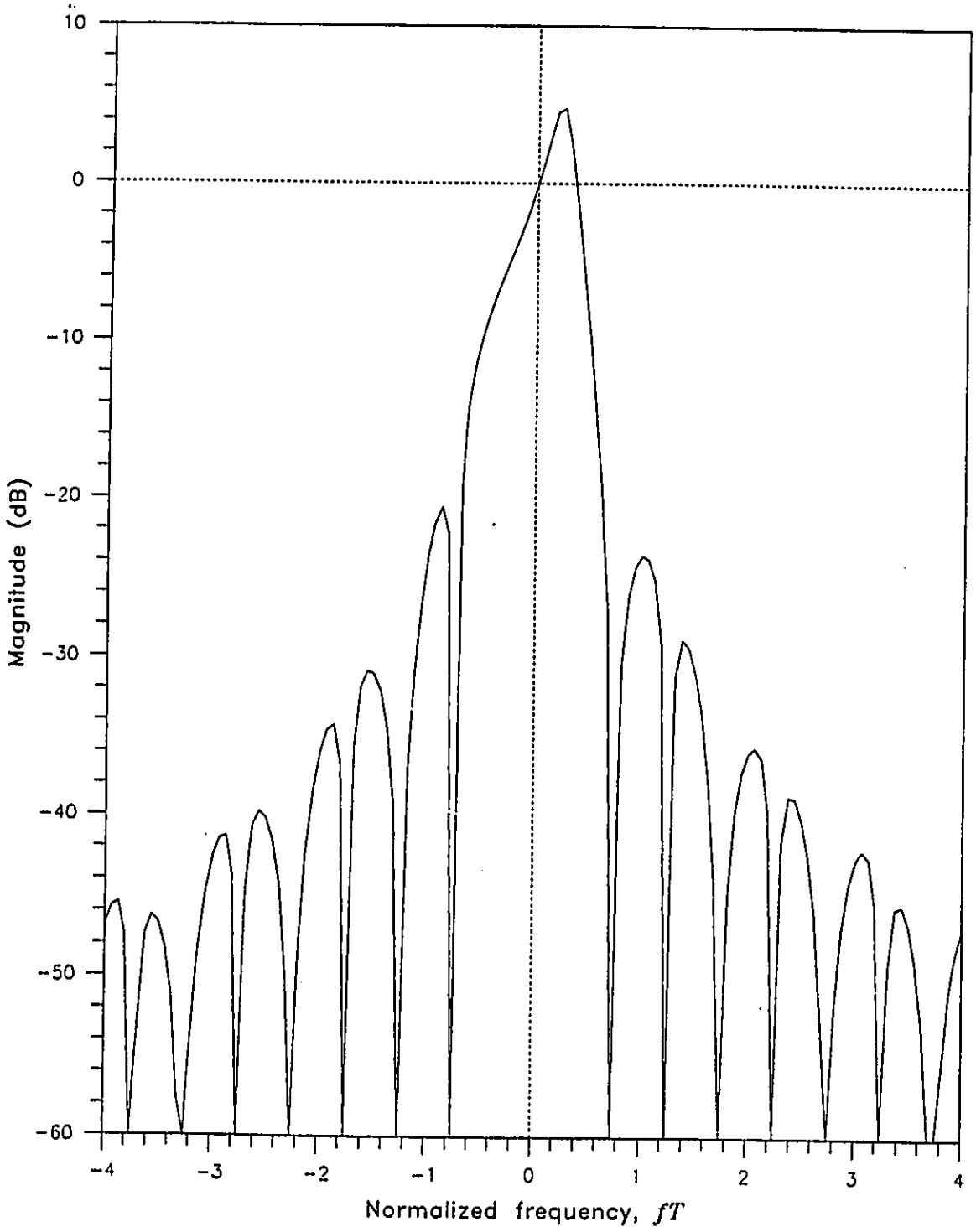

Fig. 2.10. Average PSD of MSK with symbol probability P_{-1}=.25, P_{+1}=.75.

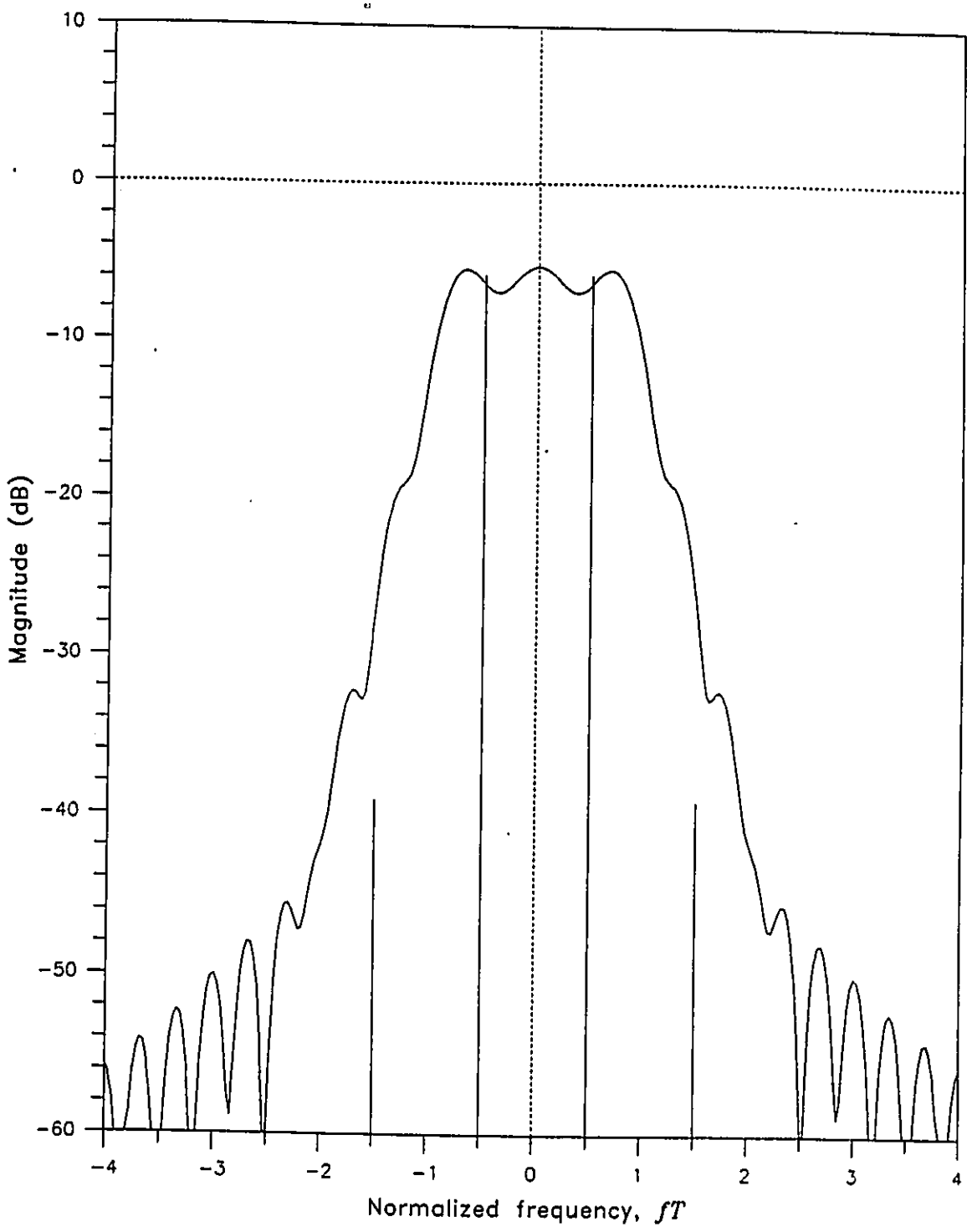

Fig. 2.11. Average PSD of binary 3N3CR with equally distributed data, h=1 and α=0.5.

2.4 Symbol Synchronization

The ability to efficiently detect a digital sequence often depends on obtaining a timing signal. In many studies, perfect synchronization information is assumed to be available. In practice however, this is not the case. As shown in Fig. 2.5, the timing signal is usually derived from the received signal itself which means that the synchronizer will be affected by the same distortion that is affecting the detection processor. Therefore, we face the problem of estimating the sampling instants from a signal disturbed by additive and multiplicative noise. A general approach is to use the maximum *a Posteriori* (MAP) criterion which can be adapted to the symbol synchronization problem. The approach will be briefly discussed and the complexity of using it in a fading environment will be considered. Afterwards, the reader will be introduced to the approach that is used here as well as some important characteristics related to it. This will be done by first establishing the role of the continuous and discrete part of the spectrum in synchronization. Once this is understood, the synchronizer structure used to solve the problem will be presented.

2.4.1 Maximum *a Posteriori* Approach

The timing recovery problem over the AWGN channel using the MAP approach has been studied in [36] for a general partial response scheme. The likelihood function averaged over all equiprobable outcomes $\underline{a}$ for estimating the timing error ϵ is given by

$$L(\hat{\epsilon}) = \frac{1}{D} \sum_{m=1}^{D} \cosh \left\{ \frac{1}{N_0} \int_{\hat{N}T} r(t)\, s(t,\underline{a}_m,\hat{\epsilon})\ dt \right\} \tag{2.4.1}$$

where D=(number of initial phases of the signal)$_{\text{modulo } 2\pi} \times 2^N$, $\hat{\epsilon} \in [0,T]$ is an estimate of ϵ, N is the length of the sequence in symbol periods and $\underline{a}_m$ is one of the possible transmitted sequences of length NT. To derive this expression, it is assumed that

1) the eye opening of a coherently demodulated CPM signal is symmetrical with respect to the time axis,

2) an AWGN channel with double-sided spectral density $\frac{N_0}{2}$ Watts/Hertz,

3) carrier phase synchronization, and

4*) all signal trajectories are equiprobable.

The synchro-position is the value of $\hat{\epsilon}$ that maximizes $L(\hat{\epsilon})$. A digital implementation of (2.4.1) will require quantization of $\hat{\epsilon}$ and a direct implementation would lead to a practically unacceptable solution due to hardware complexity (complexity increases exponentially with N) [36].

For the FFF channel, the timing error likelihood function must be derived according to the equivalent complex received signal

$$v(t) = c(t)\, u(t,\underline{a},\epsilon) + n(t), \qquad 0 \le t \le T, \tag{2.4.2}$$

where $c(t)=|c(t)|\, e^{j\theta(t)}$, $n(t)$ are complex gaussian processes and ϵ is again the timing error. As was discussed in Chapter 1, estimation of $\theta(t)$ in a FFF channel is almost impossible because of the rapidity of the phase fluctuations. Thus, even if the noise $n(t)$ is absent, the received signal would still be a random process if NT is in the order of magnitude or larger than the coherent time of the channel. So the problem is one of estimating a random process in noise with a composite hypotheses in $\underline{a}$, $\theta(t)$ and $|c(t)|$ [30]. The solution to this problem is not in the objectives of this thesis and therefore, will not be investigated. The implementation of such a synchronizer is probably even more complicated than the one discussed for the AWGN channel. Therefore, a simpler synchronizer is needed. A candidate synchronizer is developed in the next section.

2.4.2 Nonlinear Spectral Line Method

One common way of obtaining a timing signal from a modulated signal is to try to regenerate it at the receiver by removal of the modulation, fully or partially. This can often be accomplished through the use of a nonlinearity. This will yield an imperfect timing signal if the modulation cannot be fully removed, and the result is a degraded detection performance. The choice of the nonlinearity to achieve the best performance is a very difficult problem; fortunately simple operations often give

adequate performance. One particular class of nonlinearity often encounter is the instantaneous or zero-memory nonlinearity defined by an operator $\zeta[\cdot]$ linking the input $u(t)$ and the output $u'(t)$ by

$$u'(t) = \zeta[u(t)]. \tag{2.4.3}$$

The power law devices are members of this class and the special case where the power is a positive integer is of particular interest for a CPM scheme with rational modulation index $h=\frac{2k}{p}=\frac{\kappa}{\mu}$ (κ and μ relatively prime integers). In particular, the operator $\zeta[\cdot]=(\cdot)^{\mu}$ applied to the complex envelope $u(t,\underline{a})$ yields

$$u'(t,\underline{a}) = \left(e^{j2\pi\frac{\kappa}{\mu}\int_0^t \sum_i a_i\, g(t-iT)\, d\tau} \right)^{\mu}$$

$$u'(t,\underline{a}) = e^{j2\pi\kappa\int_0^t \sum_i a_i\, g(t-iT)\, d\tau}. \tag{2.4.4}$$

Looking at this last expression, it is evident that $u'(t,\underline{a})$ is also a CPM signal but with integer modulation index κ. From §2.3, it can be seen that $u'(t,\underline{a})$ will exhibit discrete components in its spectrum with frequencies separated by the symbol rate. Here, CPM schemes with modulation index of the form $h=\frac{\kappa}{\mu}=\frac{1}{M}$ will be studied, and therefore the signal $u'(t,\underline{a})$ with modulation index $h=1$ will be studied extensively. Also, the results for the Nyquist III pulse shaping will be emphasized and the advantages relative to other schemes will be shown. This will also indicate potential schemes that might be suitable for the given synchronizer structure.

2.4.3 Power in the Discrete Components

The discrete components in $S_{uu}(f)$ represent the timing information signal. Obviously, it is desirable to have as much power as possible in those discrete components to mitigate the effects of noise, and although it is not a sufficient condition to ensure good synchronizer performance, it is strongly believed that it is a necessary condition for bandwidth efficient schemes. So, the first concern here is to examine the total power available. As (2.3.35) indicates, the power is spread over the

spectrum in an infinite number of discrete components in general. The sum of the $|d_i|^2$ in (2.3.35) is simply the periodic autocorrelation function evaluated at $\tau=0$, thus

$$\text{Total power in discrete components} = R_{dis}(0) = \sum_{i=-\infty}^{\infty} |d_i|^2. \tag{2.4.5}$$

An expression for $R_{dis}(0)$ in terms of the signal parameters is desirable so that the parameters that significantly affect the results can be identified. Using $R_{dis}(\tau)$ definition, (2.3.30), and (2.3.19) with h integer, it is found that

$$R_{dis}(0) = \left\langle m_u(t+\tau)\, m_u^*(t) \right\rangle\Big|_{\tau=0}$$

$$= \frac{1}{T}\int_0^T \left(\prod_{i=1-L}^{0} \sum_{\substack{k=-(M-1) \\ k \text{ odd}}}^{(M-1)} P_k\, e^{j2\pi hkq(t-iT)} \right) \left(\prod_{n=1-L}^{0} \sum_{\substack{m=-(M-1) \\ m \text{ odd}}}^{(M-1)} P_m\, e^{j2\pi hmq(t-nT)} \right)^* dt$$

$$R_{dis}(0) = \frac{1}{T}\int_0^T \prod_{i=1-L}^{0} \sum_{\substack{k=-(M-1) \\ k \text{ odd}}}^{(M-1)} \sum_{\substack{m=-(M-1) \\ m \text{ odd}}}^{(M-1)} P_k P_m\, e^{j2\pi h(k-m)q(t-iT)}\, dt. \tag{2.4.6}$$

This expression is in general difficult to evaluate because of the product term and the nonlinear nature of the exponential function. However, for the particular case $L=1$ and $q(t)=\frac{t}{2T}$,

$$R_{dis}(0) = \frac{1}{T} \sum_{\substack{k=-(M-1) \\ k \text{ odd}}}^{(M-1)} \sum_{\substack{m=-(M-1) \\ m \text{ odd}}}^{(M-1)} P_k P_m \int_0^T e^{j2\pi h(k-m)t/2T}\, dt$$

$$= \sum_{\substack{k=-(M-1) \\ k \text{ odd}}}^{(M-1)} P_k^2 \geq \frac{1}{M}\,. \tag{2.4.7}$$

This well-known result [31] was easy to derived because the argument of the exponential in (2.4.6) is a linear function, and as a result there will be only M discrete lines in $S_{dis}(f)$. The minimum is reached when the a_i's are equally distributed and even though a general solution of (2.4.6) in terms of the probability density function of the a_i is not known, this observation is expected to be true for most

schemes. Therefore it is expected that the total discrete component power is minimum for equally distributed data when everything else is fixed. The solution of (2.4.6) was found using numerical methods. Tables 2, 3, and 4 show the results for a few time-limited pulse shapes (see Appendix A) with M=2, 4 and 8.

Table 2. Power in the discrete components for time-limited pulse shape with equally distributed data and M=2.

Pulse Shape	$R_{dis}(0)$		
	L=1	L=2	L=3
REC	0.500	0.125	3.125×10^{-2}
HCS	0.625	0.319	0.125
TRI	0.687	0.382	0.177
RC	0.720	0.442	0.222
CRC	0.732	0.464	0.239

Table 3. Power in the discrete components for time-limited pulse shape with equally distributed data and M=4.

Pulse Shape	$R_{dis}(0)$		
	L=1	L=2	L=3
REC	0.25	1.6×10^{-2}	9.8×10^{-4}
HCS	0.44	3.9×10^{-2}	1.1×10^{-2}
TRI	0.48	5.9×10^{-2}	1.6×10^{-2}
RC	0.54	0.12	2.2×10^{-2}
CRC	0.57	0.15	2.5×10^{-2}

Table 4. Power in the discrete components for time-limited pulse shape with equally distributed data and M=8.

Pulse Shape	$R_{dis}(0)$		
	L=1	L=2	L=3
REC	0.125	1.9×10^{-3}	3×10^{-5}
HCS	0.31	5.9×10^{-3}	3.9×10^{-4}
TRI	0.34	7.9×10^{-3}	6.7×10^{-4}
RC	0.42	1.3×10^{-2}	2.2×10^{-3}
CRC	0.46	1.8×10^{-2}	3.3×10^{-3}

Table 5. Power in the discrete components for TFM and N32.

Pulse Shape	$R_{dis}(0)$		
	M=2	M=4	M=8
TFM (L=5)	0.125	9.7×10^{-2}	2.9×10^{-2}
N32 (L=3)	0.57	0.316	0.165

From these results, it is observed that the power in the discrete components is related to the pulse shape peak amplitude/flatness or equivalently, the deviation of the carrier from its nominal frequency. Since the flattest possible pulse shape is LREC, it has the least power in $R_{dis}(0)$ (it also has the narrowest main lobe in its spectrum). Note that some pulse shapes still have good power in their discrete components for M=4 and that L=1 is the only potentially attractive case for M=8. As an

indication of the minimum power involved, $R_{dis}(0)$ for LREC was computed for $L \leq 5$. From data analysis, it was found that a very good approximation for the total discrete tone power is given by

$$R_{dis}(0) \simeq \left(\frac{1}{M}\right)^{2L-1}. \tag{2.4.6}$$

This indicates that $R_{dis}(0)$ is a decreasing function of M and L. This behavior is true in most cases for a fixed integer h and $g(t)$. Table 5 shows $R_{dis}(0)$ for two particular band-limited pulse shapes. A similar study was conducted for Nyquist III pulse shapes to establish its potential performance from the synchronization point of view. For band-limited pulse shapes, (2.4.6) was computed with $M=2$, 4, 8 and $L=1$, 3, 5 as a function of the excess bandwidth α with uniform probability density function for the a_i's. The results are shown in Fig. 2.12 for N3CR pulse shaping. Observe that for practical pulse shape length, the total discrete tone power is approximately equal to $1/M$, and thus almost independent of L. The degradation due to longer pulse shape length is mostly apparent for low values of excess bandwidth and seems to be lower bounded. Also note that the main lobe flatness is again related to $R_{dis}(0)$ in the same way that time-limited pulse shape were (see Fig. 2.6). This observation and the constraint (2.3.3) explain why the pulse shapes with large excess bandwidth are less affected by an increase in L. The behavior of $R_{dis}(0)$ is approximatly the same for different M when L is increased. To check the performance of other Nyquist III pulse shapes, it is possible to select for example, $M=2$, $L=1$ and expect that the behavior between the different Nyquist III pulses will be approximatly the same for other M and L. Figure 2.13 illustrates $R_{dis}(0)$ behavior for six Nyquist III pulses. The discrete tones total power is similar for all pulses except the N3ME1 pulse. Although this last pulse is the one that would have the most power available for synchronization, its spectral efficiency is dramatically worst than the others at $\alpha \simeq .9$, and for this reason N3ME1 is not a good choice for many applications. This last figure also shows that N3CR is the one with the smallest $R_{dis}(0)$ in most of the excess bandwidth range (0 to $\simeq .85$). This is why most of the results will be presented for the N3CR since it seems to represent the minimum discrete component power for the Nyquist III pulse shapes shown here, and therefore demonstrates "worst case" performance for this class of waveform.

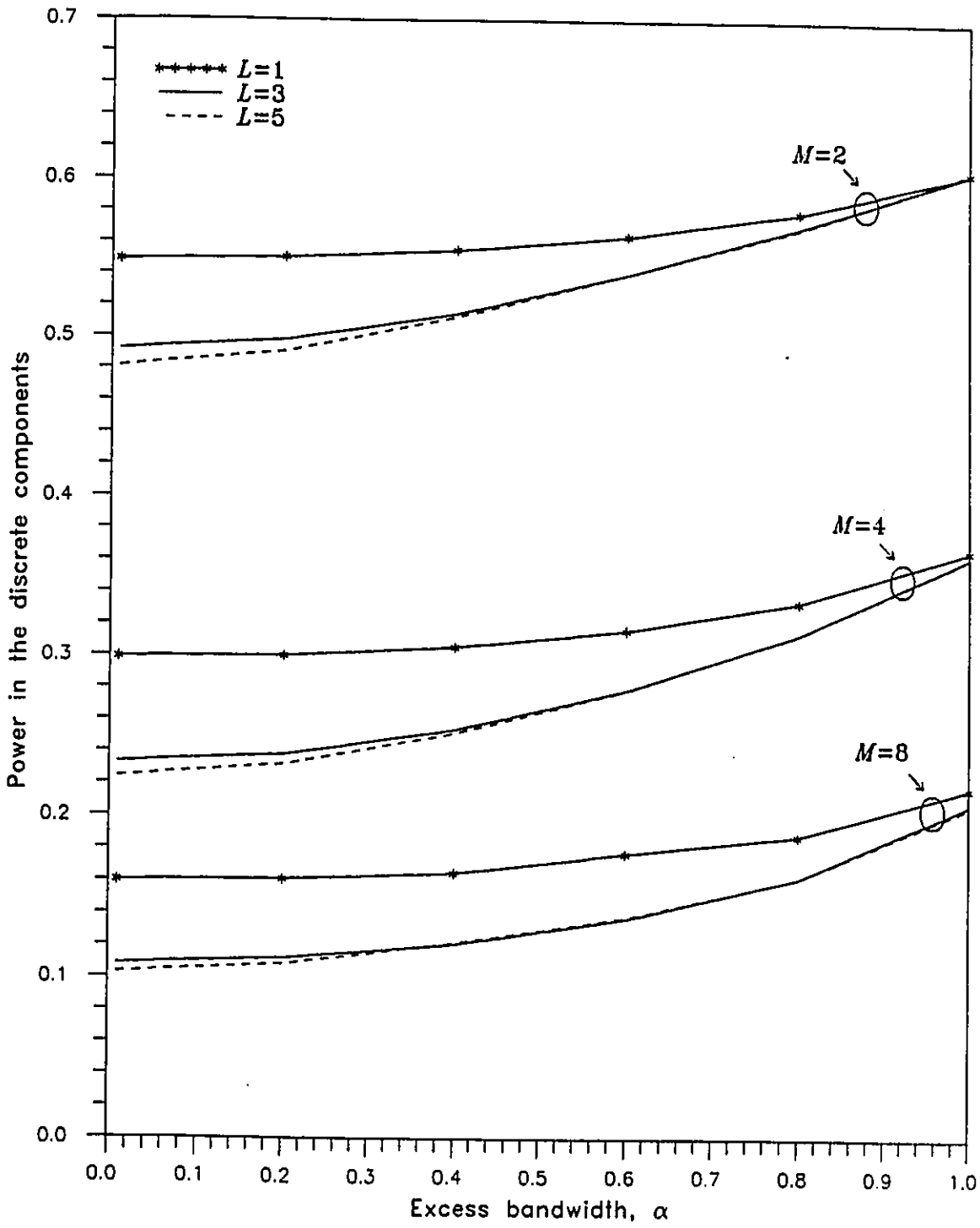

Fig. 2.12. Power in the discrete components for CPM N3CR M=2, 4, 8 and L=1, 3, 5 with equally distributed data as a function of α.

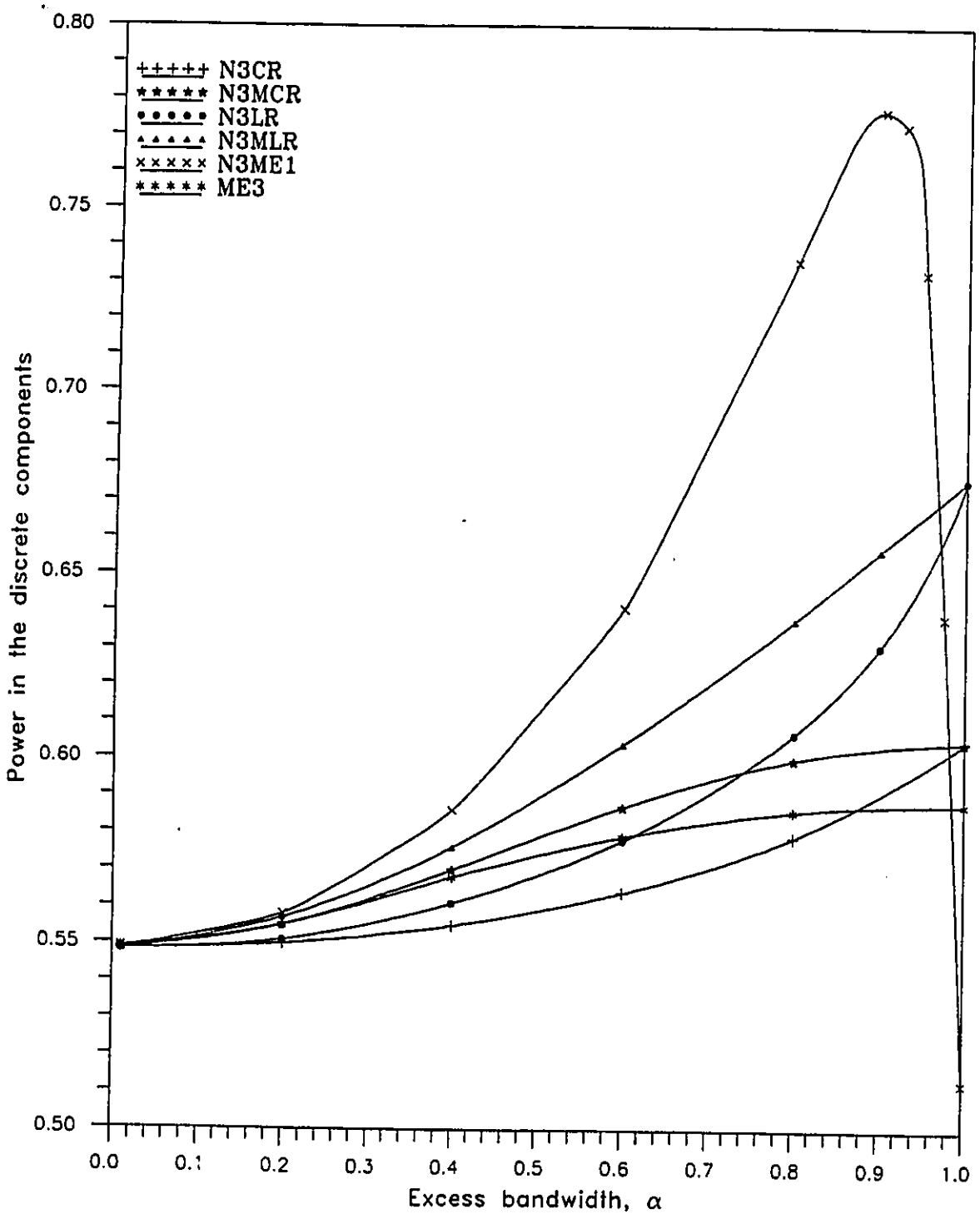

Fig. 2.13. Power in the discrete components for different Nyquist III pulse shapes with M=2, L=1 and equally distributed data as a function of α.

The good results obtained for some time-limited and Nyquist III pulse shape's discrete tone total power do not fully justify by themselves the use of those pulse shape for synchronization reasons in the context of multitone combination. Two other factors must be taken into account: the remaining power distribution $S_{con}(f)$ and the phase relationships between the discrete tones d_i. The next section is concerned with the former factor while the latter is discussed in §3.2.

2.4.4 Tone to Self-Noise Ratio

In the preceding section, the power available in the discrete components was examined. This power is distributed between several discrete tones and contains the timing information that is going to be used to generate a timing signal at the symbol rate. However the nonlinearity does not remove all the modulation and the result is a continuous spectrum $S_{con}(f)$ present at the zero memory nonlinearity output. This spectrum represents noise for the synchronizer and is present in the system even in a perfect channel. This noise will be called self-noise throughout the thesis. In general, part of this noise will degrade the synchronizer performance since it is processed with the timing signal up to the system output.

Obviously the total power in the continuous spectrum is given by $R_{con}(0)$. This power is distributed across the frequency axis depending on the modulation index, the number of levels M, the pulse shape, the pulse shape length L and the probability density function of the data. General observation reveals that the continuous part of the spectrum $S_{con}(f)$ roughly tracks the magnitudes of the discrete frequency components. The strongest frequency components are in most cases located at the frequencies $f=\pm h/2T$ in the binary case, at $f=\pm h/2T$, $\pm 3h/2T$ in the quaternary case and at $f=\pm h/2T$, $\pm 3h/2T$, $\pm 5h/2T$, $\pm 7h/2T$ in the 8-ary case. Thus in general for $h=1$, the M strongest tones are located near the carrier frequency following approximately the shape of the continuous spectrum in amplitude. A narrowband filter centered around one of these tones must reject most of $S_{con}(f)$ in order to yield a good estimate of a multiple of the symbol rate. Let the tone to self-noise ratio (TSNR) at the output of one of these bandpass filters be defined as

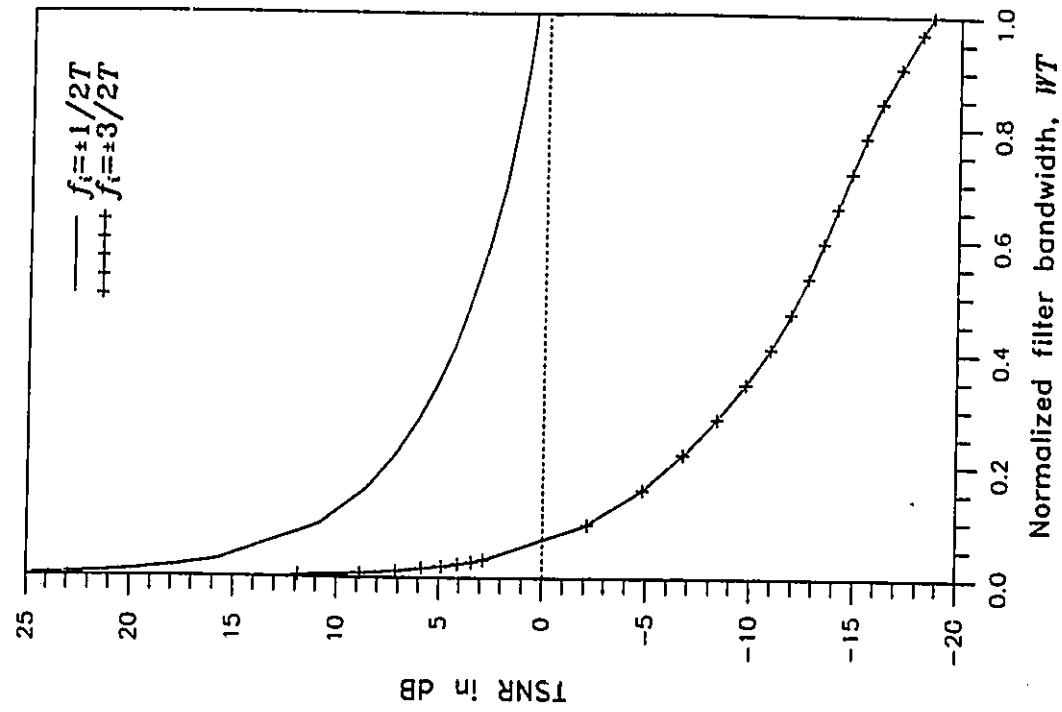

Fig. 2.15. TSNR vs. WT for binary 3N3CR.

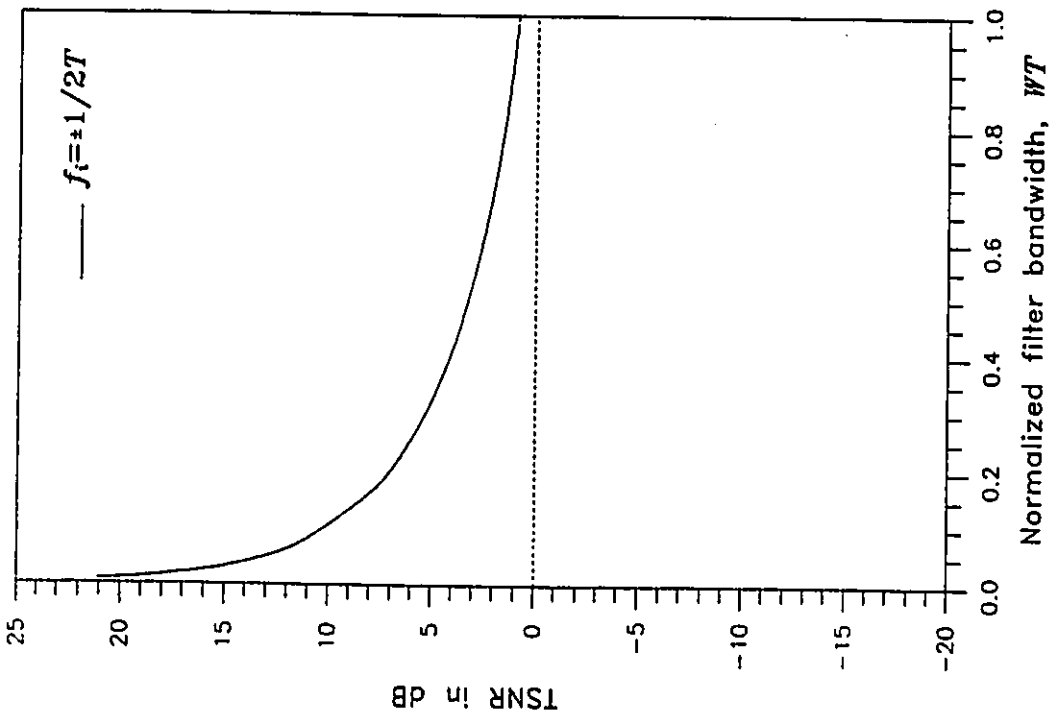

Fig. 2.14. TSNR vs. WT for squared MSK.

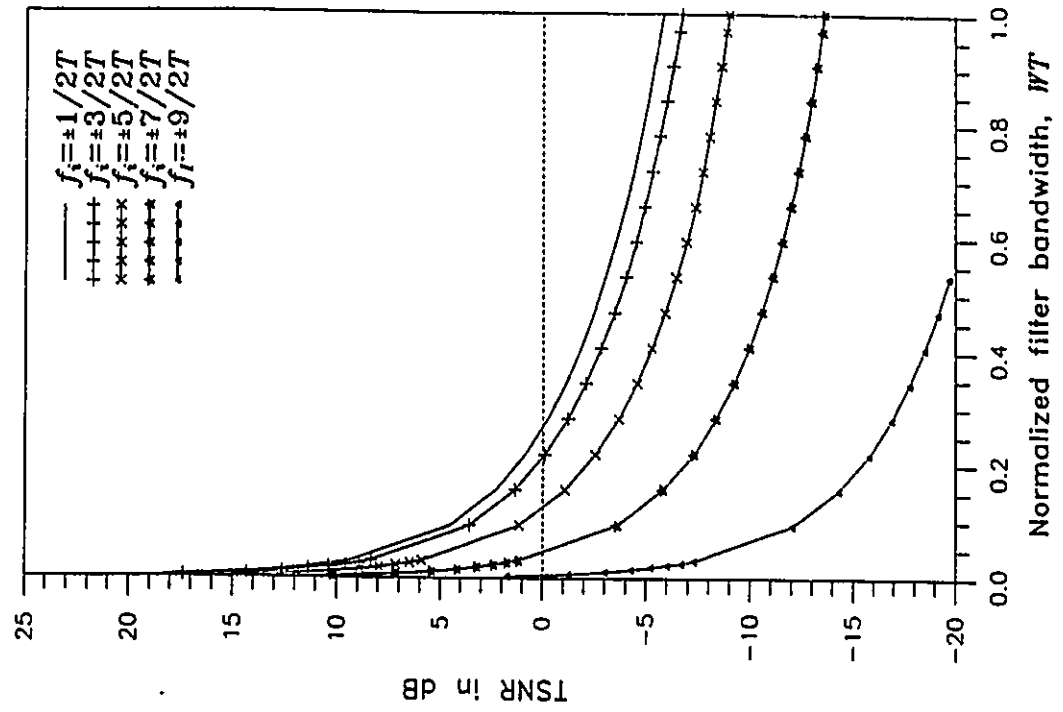

Fig. 2.17. TSNR vs. WT for 8−ary 3N3CR.

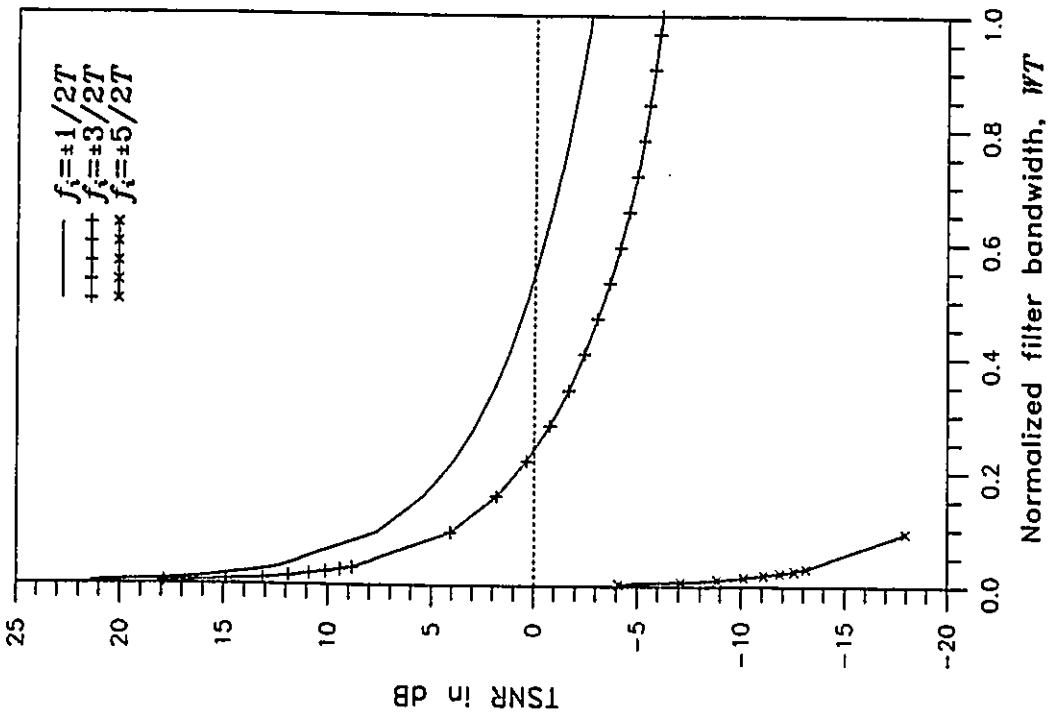

Fig. 2.16. TSNR vs. WT for quaternary 3N3CR.

$$\mathrm{TSNR}_i \equiv 10 \log_{10} \frac{|d_i|^2}{T \int_{-W/2}^{W/2} S_{con}(f_i+f)\, df}, \tag{2.4.9}$$

where f_i is the location of the discrete frequency component, $|d_i|^2$ is the corresponding magnitude squared, and W the filter bandwidth. The TSNR is given in decibels. Figure 2.14 shows the TSNR for MSK with equally distributed data. In this simplest case the value of TSNR as $WT \to \infty$ is 0dB. Figures 2.15, 2.16 and 2.17 give TSNR calculations for 3N3CR, $h=1$, $\alpha=.5$ with $M=2$, 4, and 8, respectively at $f_i = \pm 1/2T, \ldots, \pm(M+1)/2T$. Observe that the TSNR is relatively good for the M tones of a given scheme and that the reduction in the strengths of the remaining tones decreases as M increases. Verification of this behavior as a function of the excess bandwidth might reveal some particular scheme where the TSNR is especially good. The choice of $\alpha=.5$ results from the fact that this scheme has relatively good bandwidth efficiency [22] and small $R_{dis}(0)$ (see Fig. 2.13).

2.4.5 Synchronizer Structure

The description of the signals given in this chapter allows now to set the objective of the synchronizer. In short, it is to perform multitone recombination timing recovery for CPM transmitted over a fast flat-fading channel. The multitone recombination must provide a good timing signal at the rate $1/T$ at the synchronizer output. The synchronizer is in a baseband form and will thus be operating on a complex signal. The structure is a modified version of a bandpass synchronizer studied in a few papers [37][38] that was first proposed by de Buda [14]. The synchronizer structure is presented in Fig. 2.18,

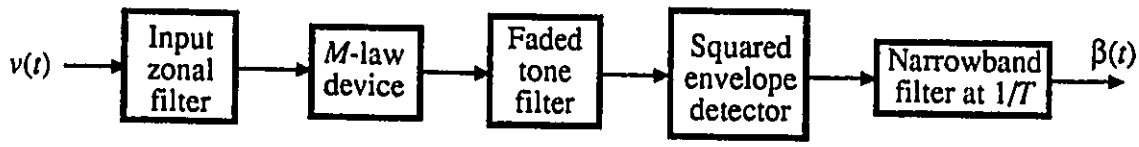

Fig. 2.18. Synchronizer structure.

where $v(t)$ is the received lowpass signal and $\beta(t)$ is an estimate of the symbol rate frequency and phase. The input zonal filter simply removes the extraneous (out of band) additive noise components while causing negligible distortion to the information bearing part of $v(t)$. The transmitted signal has modulation index $1/M$ and the M-law nonlinearity produces a signal with faded timing information. The purpose of the faded tone filter is to remove as much timing noise as possible. This noise term will be defined in the next chapter. The filter is an M-passband filter with passband center frequencies at odd multiples of $1/2T$. This will allow M tones to pass the filter without being attenuated. The following block is again a zero memory nonlinearity device with operator $\zeta[\cdot]=|\cdot|^2$ with complex input but real output signal. This nonlinearity will perform the tone recombination at the symbol rate $1/T$ of the M tones of the faded tone filter output and will compensate for the frequency shift of the same M tones. Note that even though the input is complex, the synchronizer has not been describe in terms of an I-Q channel model. This is because the I-Q channels of the synchronizer are not related to the I-Q information channels of $u(t,\underline{a})$ since $v(t)$ can be a non-coherent signal with this synchronizer structure. ■

Chapter 3

SYSTEM ANALYSIS

3.1 Analytic Model

The analysis pursued in this chapter is based on an overall system model. This global model is itself based on the three components described in the previous chapter, i.e., the channel model, the modulation scheme and the synchronizer. Linking together those components leads to the system model illustrated in Fig. 3.1a. The transmitter is viewed as a complex baseband modulator (Fig. 2.5) followed by an up-converter to generate the real signal $s(t,\underline{a})$. This up-converter is a pair of quadrature-driven mixers. The signal $s(t,\underline{a})$ is sent through a fast flat-fading (FFF) channel as explained in §2.2. At the receiver's input, the signal is first filtered to reduce the AWGN power without distorting the faded information signal. The filter output signal $r(t)$[6] is then down-converted to complex baseband with a non-coherent I-Q down-converter composed of quadrature mixers and data filters to remove unwanted mixer products. The operation yields the complex signal $v(t)$ which is further processed to give an estimate of the data sampling instant. Such a system however, does not lend itself easily to mathematical analysis because of the Rician channel characteristics and the two nonlinear devices in the system. So to ease the analysis, the Rician channel is replaced by the Rayleigh channel which can be regarded as the worst case instance of the Rician channel. This facilitates the use of the complex envelope representation of the real fading process as described in §2.1. The up and down conversion can be removed by introducing the equivalent lowpass representation of $h'(t)$ i.e., $c(t)=c'(t)$. The equivalent processing in terms of the complex lowpass equivalent signals is illustrated in Fig. 3.1b. This model is more convenient for the analysis and will be employed throughout the subsequent sections.

[6] The $\underline{a}$ dependence of $r(t)$ has been omitted because the estimation of this sequence is not of interest here.

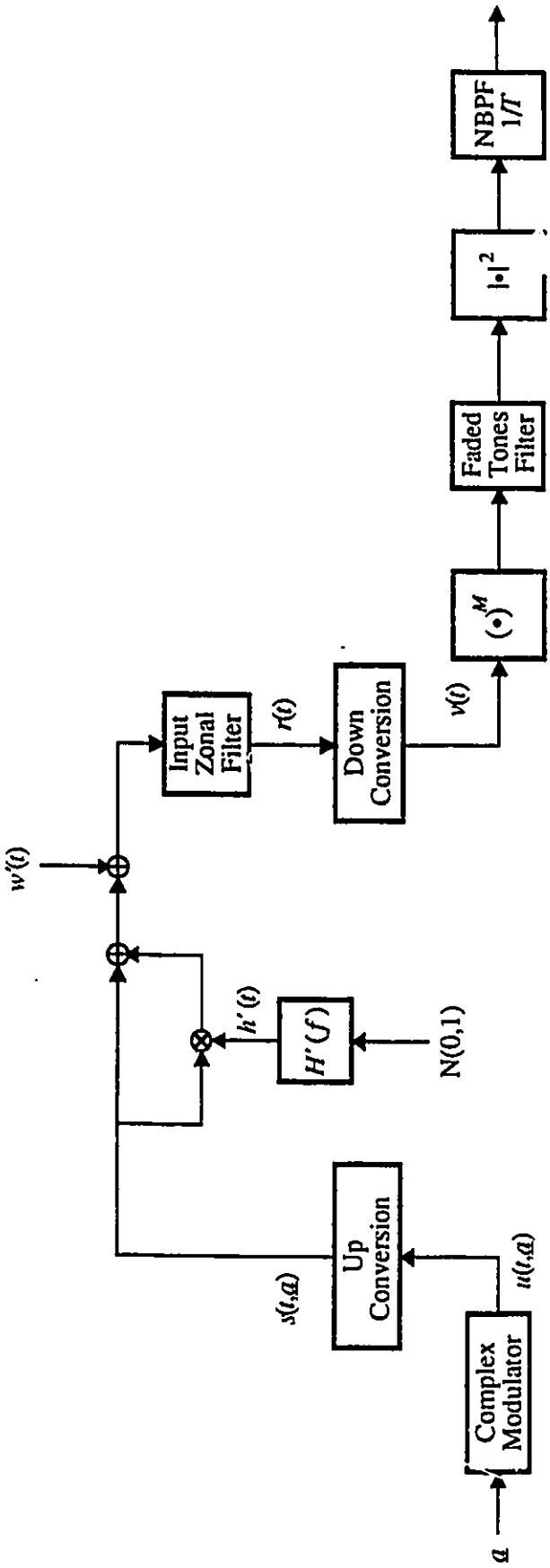

Fig. 3.1. a) Actual system model

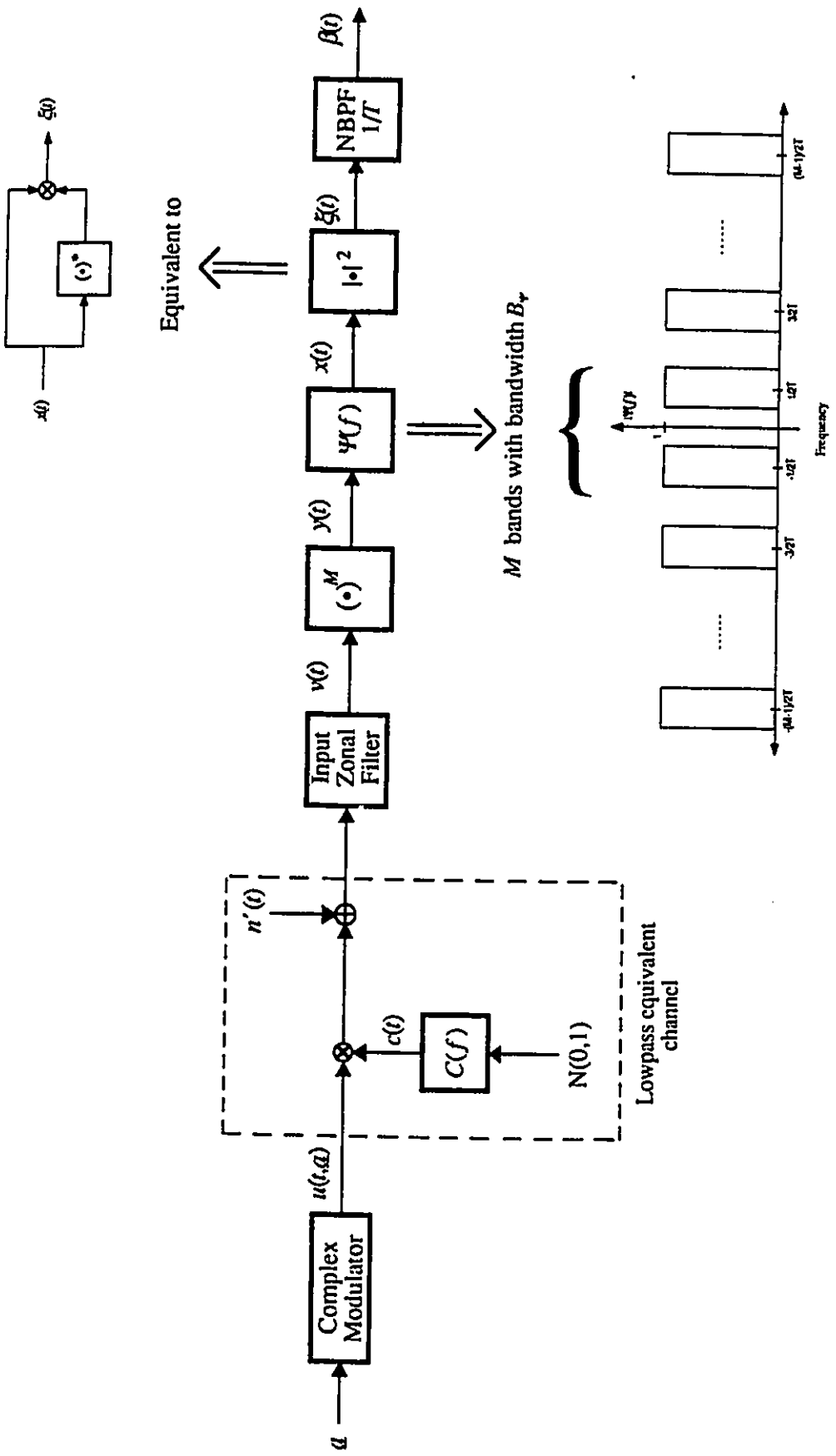

Fig. 3.1. b) Analytic model

3.2 Faded Timing Signal

3.2.1 M-law Device Output Signal

The model of Fig 3.1b begins with the complex lowpass equivalent of the modulated signal $u(t,\underline{a})=\sqrt{P}\ e^{j\phi(t,\underline{a})}$ (complex CPM signal with modulation index $1/M$), where for notation simplification it was assumed, without loss of generality, $P=1$. This signal is sent through a Rayleigh channel viewed as a multiplicative noise process $c(t)=|c(t)|\ e^{j\theta(t)}$ (complex Gaussian random process), where $|c(t)|$ is Rayleigh distributed over the interval $[0,\infty]$ and $\theta(t)$ uniformly distributed over $[0,2\pi]$. Note that the information signal is affected by an additive phase noise $\theta(t)$ and has now a Rayleigh distributed envelope instead of a constant envelope. On top of this, is the additive Gaussian noise process given by $n'(t)=|n'(t)|\ e^{j\nu'(t)}$ (complex Gaussian random process) where $|n'(t)|$ is Rayleigh distributed over the interval $[0,\infty]$ and $\nu'(t)$ uniformly distributed over $[0,2\pi]$. The resulting received signal is of the form $c(t)\ u(t,\underline{a})+n'(t)$ passed through an input zonal filter that bandlimits the additive noise process power, leaving negligible distortion on the faded signal part. Thus

$$v(t) = c(t)\ u(t,\underline{a}) + n(t), \tag{3.2.1}$$

where $n(t)$ is bandlimited to $\left[\frac{-B_z}{2},\frac{B_z}{2}\right]$ with a rectangular shape. The processes $u(t,\underline{a})$, $c(t)$ and $n(t)$ are assumed to be independent with $u(t,\underline{a})$ cyclostationary and $c(t)$, $n(t)$ stationary ergodic. The received signal $v(t)$ is therefore cyclostationary in general and one can easily see that it has zero mean. The process $v(t)$ is then passed throught the M-law nonlinearity to yield the process

$$y(t) = \left[v(t)\right]^M = \left[c(t)\ u(t,\underline{a}) + n(t)\right]^M. \tag{3.2.2}$$

Using the binomial theorem, $y(t)$ can be rewritten as

$$y(t) = \sum_{\iota=0}^{M} \binom{M}{\iota} c^{\iota}(t)\ u^{\iota}(t,\underline{a})\ n^{M-\iota}(t), \tag{3.2.3}$$

where $\binom{M}{\iota} = \frac{M!}{\iota!\,(M-\iota)!}$. Among the $M+1$ terms constituting $y(t)$, three types of terms are identified: the signal×signal (s×s) term ($\iota=M$), the signal×noise (s×n) terms ($\iota=1,\ 2,\ \cdots,\ M-1$) and the

noise×noise (n×n) term ($\iota=0$). In (3.2.3), observe that the s×s term of $y(t)$ is the product between a CPM signal with unit modulation index, and the Mth power of a complex Gaussian process. This means that the tones present in $u^M(t,\underline{a})$ are amplitude and phase modulated. To better understand this, consider the following statistical characterization of the process $y(t)$. This characterization will show that the signal $y(t)$ contains a faded timing signal, and it will also provide a quantitative indication of the bandwidth required for the bandpass region of the faded tone filter. For obvious reasons, it is very difficult to derive the probability density function of $y(t)$. So to find an expression for the mean and autocorrelation function of the process $y(t)$, it is desirable to find a relationship between $y(t)$'s second-order properties and the second order properties of $u(t,\underline{a})$, $c(t)$, $n(t)$ which are known from Chapter 2[7]. Using the independence assumption on $u(t,\underline{a})$, $c(t)$ and $n(t)$, the expected value of $y(t)$ can be written as

$$\begin{aligned}
\mathbf{E}\Big\{y(t)\Big\} &= \mathbf{E}\left\{\sum_{\iota=0}^{M}\binom{M}{\iota}\, c^{\iota}(t)\; u^{\iota}(t,\underline{a})\; n^{M-\iota}(t)\right\} \\
&= \sum_{\iota=0}^{M}\binom{M}{\iota}\,\mathbf{E}\Big\{c^{\iota}(t)\; u^{\iota}(t,\underline{a})\; n^{M-\iota}(t)\Big\} \\
&= \sum_{\iota=0}^{M}\binom{M}{\iota}\,\mathbf{E}\Big\{c^{\iota}(t)\Big\}\,\mathbf{E}\Big\{u^{\iota}(t,\underline{a})\Big\}\,\mathbf{E}\Big\{n^{M-\iota}(t)\Big\}, \qquad (3.2.4)
\end{aligned}$$

where $\mathbf{E}\{\cdot\}$ denotes expectation over data symbols, multiplicative noise and additive noise. The expected value of $y(t)$ is thus given by a sum of products involving moments of the complex processes $u(t,\underline{a})$, $c(t)$ and $n(t)$. Looking at each of these moments separately, it can be seen that

$$\mathbf{E}\Big\{c^{\iota}(t)\Big\} = \mathbf{E}\Big\{|c(t)|^{\iota}\Big\}\,\mathbf{E}\Big\{e^{j\iota\theta(t)}\Big\} = \begin{cases} 1, & \iota = 0; \\ 0, & \iota = 1, 2, \cdots, M; \end{cases} \qquad (3.2.5)$$

[7] The autocorrelation function of $c(t)$ is simply the inverse Fourier transform of the Doppler spectrum which is usually found by channel measurements.

$$\mathbb{E}\left\{u^{\iota}(t,\underline{a})\right\} = \begin{cases} 1, & \iota = 0; \\ 0, & \iota = 1, 2, \cdots, M-1; \\ {}_{M}m_{u}(t), & \iota = M \text{ and } 0 \leq t \leq T, \end{cases} \tag{3.2.6}$$

with (see Chapter 2 §2.3.4.1)

$${}_{M}m_{u}(t) = \pm\prod_{i=1-L}^{0} \sum_{\substack{k=-(M-1) \\ k \text{ odd}}}^{M-1} P_k \, e^{j2\pi kq(t-iT)}, \tag{3.2.7}$$

and finally

$$\mathbb{E}\left\{n^{M-\iota}(t)\right\} = \mathbb{E}\left\{|n(t)|^{(M-\iota)}\right\} \mathbb{E}\left\{e^{j(M-\iota)v(t)}\right\} = \begin{cases} 0, & \iota = 0, 1, 2, \cdots, M-1; \\ 1, & \iota = M, \end{cases} \tag{3.2.8}$$

resulting in

$$\mathbb{E}\left\{y(t)\right\} = 0, \tag{3.2.9}$$

because the product $\mathbb{E}\left\{c^{\iota}(i)\right\} \mathbb{E}\left\{n^{M-\iota}(t)\right\}$ is always zero. With (3.2.5), it is explicitly seen in (3.2.4) that the periodic signal ${}_{M}m_{u}(t)$ vanishes because of the phase of the fading process. This phase variation will have to be removed from the s×s term to extract the timing information. If $u^{M}(t,\underline{a})$ is rewritten as a sum of its mean and its difference from the mean

$$u^{M}(t,\underline{a}) = {}_{M}m_{u}(t) + \Delta u^{M}(t,\underline{a}),$$

then it can be written that

$$y(t) = c^{M}(t) \, {}_{M}m_{u}(t) + \lambda(t) \tag{3.2.10}$$

where $\lambda(t)$ is the sum of $c^{M}(t)\Delta u^{M}(t,\underline{a})$ and all the s×n and n×n terms. Consider next the autocorrelation function of $y(t)$. Using basic definition,

$$R_{yy}(t_1,t_2) = \mathbb{E}\left\{y(t_1)\; y(t_2)^{*}\right\}$$

$$= \mathbb{E}\left\{\left[c(t_1)\; u(t_1,\underline{a}) + n(t_1)\right]^{M} \times \left(\left[c(t_2)\; u(t_2,\underline{a}) + n(t_2)\right]^{M}\right)^{*}\right\}$$

$$= \mathbf{E}\left\{\sum_{\iota=0}^{M}\binom{M}{\iota} c^{\iota}(t_1)\, u^{\iota}(t_1,\underline{a})\, n^{M-\iota}(t_1) \times \sum_{\eta=0}^{M}\binom{M}{\eta} c^{\eta}(t_2)^*\, u^{\eta}(t_2,\underline{a})^*\, n^{M-\eta}(t_2)^*\right\}$$

$$= \mathbf{E}\left\{\sum_{\iota=0}^{M}\sum_{\eta=0}^{M}\binom{M}{\iota}\binom{M}{\eta} c^{\iota}(t_1)\, c^{\eta}(t_2)^*\;\; u^{\iota}(t_1,\underline{a})\, u^{\eta}(t_2,\underline{a})^*\;\; n^{M-\iota}(t_1)\, n^{M-\eta}(t_2)^*\right\}$$

$$= \sum_{\iota=0}^{M}\sum_{\eta=0}^{M}\binom{M}{\iota}\binom{M}{\eta}\mathbf{E}\left\{c^{\iota}(t_1)\, c^{\eta}(t_2)^*\right\}\mathbf{E}\left\{u^{\iota}(t_1,\underline{a})\, u^{\eta}(t_2,\underline{a})^*\right\}\mathbf{E}\left\{n^{M-\iota}(t_1)\, n^{M-\eta}(t_2)^*\right\}, \tag{3.2.11}$$

where the notation $c^{\eta}(t)^*$ is equivalent to $\left\{[c(t)]^{\eta}\right\}^*$ [same for $n(t)$] and the independence assumption was used again. Thus, in general $R_{yy}(t_1,t_2)$ will be formed out of a sum of $(M+1)^2$ terms. The problem of estimating the joint moment of two complex Gaussian random processes, and similarly, the joint moment of two complex CPM signals must be addressed. It is shown in Appendix B that

$$\mathbf{E}\left\{z^{\iota}(t_1)\, z^{\eta}(t_2)^*\right\} = \begin{cases} \eta!\, R_{zz}^{\eta}(t_1,t_2), & \iota = \eta; \\ 0, & \iota \neq \eta, \end{cases} \tag{3.2.12}$$

where $z(t)$ is a zero mean complex Gaussian process and $R_{zz}(t_1,t_2)$ is the autocorrelation function of $z(t)$. Also in Appendix C it is shown that

$$\mathbf{E}\left\{u^{\iota}(t_1,\underline{a})\, u^{\eta}(t_2,\underline{a})^*\right\} = \begin{cases} {}_{\eta}R_{uu}(t_1,t_2), & \iota = \eta; \\ 0, & \iota \neq \eta,\ \iota - \eta \neq nM, \\ {}_{\iota,\eta}Q_{uu}(t_1,t_2), & \iota \neq \eta,\ \iota - \eta = nM, \end{cases} \tag{3.2.13}$$

where n is an integer, ${}_{\eta}R_{uu}(t_1,t_2)$ the autocorrelation function of $u(t,\underline{a})$ raised to the power η and

$${}_{\iota,\eta}Q_{uu}(t_1,t_2) = \prod_{i=\left\lfloor\frac{t_2}{T}\right\rfloor-L+1}^{\left\lfloor\frac{t_1}{T}\right\rfloor} \sum_{\substack{k=-(M-1) \\ k\ \text{odd}}}^{M-1} P_k\, e^{j2\pi hk\left[\iota q(t_1-iT)-\eta q(t_2-iT)\right]}, \tag{3.2.14}$$

with $\lfloor\cdot\rfloor$ denoting the largest integer smaller then or equal to. Regrouping the terms in (3.2.11) leads to

$$R_{yy}(t_1,t_2) = \sum_{\eta=0}^{M} \left(\frac{M}{\eta}\right)^2 \eta!\,(M-\eta)!\; R_{cc}^{\eta}(t_1,t_2)\; {}_{\eta}R_{uu}(t_1,t_2)\; R_{nn}^{M-\eta}(t_1,t_2), \tag{3.2.15}$$

where $R_{cc}(t_1,t_2)$ and $R_{nn}(t_1,t_2)$ are the autocorrelation functions of $c(t)$ and $n(t)$ respectively. The simplification from (3.2.11) to (3.2.15) is attributed to two factors: 1°) $c(t)$ and $n(t)$ are zero mean processes, and 2°) all the terms in $y(t)$ summation form i.e., in (3.2.4) are independent. Therefore, the s×s, s×n, and n×n terms are independent as well as the $(M-1)$ terms in s×n. $R_{yy}(t_1,t_2)$ in (3.2.15) is an important result linking the input and output autocorrelation functions of the M-law device. The same approach can be used for higher order nonlinearities leading to the same general form of $R_{yy}(t_1,t_2)$. The expression (3.2.15) can be averaged over one period of the process $u(t,a)$ in a similar fashion made in §2.3.4 to give

$$R_{yy}(\tau) = \left\langle R_{yy}(t+\tau,t)\right\rangle_t = \sum_{\eta=0}^{M} \left(\frac{M}{\eta}\right)^2 \eta!\,(M-\eta)!\; R_{cc}^{\eta}(\tau)\; {}_{\eta}R_{uu}(\tau)\; R_{nn}^{M-\eta}(\tau), \tag{3.2.16}$$

where $R_{cc}(\tau)=\langle R_{cc}(t+\tau)\rangle_t$, $R_{nn}(\tau)=\langle R_{nn}(t+\tau)\rangle_t$, and ${}_{\eta}R_{uu}(\tau)=\langle {}_{\eta}R_{uu}(t+\tau)\rangle_t$ for $t\in[0,T]$. $R_{yy}(\tau)$ can now be used to compute the PSD of $y(t)$. But before doing so, it is worthwhile decomposing ${}_{M}R_{uu}(\tau)$ into two components which give rise to the discrete and continuous spectral components:

$${}_{M}R_{uu}(\tau) = R_{dis}(\tau) + R_{con}(\tau) \tag{3.2.17}$$

such that $R_{yy}(\tau)$ is rewritten as

$$R_{yy}(\tau) = M!\left(R_{cc}^{M}(\tau)\; R_{dis}(\tau) + R_{cc}^{M}(\tau)\; R_{con}(\tau)\right) + \sum_{\eta=0}^{M-1} \left(\frac{M}{\eta}\right)^2 \eta!\,(M-\eta)!\; R_{cc}^{\eta}(\tau)\; {}_{\eta}R_{uu}(\tau)\; R_{nn}^{M-\eta}(\tau) \tag{3.2.18a}$$

$$R_{yy}(\tau) = M!\; R_{cc}^{M}(\tau)\; R_{dis}(\tau) + R_{\lambda\lambda}(\tau). \tag{3.2.18b}$$

The first two terms in (3.2.18a) are the s×s terms. Equation (3.2.18a) emphasizes that this term contains a faded timing signal term $R_{cc}^{M}(\tau)\; R_{dis}(\tau)$ and a faded self-noise term $R_{cc}^{M}(\tau)\; R_{con}(\tau)$. The faded timing signal is therefore embedded in three types of noise disturbance: the faded self-noise

$R_{cc}^{M}(\tau)\, R_{con}(\tau)$, the s×n terms and finally the n×n term. With this, the PSD of $y(t)$ is simply given by

$$S_{yy}(f) = \mathcal{F}\big[R_{yy}(\tau)\big] = M!\Big({}^{M}S_{cc}(f) \star S_{dis}(f)\Big) + S_{\lambda\lambda}(f), \tag{3.2.19}$$

where

$$S_{\lambda\lambda}(f) = M!\Big({}^{M}S_{cc}(f) \star S_{con}(\tau)\Big) + \sum_{\eta=0}^{M-1}\Big(\frac{M}{\eta}\Big)^2 \eta!\,(M-\eta)!\,\Big[{}^{\eta}S_{cc}(f) \star {}_{\eta}S_{uu}(f) \star {}^{(M-\eta)}S_{nn}(f)\Big] \tag{3.2.20}$$

and

$${}^{\eta}S(f) = \mathcal{F}\big[R^{\eta}(\tau)\big] = S(f) \overset{\eta-1}{\star} S(f), \tag{3.2.21}$$

with $\overset{\eta-1}{\star}$ denotes the $\eta-1$ fold convolution of $S(f)$, and ${}_{\eta}S_{uu}(f)$ is the Fourier transform of ${}_{\eta}R_{uu}(\tau)$. The first term of (3.2.19) has been computed for a few CPM schemes to show the shape of the faded timing signal PSD. For this purpose, two Doppler spectra or fading spectral shapes were used as shown in Fig. 3.2. The land-mobile spectrum is an approximation of the mobile radio fading spectrum amplitude modulated by a Gaussian process [40]. The aeronautical Doppler spectrum[8] [41] is simply given by the Gaussian shape with variance $B_d^2/2$. Figures 3.3 throught 3.5 illustrate the spectrum of the faded timing signal for the CPM schemes discussed in Chapter 2, e.g., 3N3CR α=0.5, M=2, 4, 8 and equally distributed data. Note that the spreading and the amplitude of the spectrum increase as M increases while the general spectrum shape approaches one of a Gaussian shape for large M.

3.2.2 Filtered Faded Timing Signal

The next step in the synchronizer analysis involves a multiband filtering operation as shown in Fig. 3.1b. The ultimate purpose of this filter is to remove as much as possible the disturbance power $S_{\lambda\lambda}(f)$ without cutting off the faded tones signal. At the same time, the filter also acts as a periodic envelope builder for the block processing that follows, i.e., the squared envelope detector. By eliminating part of the disturbance process $\lambda(t)$, it emphasizes the amplitude and phase modulated tones in $u^{M}(t,\underline{a})$. It is therefore likely that the squared envelope detector will recover a relatively strong

[8] The aeronautical channel is only a FFF channel for low signal bandwidths (i.e., less than a few KHz).

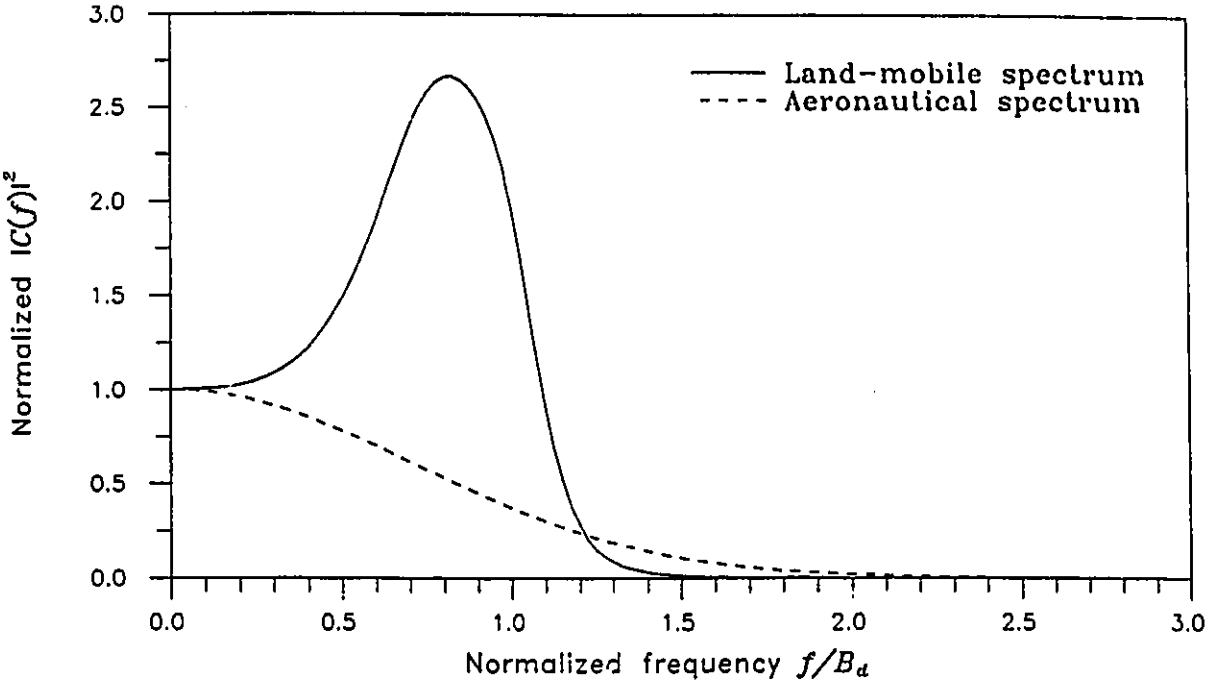

Fig. 3.2. Fading spectrums.

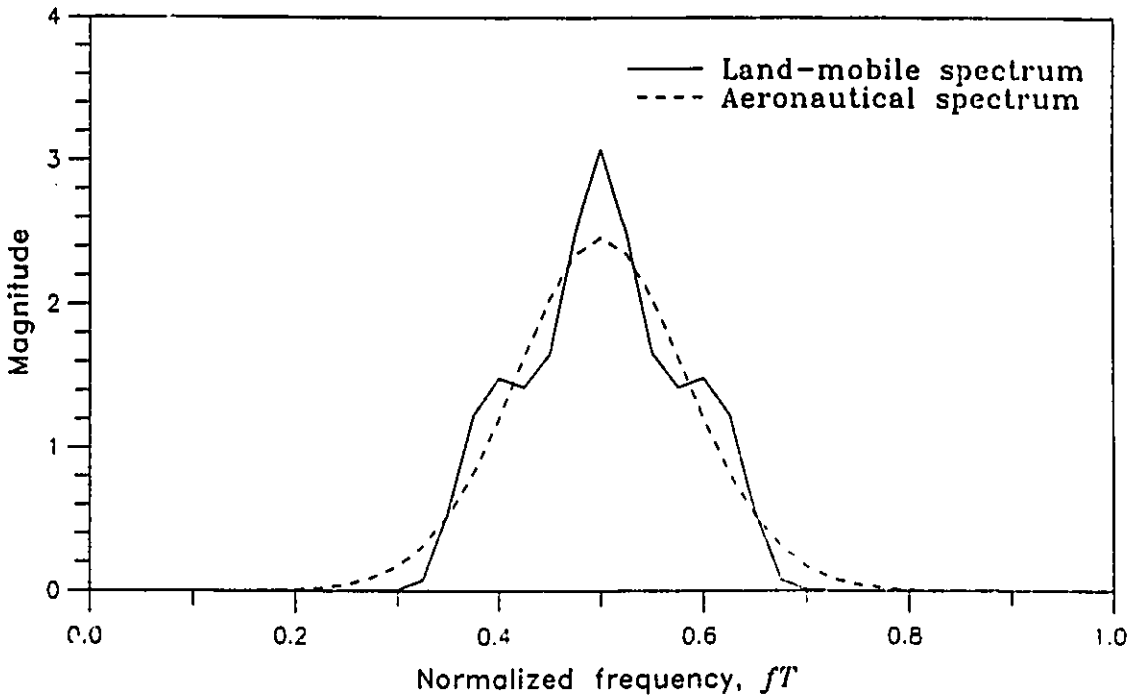

Fig. 3.3. Faded timing signal PSD for binary 3N3CR with B_dT=0.1.

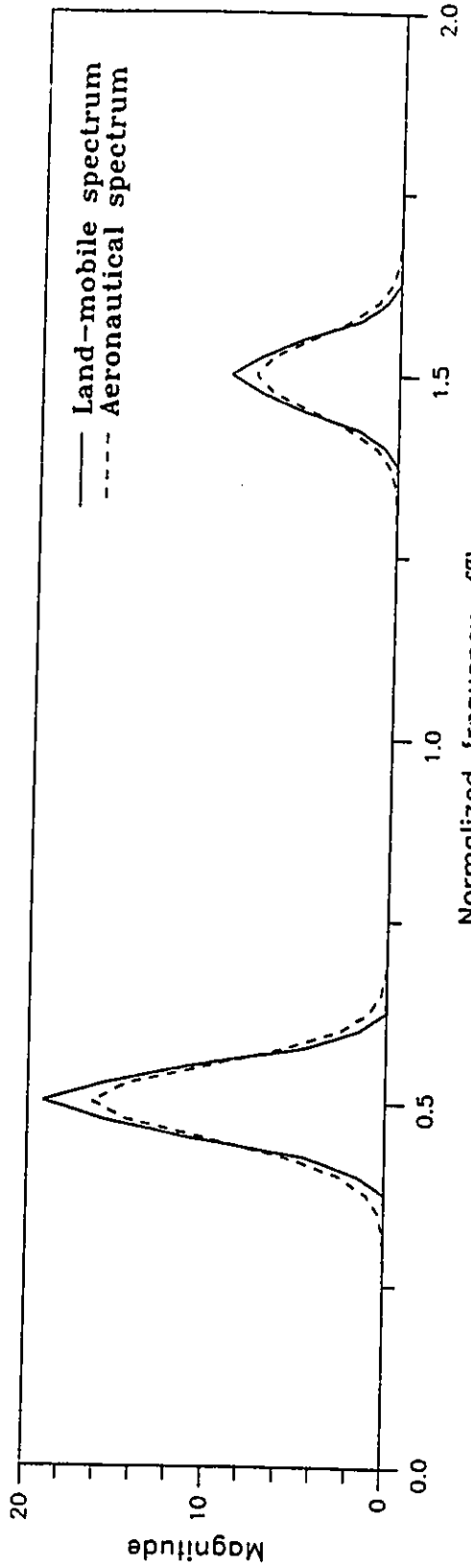

Fig. 3.4. Faded timing signal PSD for quaternary 3N3CR with B_dT=0.05.

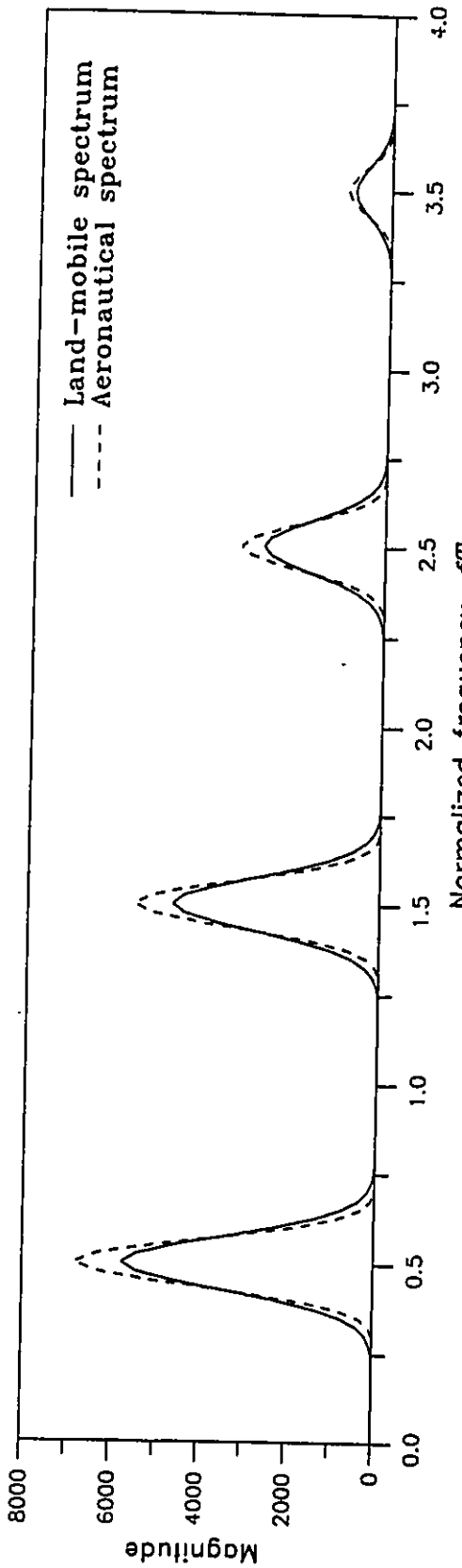

Fig. 3.5. Faded timing signal PSD for 8-ary 3N3CR with B_dT=0.05.

amplitude modulated signal with carrier frequency related to $1/T$. To achieve this goal, a real linear-phase multibandpass filter with the bandpass region centered at odd multiple of $1/2T$, is employed. The linear phase requirement ensures a constant faded tone delay in each bandpass region of $\Psi(f)$. This is a desirable property as will be demonstrate in the next section. The shape of the bandpass region can be chosen in several different ways, and for simplicity we will assume a rectangular shape for the amplitude response[9]. Next consider the bandwidth of this filter. The bandwidth depends basically on three factors. The first one is obviously the fading bandwidth B_d of $C(f)$. As was seen, the faded tones PSD expression contains the term ${}^{M}S_{cc}(f)$ which obviously widen as B_d increase. The second factor is the number of possible data symbols, i.e., M. ${}^{M}S_{cc}(f)$ is the $(M-1)$ fold convolution of $S_{cc}(f)$, and thus has bandwidth of approximately MB_d. This limits the amount of fading the synchronizer can correct for a symbol set because we must meet the constraint $MB_d<1$ to ensure proper operation. The third factor and last factor to consider is the shape of $S_{cc}(f)$ itself. Given those factors and assuming that the tone interference is negligible, the bandwidth B_ψ is defined as being the bandpass region bandwidth of $\Psi(f)$ which leave negligible distortion to one of the M faded tones in ${}^{M}S_{cc}(f) \star S_{dis}(f)$. The range of the normalized product $B_\psi T$ is then $0<B_\psi T<1$. It appears that this spectral spreading of the faded timing signal is the limiting phenomena in the synchronizer chain. If one or a combination of the mentioned factors causes the faded tones to overlap significantly or to require a multi-bandpass filter having passband widths larger than stopband widths, then it is unlikely that the synchronizer will exhibit good performance.

The PSD of the signal at the filter output $x(t)$ can be expressed as

$$S_{xx}(f) = M!\left({}^{M}S_{cc}(f) \star \sum_{\substack{i=-(M-1) \\ i \text{ odd}}}^{M-1} |d_i|^2 \, \delta(f-\tfrac{i}{2T}) \right) + S_{\lambda\lambda}(f) \, |\Psi(f)|^2. \qquad (3.2.22)$$

[9] Two other logical choices for $\psi(f)$ would be a filter matched to ${}^{M}S_{cc}(f)$ and a Wiener filter. The filter matched to ${}^{M}S_{cc}(f)$ shape would attenuates the timing signal and $\lambda(t)$ depending on the frequency shift to hopefully achieve a good average timing signal to noise ratio. The Wiener filter minimizes the difference between a desired response, first term in (3.2.10), and the actual filter output $x(t)$ using the minimum mean squared error criterion. This ensures the best or optimum linear filter in the minimum mean-square sense. The reason why those options are not considered now is because they complicate the analysis, and do not guarantee the performance in the specified sense at the synchronizer output (due to the squared envelope detector).

To get a feeling for the relative power of the information signal compared to the disturbance terms, the faded tone to noise ratio can be computed for each faded tone of Figs. 3.3., 3.4, and 3.5 as a function of $\frac{\sigma_c^2 E_b}{N_0}$. The faded tone to noise ratio would be an increasing function with saturation occurring at high $\frac{\sigma_c^2 E_b}{N_0}$. Depending on $B_\Psi T$, the saturation value of the faded tone to noise ratio would be given by Figs. 2.16, 2.17, and 2.18 for the given schemes. One can see that negative faded tone to noise ratio are possible for M=4 and 8. This may limits furthermore the amount of fading correctable by the synchronizer, and this due to self-noise only.

3.3 Timing Extraction

3.3.1 Tone Recombination Concept

In Chapter 2 it was seen that the expected value ${}_M m_u(t)$ of a CPM signal with integer modulation index is periodic with period T or $2T$. Such a signal can thus be express in terms of a Fourier series expansion. Limiting the number of Fourier series coefficients to M, for reasons explained in the Chapter 2 and in the previous section, it is assumed that this signal is multiplied by a random phase phasor with relatively slow phase variations $\theta(t)$. Let us express the sum of these components as

$$x'(t) = \sum_{\substack{k=-(M-1) \\ k \text{ odd}}}^{M-1} d_k \, e^{j(2\pi f_k t + \theta(t))}, \qquad f_k = \frac{k}{2T}, \tag{3.3.1}$$

where $d_k = |d_k| \, e^{j\varphi_k}$ are the complex Fourier series coefficients. Applying $x'(t)$ with a fixed, but unknown, delay from the origin to a squared envelope detector, yields

$$x'(t+\tau)\, x'^*(t+\tau) = \sum_{\substack{k=-(M-1) \\ k \text{ odd}}}^{M-1} \sum_{\substack{m=-(M-1) \\ m \text{ odd}}}^{M-1} d_k \, d_m^* \, e^{j(2\pi f_k(t+\tau)+\theta(t+\tau))} \, e^{-j(2\pi f_m(t+\tau)+\theta(t+\tau))}$$

$$= \sum_{\substack{k=-(M-1) \\ k \text{ odd}}}^{M-1} \sum_{\substack{m=-(M-1) \\ m \text{ odd}}}^{M-1} |d_k| \, |d_m| \; e^{j2\pi(f_k - f_m)t} \, e^{j2\pi(f_k - f_m)\tau} \, e^{j(\varphi_k - \varphi_m)}$$

$$= \sum_{\substack{l=0 \\ l \text{ even}}}^{2(M-1)} \sum_{\substack{k=-(M-1) \\ k \text{ odd}}}^{M-l-1} 2D_{lk} \cos(2\pi f_l t + 2[illegible] \bar{\varphi}_{lk}), \tag{3.3.2}$$

with $f_l = f_{k+l} - f_k = \frac{l}{2T}$, $\bar{\varphi}_{lk} = \varphi_{k+l} - \varphi_k$ and $D_{lk} = |d_{k+l}|\,|d_k|$. Concentrating on the symbol rate tone, (i.e., $f_{k+l} - f_k$ difference of $1/T$), it is seen that there are $(M-1)$ tones adding at $1/T$. These tones have phases depending on the phase difference $\bar{\varphi}_{2k}$, and on the fixed delay τ. The $(M-1)$ tones at $1/T$ all have a phase shift of $\frac{2\pi\tau}{T}$. Therefore the phase difference between $1/T$ tones does not depend on the fixed delay τ. This means that the phase shift cause by a linear phase filter will not affect the tone recombination. The fixed delay τ was introduced previously to point out that linear phase (i.e., constant delay) is a system design requirement for $\Psi(f)$. The tone's phase due to the difference $\bar{\varphi}_{2k}$ are however not necessarily equal between all $1/T$ tones (i.e., different values of k). To enhance the synchronization possibilities, it is desirable that the phase relationship among the Fourier coefficients d_k be such that the sum of the $(M-1)$ tones at $1/T$ occurs constructively without mutual offset phases. This situation will be verified shortly. For the moment, looking again at (3.3.2) and assuming that a constructive signal summation occurs, then the total amplitude D_{2k} of the $1/T$ tone is then given by

$$D_{2k} = \sum_{\substack{k=-(M-1) \\ k \text{ odd}}}^{M-3} |d_{k+l}|\,|d_{k+2}|. \tag{3.3.3}$$

In the binary case, the maximum value of (3.3.3) occurs when the data symbols are equally likely. This contrasts with the results of Chapter 2 where the power in the discrete components increases when the symbols PDF was not uniform. For the M-ary case, (3.3.3) increases when the $|d_k|$ at $k = \pm(M-1)$ have relatively decreasing weight in $x'(t)$ Fourier series expansion.

3.3.2 Phase Relationship

The phase of the complex Fourier series coefficients can affect the performance of the synchronizer as was seen in the preceding section. It is necessary to enhance the synchronizer performance to find the phase behavior of the d_k for the particular case of a CPM signal with

symmetric pulse shaping. In §2.3.4 it was mentioned that

$$ {}_{M}m_u(-t) = \begin{cases} {}_{M}m_u(T-t), & h \text{ even;} \\ -{}_{M}m_u(T-t), & h \text{ odd,} \end{cases} \qquad 0 \le t \le T, \tag{3.3.4} $$

and the expression for ${}_{M}m_u(t)$ is known (3.2.7). Looking first at the h odd case with an expansion of (3.3.4), we get

$$ {}_{M}m_u(-t) = -\prod_{i=1-L}^{0} \sum_{\substack{k=-(M-1) \\ k \text{ odd}}}^{M-1} P_k \, e^{j2\pi hkq(-t+(1-i)T)}. \tag{3.3.5} $$

For a symmetric pulse shape one can see that

$$ q(t-iT) = \tfrac{1}{2} - q(-t + (L+i)T), \tag{3.3.6} $$

and using the change of variable $t=-x+T$ we get

$$ q(-x+T-iT) = \tfrac{1}{2} - q(x-T + (L+i)T). \tag{3.3.7} $$

Substituting (3.3.7) in (3.3.5) results in

$$ {}_{M}m_u(-t) = -\prod_{i=1-L}^{0} \sum_{\substack{k=-(M-1) \\ k \text{ odd}}}^{M-1} P_k \, e^{j\pi hk} \, e^{-j2\pi hkq(t+(L+i-1)T)}. \tag{3.3.8} $$

For h odd, $e^{j\pi hk}=-1$, and letting $n=-(i+L-1)$,

$$ {}_{M}m_u(-t) = (-1)^{L+1} \prod_{n=1-L}^{0} \sum_{\substack{k=-(M-1) \\ k \text{ odd}}}^{M-1} P_k \, e^{-j2\pi hkq(t-nT)} = (-1)^{L+1} \, {}_{M}m_u^*(t). \tag{3.3.9} $$

Following a similar procedure for h even,

$$ {}_{M}m_u(-t) = \begin{cases} {}_{M}m_u^*(t), & h \text{ even;} \\ (-1)^{L+1} \, {}_{M}m_u^*(t), & h \text{ odd,} \end{cases} \qquad 0 \le t \le T. \tag{3.3.10} $$

This result indicates that for h even, and (h odd, L odd), the d_k are purely real while for (h odd, L even), the d_k are purely imaginary. Another point to note is that the result is independent of the symbol probability density function.

These results do not prove that the arguments of the coefficients are all the same sign, since a 180° uncertainty in the arguments remains. However in the examples considered which involve pulses satisfying the Nyquist III criterion [21], the signs of the d_k have been found to be the same and it is conjectured that this result holds for all such pulses. It follows therefore that $\bar{\varphi}_{2k}=0$ (due to the signal phase) so that the resulting generated tone has zero phase. This assumes that the phase response of the multiband filter is zero, but providing the phase response is linear, the reconstructed tone will remain phase aligned. For Nyquist III pulse shaping, the $|d_k|$ for $k=\pm 1, \pm 3, \ldots, \pm(M-1)$ yield large values relatively independent of L (see Chapter 2) making it a desirable class of pulse shape from the synchronization point of view. Several examples of the values of d_k for unit modulation index quaternary CPM with LREC and N3CR $\alpha=0.5$ pulse shaping are shown in Table 6 and 7, and the two particular cases of 2REC and 3N3CR is illustrated in Fig. 3.6. One can see that the d_k are in complex conjugate pairs and that the real tones are all of the same sign even for non-Nyquist III pulse shapes. This seems to be a general behavior for all CPM schemes meeting (3.3.10) condition with h odd. Consider for example 2REC $h=1$. Taking the differences $\bar{\varphi}_{2k}$ yields three tones with phase 0, π and 0 radians. Obviously, destructive interference between the tones is occuring. On the other hand, N3CR $\alpha=0.5$ gives three tones with 0 radian phase, thus resulting in constructive tones.

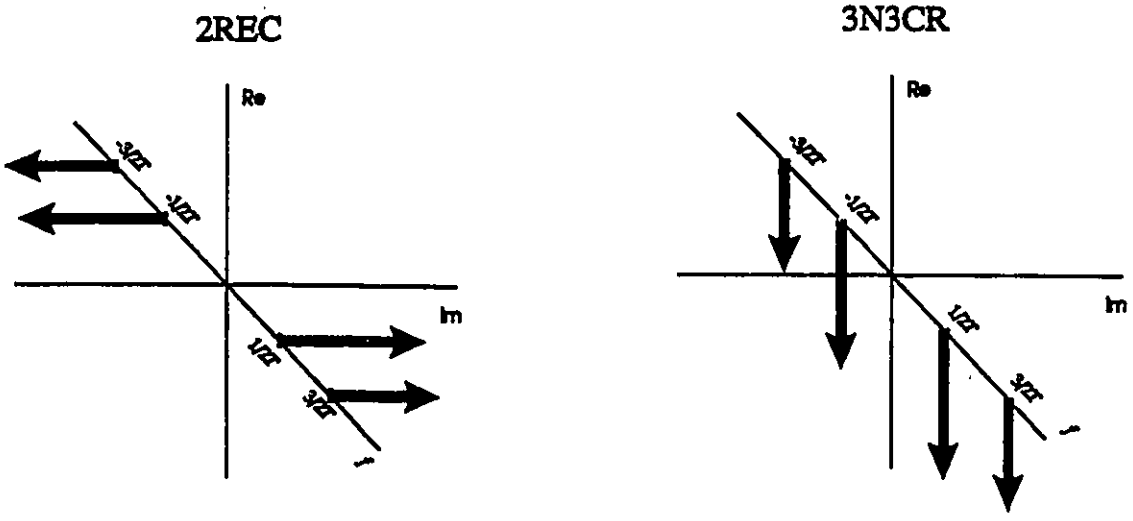

Fig. 3.6. Phase values of the d_k for quaternary 2REC and 3N3CR α=0.5.

Table 6. Complex Fourier series coefficients for quaternary LREC and h=1.

	n	$\lvert\cdot\rvert$	$\angle\cdot$ in rad
$L=1$	−3	0.25	0
	−1	0.25	0
	+1	0.25	0
	+3	0.25	0
$L=2$	−3	0.0625	$\pi/2$
	−1	0.0625	$\pi/2$
	+1	0.0625	$-\pi/2$
	+3	0.0625	$-\pi/2$
$L=3$	−3	0.0156	π
	−1	0.0156	π
	+1	0.0156	π
	+3	0.0156	π
$L=4$	−3	3.9×10^{-3}	$-\pi/2$
	−1	1.17×10^{-2}	$\pi/2$
	+1	1.17×10^{-2}	$-\pi/2$
	+3	3.9×10^{-3}	$\pi/2$

Table 7. Complex Fourier series coefficients for quaternary 3N3CR and h=1.

	n	$\lvert\cdot\rvert$	$\angle\cdot$ in rad
$L=1$	−3	0.23	0
	−1	0.316	0
	+1	0.316	0
	+3	0.23	0
$L=3$	−3	0.21	π
	−1	0.296	π
	+1	0.296	π
	+3	0.21	π
$L=5$	−3	0.207	0
	−1	0.295	0
	+1	0.295	0
	+3	0.207	0

3.3.3 Squared Envelope Detector Analysis

First it will be shown that $\xi(t)$, the squared envelope detector output has periodic components at multiples of the symbol rate. Next, the characteristics of the disturbance process, affecting the periodic component of interest, will be determined.

From equation (3.2.10), $x(t)$ is redefined as

$$x(t) = b(t) + \gamma(t) \tag{3.3.11}$$

with

$$b(t) = |c(t)|^M \, e^{jM\theta(t)} \sum_{\substack{k=-(M-1) \\ k \text{ odd}}}^{M-1} d_k \, e^{j2\pi f_k t}, \qquad f_k = \frac{k}{2T}, \tag{3.3.12}$$

$$\simeq \; c^M(t) \; {}_M m_u(t),$$

and

$$\gamma(t) = \lambda(t) \star \psi(t) = |\gamma(t)| \, e^{j\nu(t)}. \tag{3.3.13}$$

Here, only the M strongest tones of ${}_M m_u(t)$ resulting from multiband filtering are kept and the complex Fourier series expansion is used to represent there sum. Also, the process $\lambda(t)$ is introduced, which regroups the disturbance processes of $y(t)$, with $\psi(t)$ the impulse response of unit gain filter $\Psi(f)$. The phase of $\psi(t)$ will simply delay $x(t)$ and can therefore be dropped since it does not affect the result at the squared envelope detector output. This fixed delay can be accounted for at the system output. Finally, recall from §3.2 that $b(t)$ and $\lambda(t)$ are independent [$\Delta u^M(t,\underline{a})$ is independent of ${}_M m_u(t)$] zero mean processes.

The signal at the squared envelope detector output $\xi(t)$, can be express as

$$\xi(t) = |x(t)|^2$$

$$= |b(t)|^2 + 2\Re\left[b(t)\,\gamma(t)^*\right] + |\gamma(t)|^2$$

$$= |c(t)|^{2M} \sum_{\substack{l=0 \\ l \text{ even}}}^{2(M-1)} \sum_{\substack{k=-(M-1) \\ k \text{ odd}}}^{M-l-1} 2D_{lk} \cos(2\pi f_l t + \bar{\varphi}_{lk})$$

$$+ 2\Re\left[c^M(t) \sum_{\substack{k=-(M-1) \\ k \text{ odd}}}^{M-1} d_k \, e^{j2\pi f_k t} \gamma(t)^* \right] + |\gamma(t)|^2. \qquad (3.3.14)$$

Like the preceeding analysis, consider the first moment of $\xi(t)$, and by using the result of §3.3.1 it can be shown that

$$\mathbf{E}\left\{\xi(t)\right\} = \mathbf{E}\left\{|b(t)|^2\right\} + \mathbf{E}\left\{|\gamma(t)|^2\right\}, \qquad (3.3.15)$$

with

$$\mathbf{E}\left\{|b(t)|^2\right\} = \mathbf{E}\left\{|c(t)|^{2M}\right\} \sum_{\substack{l=0 \\ l \text{ even}}}^{2(M-1)} \sum_{\substack{k=-(M-1) \\ k \text{ odd}}}^{M-l-1} 2D_{lk} \cos(2\pi f_l t + \bar{\varphi}_{lk}) \qquad (3.3.16)$$

$$\simeq \mathbf{E}\left\{|c(t)|^{2M}\right\} R_{dis}(t,t),$$

$$\mathbf{E}\left\{|\gamma(t)|^2\right\} = R_{\gamma\gamma}(t,t) = R_{\lambda\lambda}(t,t) \star \psi(-t) \star \psi(t). \qquad (3.3.17)$$

Expression (3.3.14) explicitly shows that we recover a sum of periodic signals, amplitude modulated by a Rayleigh random process raised to the power $2M$. The fact that the expected value of $|b(t)|^2$ is also almost equal to the product of $\mathbf{E}\left\{|c(t)|^{2M}\right\}$ and $R_{dis}(t,t)$ makes it apparent that we are able to recover symbol timing due to the cyclostationary character of $u(t,\underline{a})$. The phase fluctuations that were experienced before the squared envelope detector are now completely removed from the timing information signal. Note that (3.3.16) can be evaluated exactly since all the functions constituting it are known.

Although an appropriate timing signal can be extracted, it is necessary to determine the effects of the disturbance process generated by $\gamma(t)$ at the squared envelope detector output and particularly,

its relative amplitude compare to the timing signal. One approach is to derive the autocorrelation function of $\xi(t)$ which can be used to compute the PSD $S_{\xi\xi}(f)$. It is known however that in many cases this approach leads to pessimistic results regarding the evaluation of the timing jitter [38][42]. However in the situation here, the problem corresponds to a random phase fluctuation in the received signal so that the PSD may represent a good estimate of the noise power. The exact evaluation of $S_{\xi\xi}(f)$ using the autocovariance function $C_{\xi\xi}(\tau)$ is not easy. It is shown in Appendix D that

$$C_{\xi\xi}(\tau) = C_{|b|^2|b|^2}(\tau) + 2\Re\left[R_{bb}(\tau)\, R_{\gamma\gamma}(\tau)^*\right] + C_{|\gamma|^2|\gamma|^2}(\tau) \tag{3.3.18}$$

where $C_{\xi\xi}(\tau)$, $C_{|b|^2|b|^2}(\tau)$ and $C_{|\gamma|^2|\gamma|^2}(\tau)$ are the autocovariance function of $\xi(t)$, $|b|^2$ and $|\gamma|^2$ respectively. Unfortunately the term $C_{|\gamma|^2|\gamma|^2}(\tau)$ is very difficult to derive. This is due to the fact that the process $|\gamma|^2$ is very hard to characterize statistically (its probability density function as well as its relationship with $\gamma(t)$ are not well defined). Although $C_{\xi\xi}(f)$ cannot be easily found or approximated, a look at (3.3.16) reveals that the M tones are affected by amplitude modulation that does not create any time jitter at all since $|c(t)|^{2M} \geq 0$ for all t. In some situations (low B_d), this amplitude fluctuation may have a significant contribution to the spectrum around the symbol rate tone and may therefore influence the jitter. This phenomena will be examined.

The above observations tend to indicate that the total spectrum around $1/T$ is not a good parameter to derive an estimate for the timing jitter as encountered in many situations [42]. In addition, the spectrum itself is not trivial to evaluate because of the filtering followed by a nonlinear operation on a nonlinear modulated signal. This represents a major difficulty and the solution of the problem is beyond the scope of this thesis. Consequently the total power spectrum orientation as a mean to deduce timing jitter in a fast flat-fading environment will be dropped.

3.3.3.1 Timing signal envelope fluctuations

The squared envelope detector efficiently removed the random phase fluctuations of the timing signal. However, as was seen the envelope of the random process $c^M(t)$ still effects the timing signal.

This does not create any Doppler effect like that present before the squared envelope detector, but acts like an amplitude modulation signal on the timing tone. The purpose of looking at the envelope characteristics is to establish its effect on the spectrum at the system output.

The process of interest is $\vartheta=|c(t)|^{2M}$, i.e., a Rayleigh random process raised to the power $2M$. Using basic random variable transformation techniques [15][19] and §2.1 definitions it can be shown that the probability density function of ϑ is given by

$$p_\vartheta(\vartheta) = \begin{cases} \dfrac{1}{M\sigma_c^2\,\vartheta^{(1-\frac{1}{M})}}\, e^{-\frac{\vartheta^{(1/M)}}{\sigma_c^2}}, & 0 \le \vartheta \le \infty; \\ 0, & \text{elsewhere,} \end{cases} \tag{3.3.19}$$

with mean

$$m_\vartheta = \sigma_c^{2M}\, M!, \tag{3.3.20}$$

and variance

$$\sigma_\vartheta^2 = \sigma_c^{4M}\left[(2M)! - (M!)^2\right]. \tag{3.3.21}$$

To evaluate the spectrum of ϑ, the autocorrelation function of ϑ can be used. It is shown in [44] that

$$R_{\vartheta\vartheta}(\tau) = \left\langle \mathbf{E}\left\{|c(t+\tau)|^{2M}|c(t)|^{2M}\right\}\right\rangle_t = (M!)^2\, R_{cc}^{2M}(0) \sum_{i=0}^{M} \binom{M}{i}^2 \left(\frac{|R_{cc}(\tau)|}{R_{cc}(0)}\right)^{2i}. \tag{3.3.22}$$

The frequency domain implication of the above expression lies in the presence of a discrete tone (due to non-zero mean) at $f=0$ surrounded by a continuous spectrum. The relative amplitude of the discrete tone compared to the continuous spectrum near $f=0$ is of importance. Note that in the system discussed here, most of the power in the spectrum will be centered around multiples of $1/T$. But for the moment, consider the average PSD of ϑ for a particular fading spectrum. Defining

$$S_{\vartheta\vartheta}(f) = \mathcal{F}\left[R_{\vartheta\vartheta}(\tau)\right], \tag{3.3.23}$$

and using the inverse Fourier transform of the aeronautical Doppler spectrum (as an example) to get

$$R_{cc}(\tau) = e^{-(\pi B_d \tau)^2}, \tag{3.3.24}$$

$S_{\vartheta\vartheta}(f)$ can be computed for M=2, 4, and 8 as a function of the normalized frequency f/B_d to give an idea of the power in presence. Examining Figs. 3.7, 3.8 and 3.9, it is seen that the difference between the continuous spectrum and the discrete component amplitude increases when M increases. This mean that the amplitude variations of the tone at $1/T$ are going to be more important for increasing M.

3.3.4 Timing Tone

The last block of Fig. 3.1b in the signal path is a unity-gain linear-phase narrowband filter centered around $1/T$. It has been shown here that the filter input signal contains a discrete tone at the symbol rate. The purpose of this filter is to reduce the noise power around $1/T$. From Chapter 2, it was shown that the narrowband output signal $\beta(t)$ ($B \ll 1/T$) can be expressed as

$$\beta(t) = \sqrt{2}\left[\beta_I(t)\cos\frac{2\pi t}{T} - \beta_Q(t)\sin\frac{2\pi t}{T}\right], \tag{3.3.25}$$

where $\beta_I(t)=m_\beta+\vartheta'(t)+\beta'_I(t)$, $\beta_Q(t)=\beta'_Q(t)$ with $\vartheta'(t)$ representing the filtered modulated variations of the timing tone around $m_\beta=2m_\vartheta D_2$ due to the signal envelope variations. The terms $\beta'_I(t)$ and $\beta'_Q(t)$ are the inphase and quadrature components of the filtered process associated with the second and third terms of (3.3.14). The derivation of $\beta_I(t)$ and $\beta_Q(t)$ (related to the inphase and quadradure component of $\xi(t)$ for a real NRPF) in terms of the signal and channel characteristics is a very difficult task because we do not know exactly $\xi(t)$. Likewise there respective spectrum has only been found for particular cases [39][42]. It is suspected that for the AWGN channel a very good approximation for $\beta(t)$ would be possible because the unknown terms in (3.3.14) can be approximated, as is often done in narrowband filtering of a single tone. Recall that there are multitones present before the squared envelope detector. However this is not of interest in the present analysis (still it might give some insight to an approximation for the FFF channel in certain conditions).

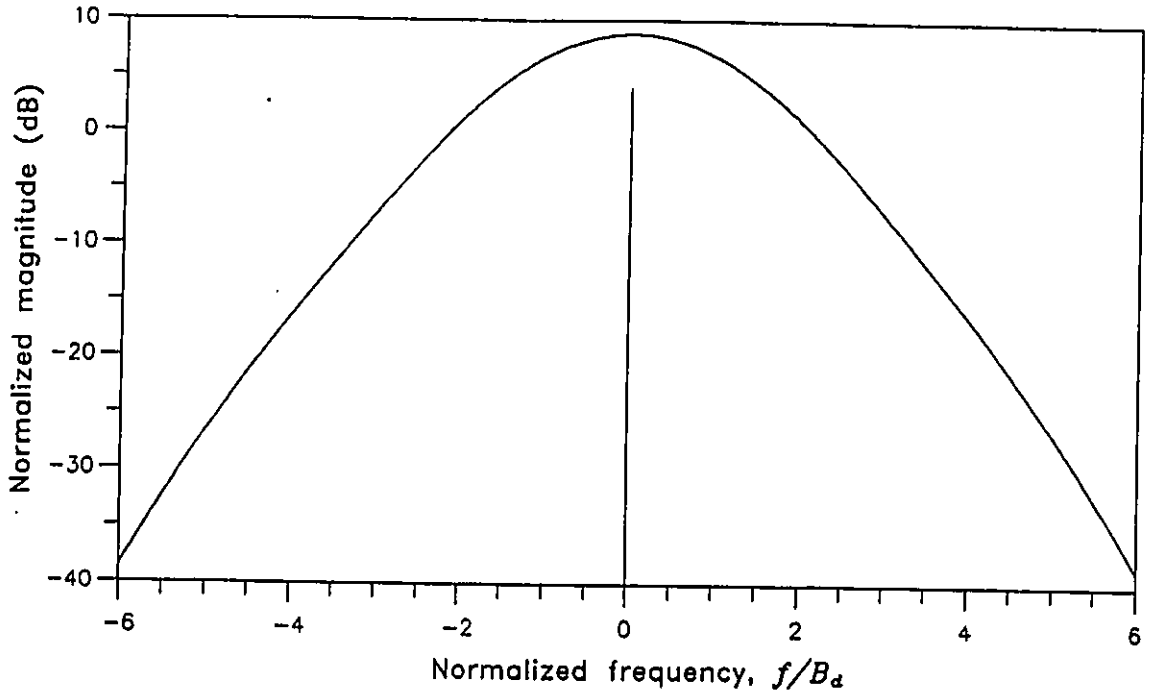

Fig. 3.7. Spectrum of ϑ with aeronautical fading spectrum and M=2.

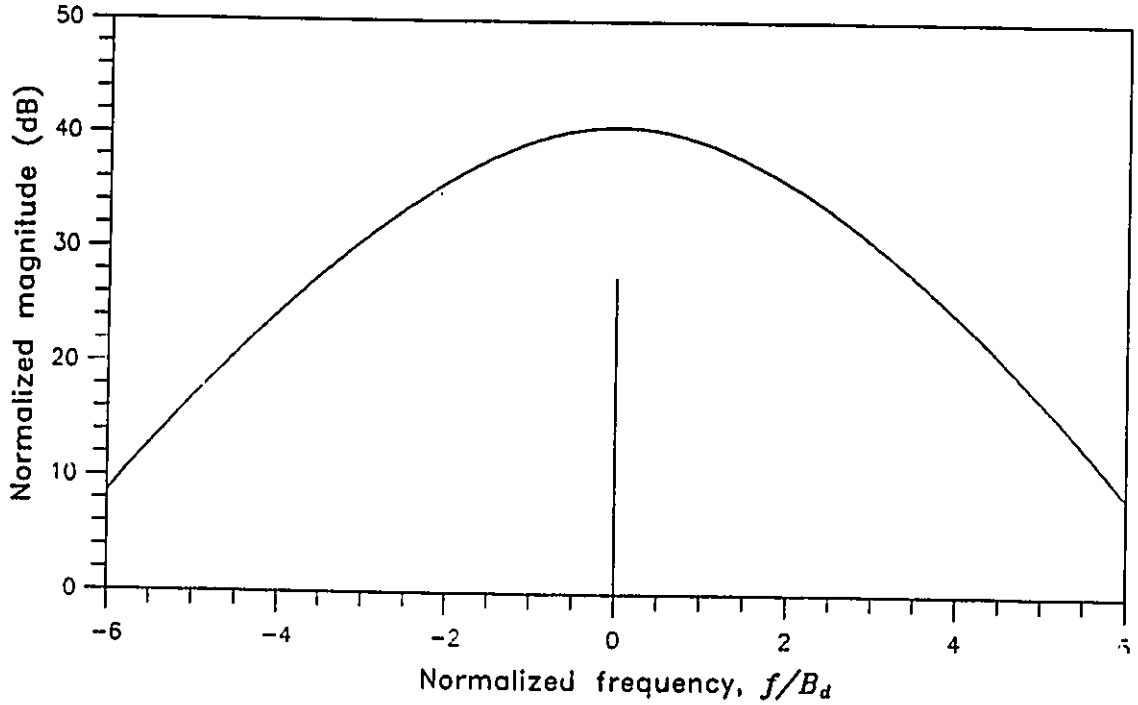

Fig. 3.8. Spectrum of ϑ with aeronautical fading spectrum and M=4.

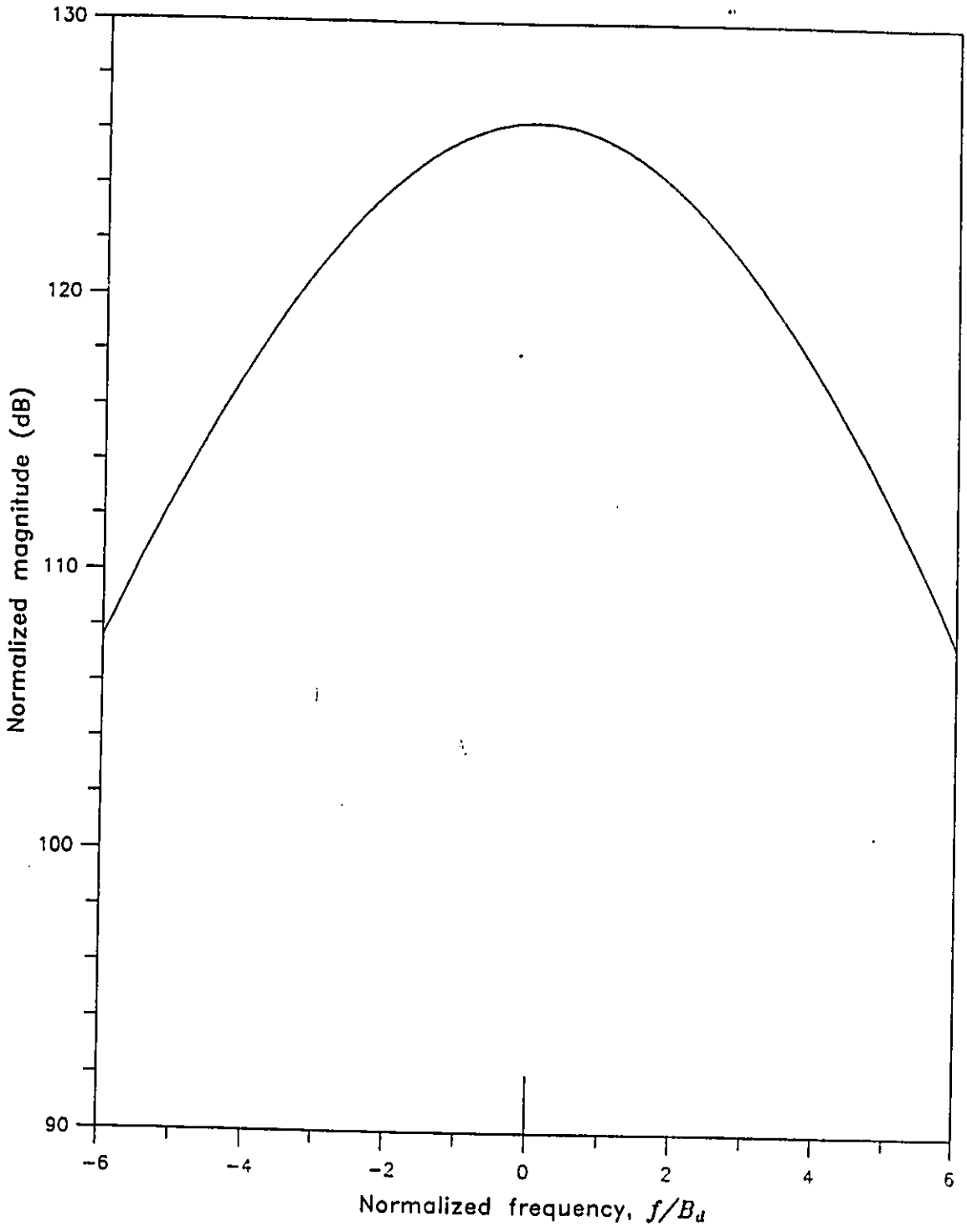

Fig. 3.9. Spectrum of ϑ with aeronautical fading spectrum and M=8.

3.4 Timing Jitter

The timing jitter associated with the zero crossings of a periodic tone can be determined from (3.3.25). For example, if it is assumed that $\beta_Q(t)=0$ and that $\beta_I(t)>0$, then the zero crossings of $\beta(t)$ are jitter free. In the present signal, it can be assumed that $\beta_I(t)>0$, leaving jitter due to $\beta_Q(t)$ only. Explicitly, $\beta(t)$ can be expressed as

$$\beta(t) = \Re\left[|\beta(t)|\, e^{j\left[\frac{2\pi t}{T}+\angle\beta(t)\right]}\right], \tag{3.4.1a}$$

with

$$|\beta(t)| = \sqrt{\beta_I^2(t) + \beta_Q^2(t)}, \tag{3.4.2b}$$

$$\angle\beta(t) = \tan^{-1}\frac{\beta_Q(t)}{\beta_I(t)}. \tag{3.4.3c}$$

We can associate with this phasor, a timing error related to (3.4.3c) by

$$\epsilon(t) = \frac{T}{2\pi}\angle\beta(t). \tag{3.4.4}$$

Figure 3.10 illustrates a typical case for the complex phasor $|\beta(t)|\, e^{j\angle\beta(t)}$ and the corresponding timing jitter. The problem of finding the probability density function of $\epsilon(t)$ is once again difficult because of the $\tan^{-1}$ operation. For proper operation of the synchronizer, $\epsilon(t)$ has to be small, and this condition is meet when $\beta_I(t)\approx m_\beta \gg \beta_Q(t)$ leading to

$$\epsilon(t) \approx \frac{T}{2\pi m_\beta}\beta_Q(t) \quad \text{(in seconds)}. \tag{3.4.5}$$

The above conditions are met for a particular set of NBPF bandwidths and it is up the designer to ensure their realization. Now, it is much easier to find an expression for the first and second central moment of $\epsilon(t)$. The process $\beta_Q(t)$ is zero mean since part of the mean of $\xi(t)$ is included in $\beta_I(t)$ while the rest is filtered by the NBPF, consequently $m_\epsilon=0$ if there is no timing misadjustment. The other important statistical characterization of $\epsilon(t)$ is given by its variance. With the use of the small angle assumption, the variance can be expressed as

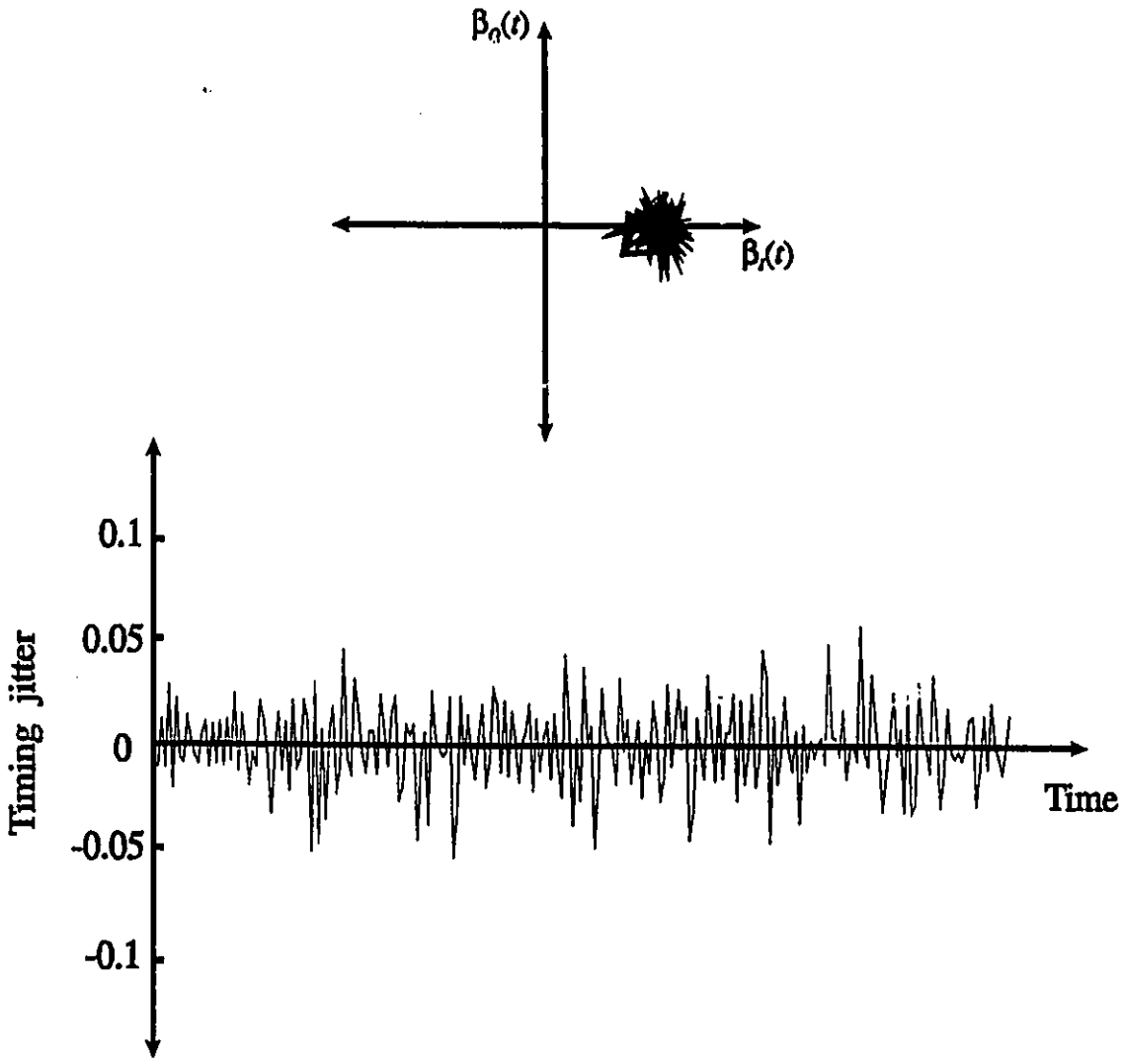

Fig. 3.10. Timing jitter.

$$\sigma_\epsilon^2 = \mathbb{E}\left\{\epsilon^2(t)\right\} \approx \frac{T^2}{(2\pi)^2 m_\beta^2}\,\mathbb{E}\left\{\beta_Q^2(t)\right\} . \tag{3.4.6}$$

This expression is however not analytically tractable for the reasons mentioned earlier, i.e., $\mathbb{E}\left\{\beta_Q^2(t)\right\}$ is not easily tractable. There are probably other measuments that are indicative of the synchronizer performance, but the timing error variance is well understood and somewhat intuitively simple. Since further progress in the present analysis is not possible, the next chapter will look at another way of evaluating σ_ϵ^2, namely computer simulation. ■

Chapter 4

TIMING RECOVERY PERFORMANCE

The analysis in the preceding chapter show just how difficult it is to analytically compute the performance measures such as timing jitter variance. Because of this difficulty, in attempting to numerically evaluate the timing jitter of some representative situations, it was found necessary to resort to computer simulation. The means employed and results obtained are presented in this chapter which concludes with a discussion of some aspects of the practical implementation of this type of synchronizer.

4.1 Simulation

Three general aspects of the simulation approach developed in this thesis can be highlighted. They are the simulation goals, model and method. The simulation goals are diverse and numerous. Among the most important for the present problem, are

1) numerical computation of a timing jitter variance estimate,
2) verification of some analytic assumptions, and
3) insight to pursue analysis.

The objectives are going to be met with the help of a simulation model based on the analytic model with a Rician channel instead of restricting ourselves to a Rayleigh channel. Referring to Fig. 4.1, the set $\{\underline{a}_J\}$ represents a vector of J symbols taken from a set of M possible data values. This vector feeds a discrete-time complex baseband CPM modulator with a given pulse shape and sampling rate $T_s=\frac{T}{2M}$, where T is the symbol period. The signal block length is then of $N=2MJ$ samples. This

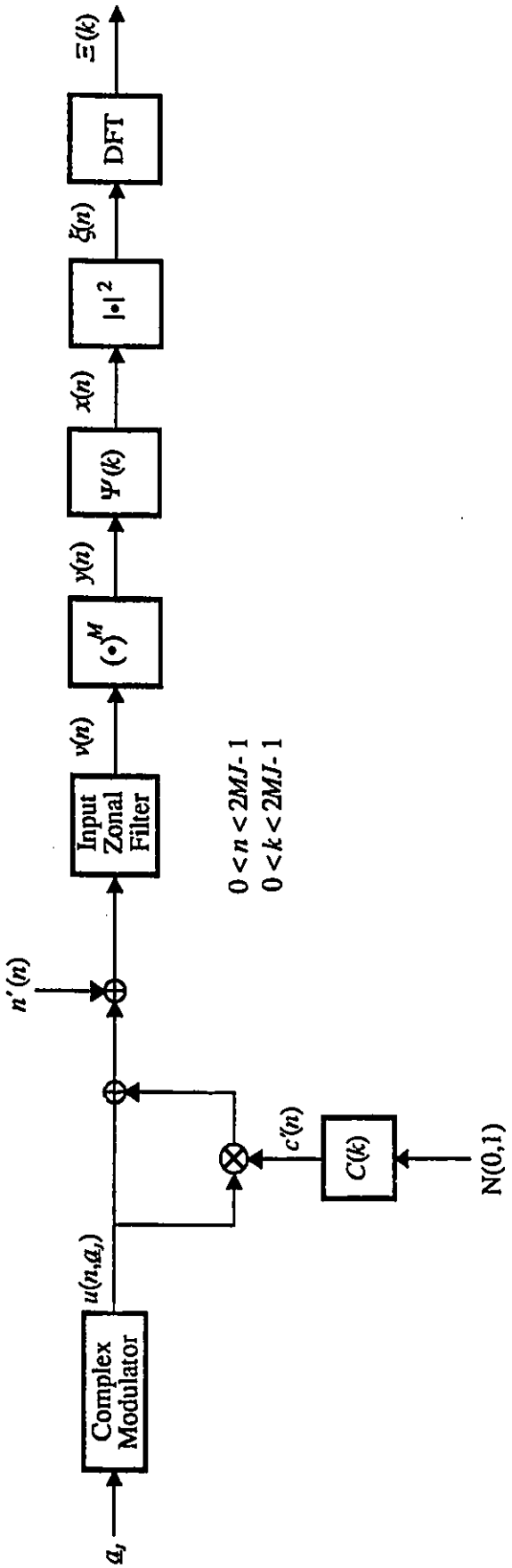

Fig. 4.1. Simulation model.

signal block is sent through a Rician channel where it is multiplied by $c(n) \equiv c(nT_s)$ $0 \leq n \leq N-1$, a discrete-time random Gaussian process with mean m_c (set to one without loss of generality) and variance σ_c^2. The additive noise signal power is determined with respect to the total average received signal power $E\left\{|c(t)|^2\right\} P$ so that fair comparisons can be made for different channel parameters. For notational convenience, the transmitted average signal power $P=\frac{E}{T}$ is set to unity. Then, the signal block is processed according to each element of the synchronizer. All the filters are implemented in the frequency domain using the discrete Fourier transform (DFT). The input filter has a root raised cosine (with 25% excess bandwidth) shape, shown in Fig. 4.2, with a one-sided bandwidth $B_z/2$. The multitone filter has a strong bandlimited shape with each tone bandwidth given by B_ψ. For the AWGN channel, $B_\psi T$ has been fixed to 0.01. Note that the NBPF, is not implemented and therefore we will derive our synchronizer performance from the DFT of $\xi(n) \equiv \xi(nT_s)$.

The data sequence and the Gaussian noise samples are created using a pseudo random number generator employing the linear congruential method. The cycle length of this generator is approximately 2^{32}. Since any simulation run will only use a small portion of this sequence, this generator is adequate for a Monté Carlo block simulation of the system.

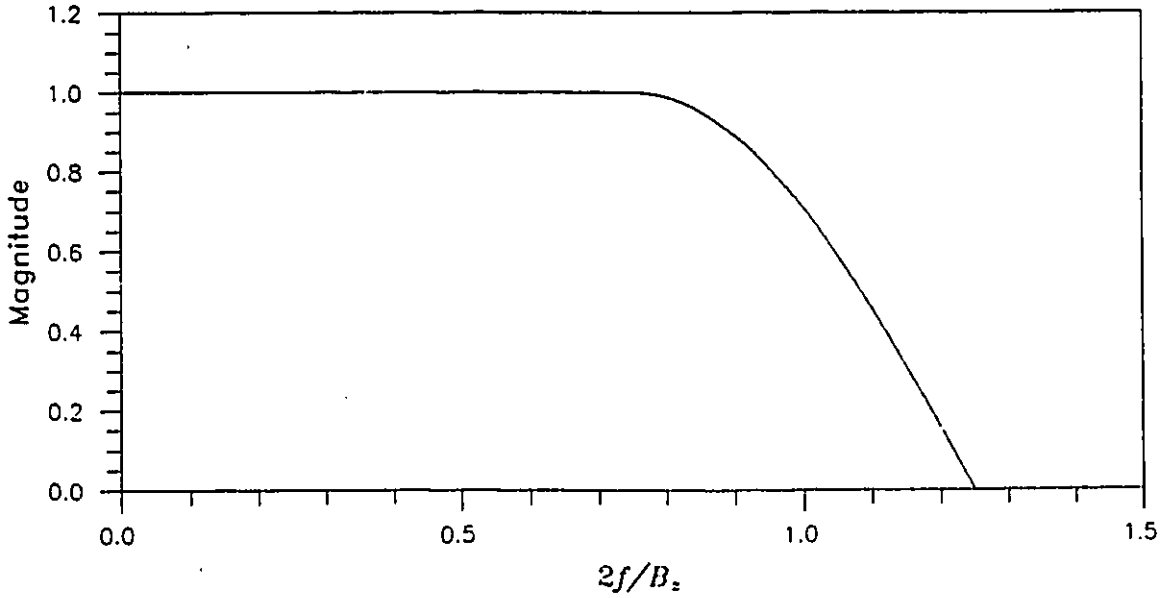

Fig. 4.2. Input filter magnitude response (root raised cosine α=.25).

4.2 RMS[10] Timing Jitter Estimation

4.2.1 Simulation Jitter Definition

A simulation run based on the model described in the previous section leads to a real sequence $\xi(n)$ $0 \leq n \leq N-1$, from which the symbol timing jitter can be evaluated since $\xi(n)$ contains a periodic component at $1/T$. However, the signal of interest is not $\xi(n)$, but $\beta(n)$ the filtered version of $\xi(n)$ around $1/T$. Thus for a narrow band sequence $\beta(n)$, it can be written that

$$\beta(n) = \Re\left\{ e^{j\frac{2\pi nk}{N}} \sum_{i=-N'}^{N'} \Xi(k+i)\, e^{j\frac{2\pi ni}{N}} \right\}, \qquad N' \ll N \text{ and } k=(M+1)J, \tag{4.2.1}$$

where $\Xi(k+i)$ are the centered DFT coefficients of $\xi(n)$ around $1/T$. Now the complex baseband equivalent of $\beta(n)$, defined as $\tilde{\beta}(n)$ can be express in terms of the $\Xi(k+i)$ as

$$\tilde{\beta}(n) = \sqrt{2}\left[\beta_I(n) + j\beta_Q(n)\right] = \sqrt{2} \sum_{i=-N'}^{N'} \Xi(k+i)\, e^{j\frac{2\pi ni}{N}}, \tag{4.2.2}$$

with

$$\beta_I = \text{IDFT}\left\{\Xi_{even}(k+i)\right\}, \qquad i=-N', \ldots, N', \tag{4.2.3a}$$

$$\beta_Q = \text{IDFT}\left\{\Xi_{odd}(k+i)\right\}, \qquad i=-N', \ldots, N', \tag{4.2.3b}$$

where IDFT denotes Inverse DFT. $\Xi_{even}(k+i)$ and $\Xi_{odd}(k+i)$ are defined [46] as

$$\Xi_{even}(k+i) = \tfrac{1}{2}\left[\Xi(k+i) + \Xi^*(k+i)\right], \qquad i=-N', \ldots, N', \tag{4.2.4a}$$

$$\Xi_{odd}(k+i) = \tfrac{1}{2}\left[\Xi(k+i) - \Xi^*(k+i)\right], \qquad i=-N', \ldots, N'. \tag{4.2.4b}$$

Equation (4.2.2) is in a form similar to (3.4.2) and it is easy to define an estimate of σ_ϵ^2 for a given block l, named $\hat{\sigma}_{\epsilon l}^2$ as

$$\hat{\sigma}_{\epsilon l}^2 = \frac{T^2}{(2\pi)^2}\, \text{E}\left\{\frac{\beta_Q^2(n)}{\beta_I^2(n)}\right\} \simeq \frac{T^2}{(2\pi)^2}\, \frac{T_s}{N} \sum_{n=1}^{N} \frac{\beta_Q^2(n)}{\beta_I^2(n)}. \tag{4.2.5}$$

[10] In the present context, root mean square (RMS) is equivalent to standard deviation in statistical theory.

The major difference between this expression and (3.4.6) is that in our simulation we do not have m_β^2 but $\beta_I^2(n)$. The difference is insignificant if $m_\beta \gg \vartheta'(t)+\beta_I'(t)$ which is true for modulation schemes that can have their timing tracked by the present synchronizer. In terms of the DFT and the preceding assumption, it can be found using Farseval's relation for the DFT that (4.2.5) is equivalent to

$$\hat{\sigma}_{\epsilon l}^2 \simeq \frac{T^2}{(2\pi)^2}\frac{\frac{T}{2MN^2}\sum_{i=-N'}^{N'}|\Xi_{odd}(k+i)|^2}{\left(\frac{|\Xi_{even}(k)|^2-|\Xi_{even}(k+1)|^2}{N^2}\right)}. \tag{4.2.6}$$

Now it turns out, after many observations, that $\Xi_{odd}(k+i)$ and $\Xi_{even}(k+i)$ $i=-N', \ldots, N'$ are approximatly constant if $\frac{(2N'+1)}{J} \leq B_\psi T$. Fig. 4.3 illustrates typical shape of $\Xi_{odd}(k+i)$ and $\Xi_{even}(k+i)$ for the AWGN channel and the FFF channel. In both cases, the above observation holds. Thus, equation (4.2.6) can be rewritten as

$$\hat{\sigma}_{\epsilon l}^2 = \frac{T^2}{(2\pi)^2}\frac{\frac{BT}{2MN}|\Xi_{odd}(k)|^2}{\left(\frac{|\Xi_{even}(k)|^2-|\Xi_{even}(k+1)|^2}{N^2}\right)} \tag{4.2.7}$$

with $B \leq B_\psi$ and $B \ll 1/T$. Expressed in this way, B represents the bandwidth of the narrow bandpass filter centered around $1/T$. For a typical application, the restriction on the bandwidth B is naturally satisfied and in the case where it is not, equation (4.2.7) can be viewed as an upper bound on the jitter variance because of the narrowband shape of $\Xi_{even}(k)$ for practical B (see Fig. 4.3). Finally, the results will be expressed in terms of a normalized RMS timing jitter defined as

$$\hat{\sigma}_{\epsilon l} = \frac{T}{2\pi}\sqrt{\frac{J|\Xi_{odd}(k)|^2}{|\Xi_{even}(k)|^2-|\Xi_{even}(k+1)|^2}} \qquad \text{(in second}/\sqrt{BT}\text{)}. \tag{4.2.8}$$

As the last expression indicates, $\hat{\sigma}_{\epsilon l}$ is an estimate of σ_ϵ. The nature of the simulation leaves us with variations in the $\Xi(k+i)$ from one simulation block to another. To improve the quality of the estimate, an average of $\hat{\sigma}_{\epsilon l}$ over several blocks is performed to get a reasonable confidence interval for the results. Explicitly, to determine $\hat{\sigma}_\epsilon$ at a given E_b/N_0, 30 estimates $\hat{\sigma}_{\epsilon l}$ $1 \leq l \leq 30$ is generated and $\hat{\sigma}_\epsilon$

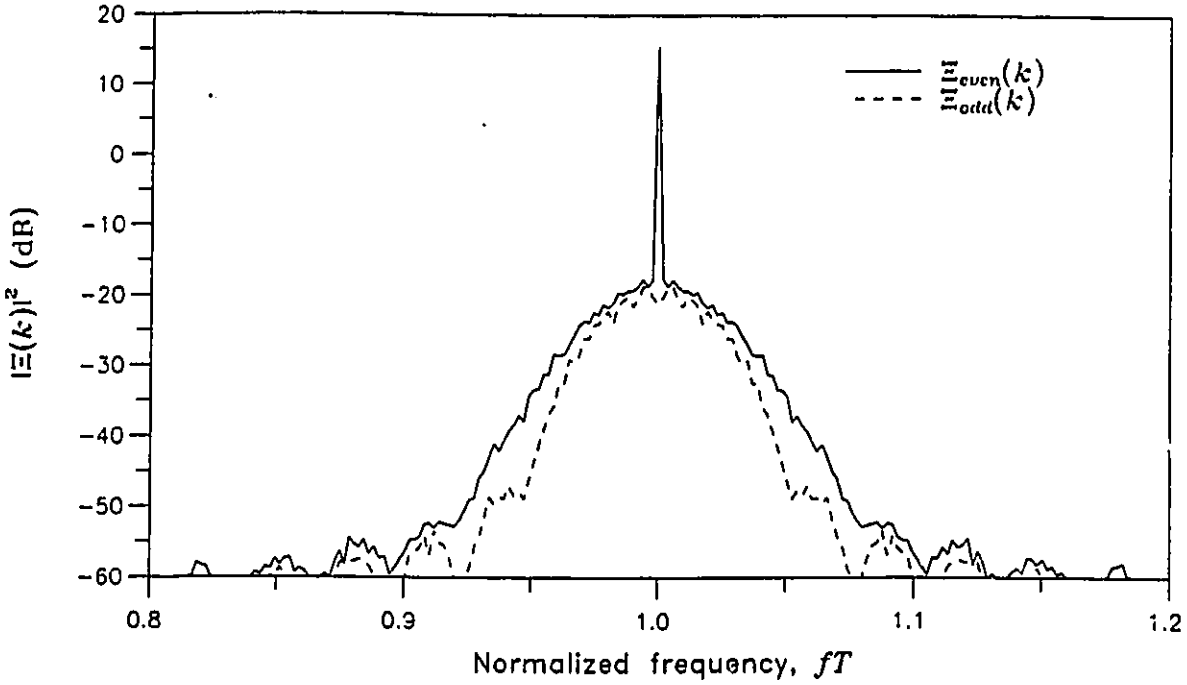

a) MSK in AWGN channel at E_b/N_0=20 dB.

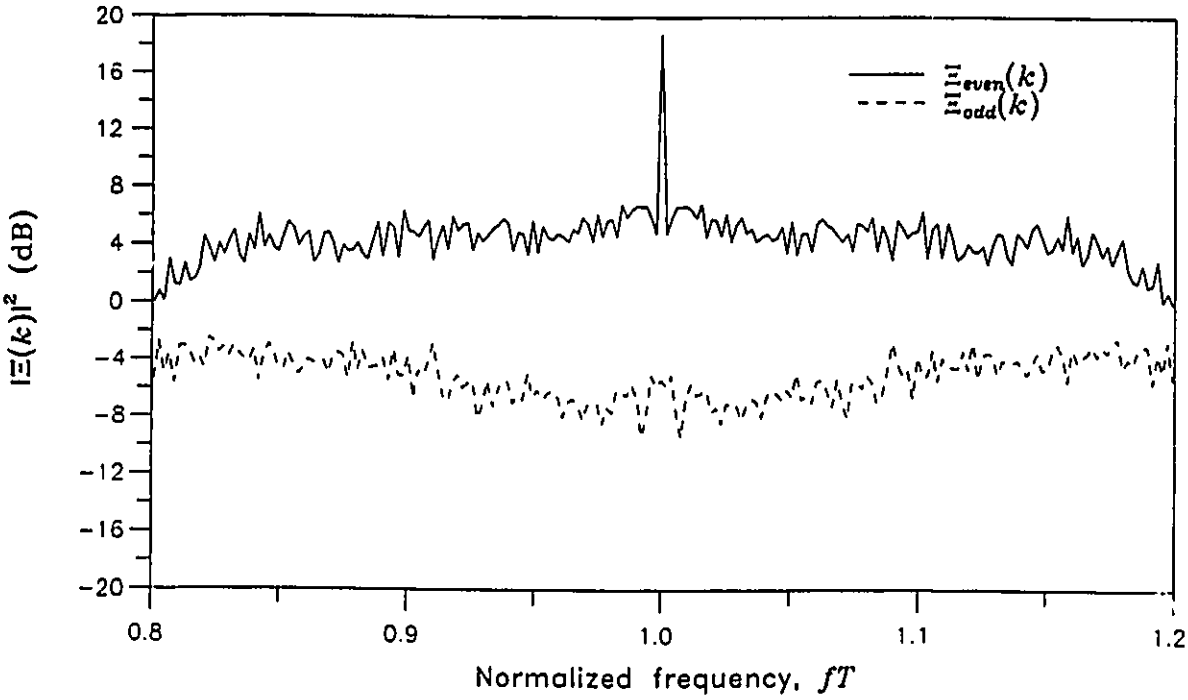

b) Binary 3N3CR in Rayleigh channel at E_b/N_0=20 dB.

Fig. 4.3. $\Xi(k)$ coefficients magnitude squared.

is be the mean $\frac{1}{30}\sum_{l=1}^{30}\hat{\sigma}_{\epsilon l}$. The precision of the resulting estimate is monitored by a 95% confidence interval, computed assuming a Gaussian probability density function for the $\hat{\sigma}_{\epsilon l}$, even though it is known that this is not a possible probability density function for a variance estimate or standard deviation (a Rician distribution would be more realistic). However, for small variance estimates, this approximation is reasonably good as shown in Fig. 4.4. Unless otherwise stated, the RMS timing jitter confidence interval results will assume a Gaussian probability density function. As a last point before looking at the results, the accuracy of the simulation is limited by the assumption that $|\Xi_{even}(k)|^2 \gg |\Xi_{even}(k+1)|^2$ which becomes less realistic for low E_b/N_0. Knowing this, it was established that no results larger than $\hat{\sigma}_\epsilon=1.25$ will be accurate enough and therefore this value represents the simulation's upper limit even though the actual system may operate properly for higher values of σ_ϵ.

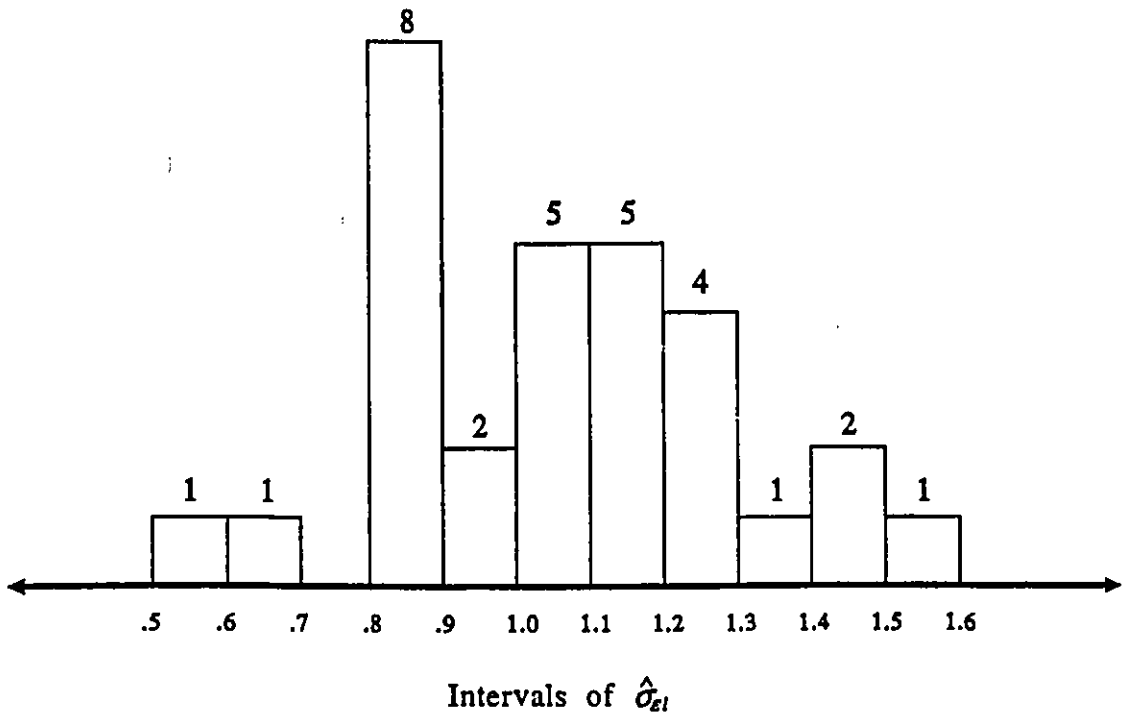

Fig. 4.4. Distribution of $\hat{\sigma}_{\epsilon l}$ for MSK at E_b/N_0=0dB ($\hat{\sigma}_\epsilon$=1.05).

4.2.4 Results

The first results are shown in Figs. 4.5 and 4.6 for a few well-known schemes (defined in Appendix A). Before comparing the results, a design example is provided to give the reader some insight for interpreting the results. The symbol rate is chosen to be 2400 symbol/s (T=0.41$\bar{6}$ msec) and the point of operation is at an E_b/N_0 of 10 dB. Finally, the allowable RMS jitter is σ_ϵ=0.03 (3% of the symbol rate). For MSK in Fig. 4.5, according to these data and the constraints $B_x T$=2, $B_\psi T$=0.01, the bandwidth of the input zonal filter is B_x=4800 Hz, and the bandwidth of the multitone filter is B_ψ=24 Hz. At E_b/N_0=10 dB, $\hat{\sigma}_\epsilon \simeq .21$ and the bandwidth of the narrow bandpass filter at $1/T$ is given by $B=\frac{(0.03)^2}{(\hat{\sigma}_\epsilon)^2 T} \simeq 49$ Hz. Now, returning to Figs. 4.5 and 4.6, some of the simulation results are compared with previous theoretical results found in [38]. For the binary AWGN channel, both sources of results give comparable performance. They diverge only at low and high E_b/N_0 because the effect of the input zonal filter was neglected in [38]. For high E_b/N_0 the saturation is typical of many practical systems and was found to be sensitive to the bandwidth of the input zonal filter B_x. The divergence at low E_b/N_0 is more troublesome but is characteristic of nonlinear systems. Note that the theoretical curves are not exactly linear either at low E_b/N_0. The degradation for an LREC pulse shape at high E_b/N_0 is more significant. In the range 8-25 dB, the jitter approximately doubles for each increment of L. MSK and 2RC have similar behavior in terms of timing jitter, despite possessing different signal bandwidths. The same observation holds for 2REC and TFM [26]-[28] except that this time the two bandwidths are comparable. As one can also see, 2RC performs better than 2REC probably because there is more power in the periodic components of 2RC than in those of 2REC. Fig. 4.6 also shows the performance of 2RC in two FFF channels. The degradation is more important for $(|m_c|^2+\sigma_c^2)E_b/N_0$>20 dB while below this range the degradation is almost constant compared to the AWGN channel. The performances are almost identical for the Rayleigh and Rician (K=0 dB) channel below 20 dB which implies that the additive noise is the primary source of degradation, while above 20 dB, the self-noise passed through the multiband filter, $\Psi(f)$, is responsible for the large timing jitter. Recall that the passband width of the multiband filter has to accommodate the fading process.

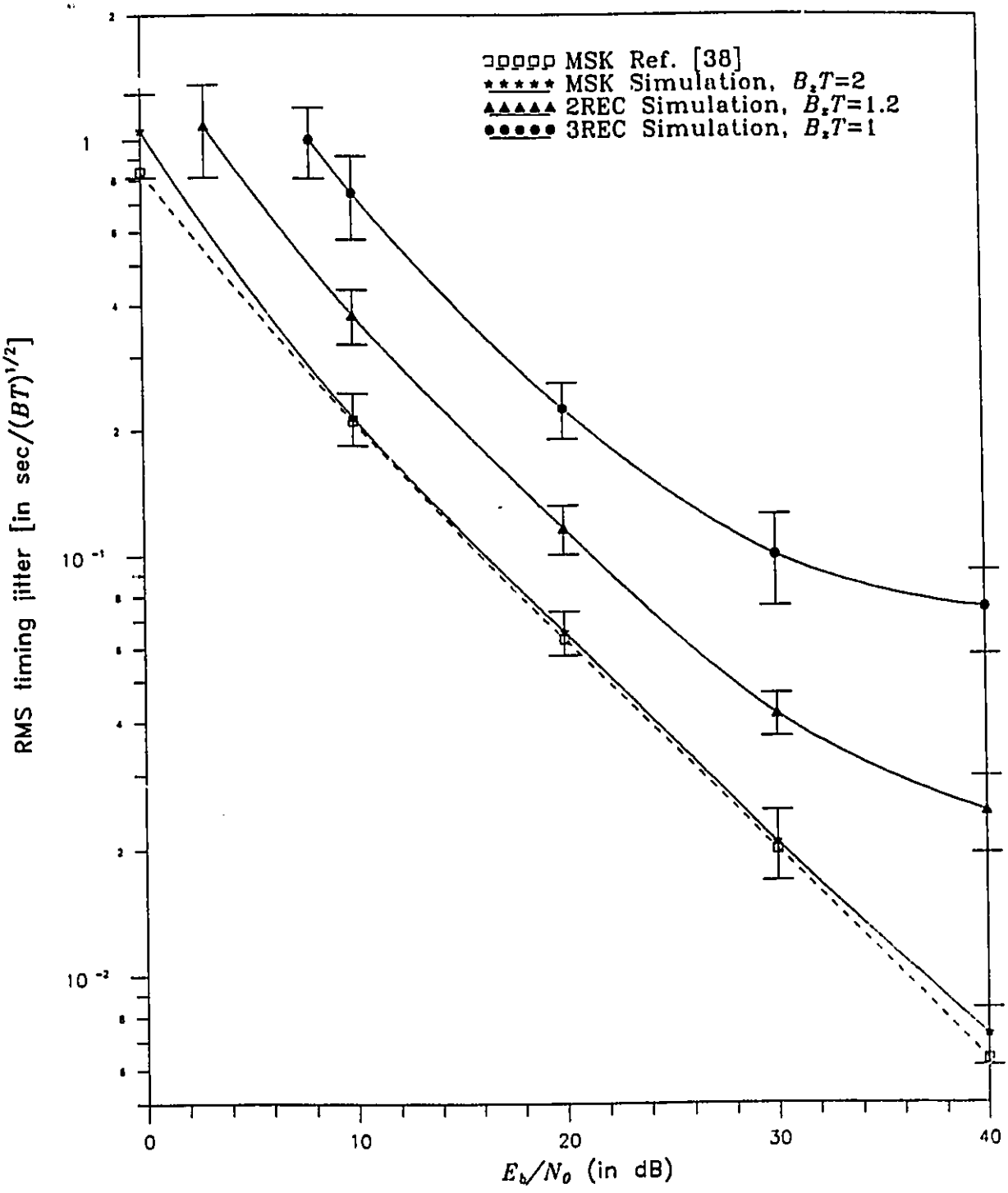

Fig. 4.5. MSK, binary 2REC and 3REC RMS timing jitter in an AWGN channel.

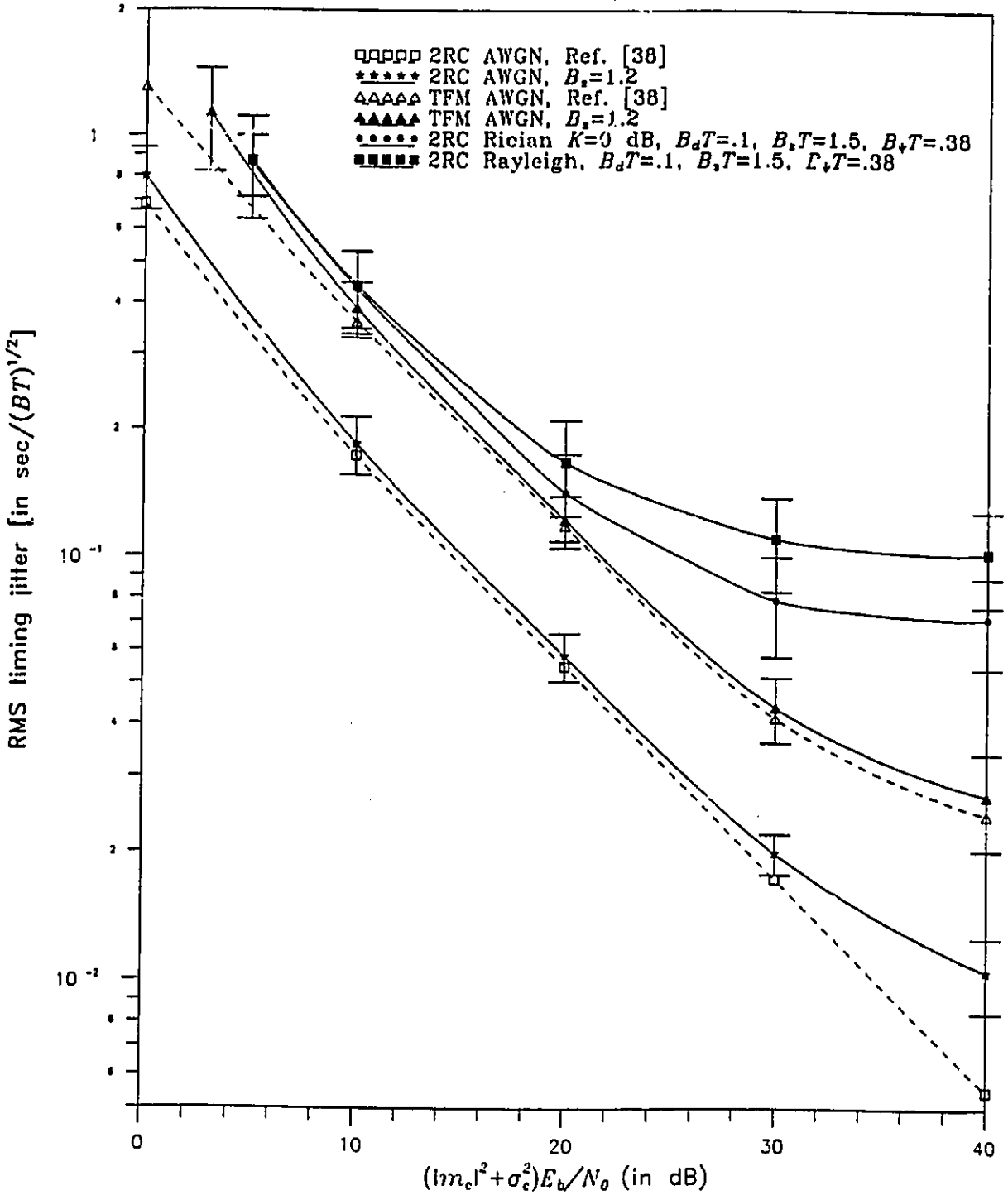

Fig. 4.6. Binary 2RC and TFM RMS timing jitter.

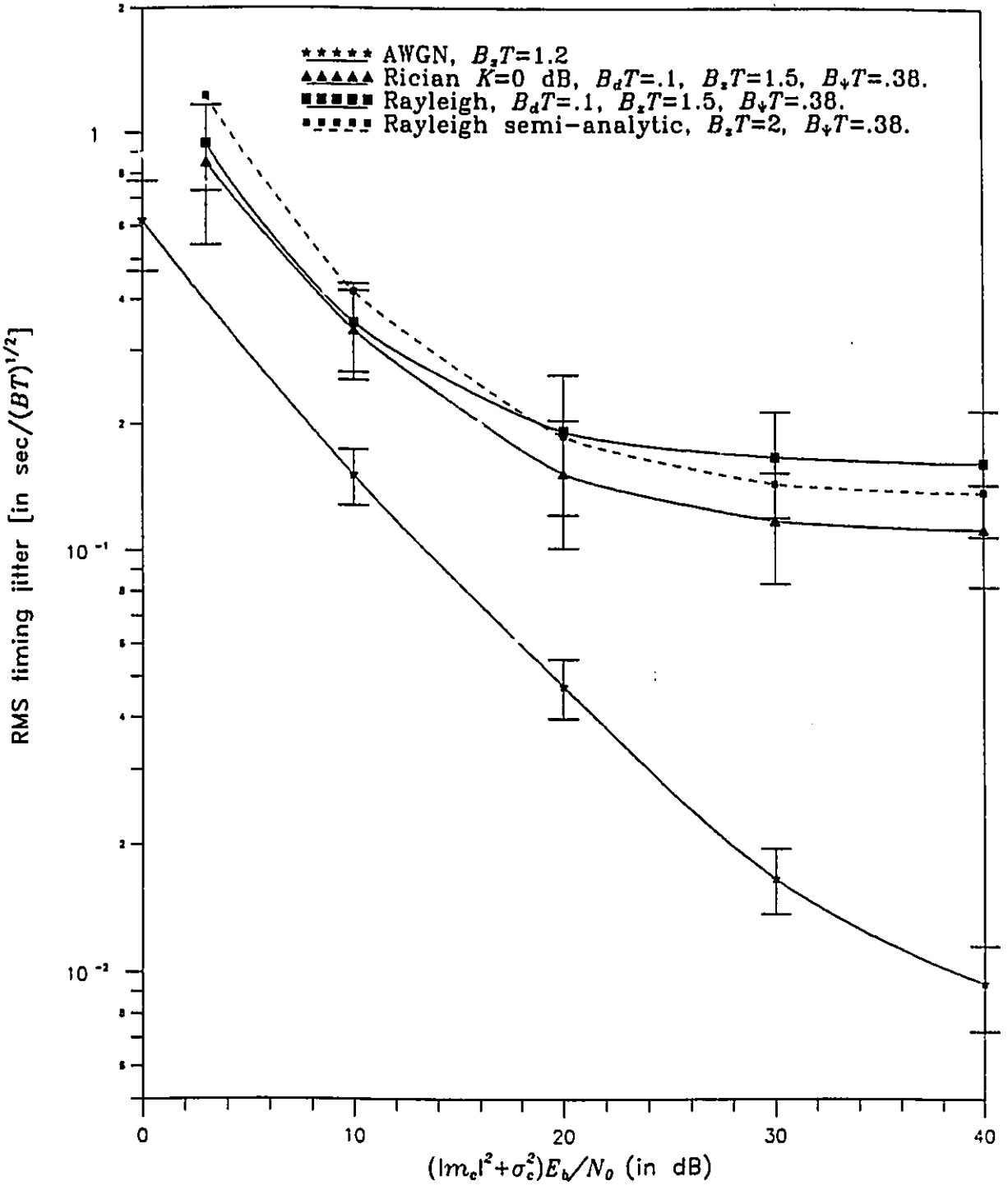

Fig. 4.7. Binary 3N3CR RMS timing jitter.

The 3N3CR pulse shape in Fig. 4.7 performs similarly to MSK but with a smaller signal bandwidth (B_zT=1.2). Nyquist III achieve good performances because they have a lot of power in their discrete components. Also shown in Fig. 4.7 is the performance for a Rician (K=0 dB) and Rayleigh channel. The degradation is not highly dependent on K when it is larger than 0 dB, as for 2RC. For $-\infty<K<0$, the range of $\hat{\sigma}_\epsilon$ is much more important particularly at high $(|m_c|^2+\sigma_c^2)E_b/N_0$. In general the saturation occurs at lower $(|m_c|^2+\sigma_c^2)E_b/N_0$ than for the AWGN channel but is still acceptable in the overall range. The variance of the estimate is increased because the envelope fluctuation now affects the timing tone. Note also that for binary signalling the results are slightly worse than those for 2RC in the same channels, at high $(|m_c|^2+\sigma_c^2)E_b/N_0$. The dashed line shows a semi-analytic result where the denominator in (4.2.5) has been replaced by the theoretical value m_β^2 mentioned in §3.3.4. It behaves as expected i.e., better than Rayleigh with B_zT=1.5 at high $(|m_c|^2+\sigma_c^2)E_b/N_0$ and worse at low $(|m_c|^2+\sigma_c^2)E_b/N_0$, and indicates that the assumption made in the analysis is realistic.

The performances for quaternary schemes are shown in Figs. 4.8 and 4.9. Note that the performance shows a slight degradation, relative to the binary case, for the Nyquist III pulse shapes 1REC and 3N3CR pulses in the AWGN channel for the midrange of E_b/N_0. Also, the plateau is in general at a higher value of $\hat{\sigma}_\epsilon$ compared to the binary cases. The effect of bandlimiting at high E_b/N_0 is now more severe and is again a reflection of the input zonal filter action on the CPM signal. For example, the dashed line in Fig. 6 shows the timing jitter for 1REC with B_zT=1.6 and comparison with the result for B_zT=2 illustrates the degradation at high E_b/N_0 where self-noise dominates. At low E_b/N_0, the degradation increases faster compared to the binary schemes. For 2RC the degradation is more significant. 1REC and 2RC were similar for the binary schemes while 2RC has now twice the RMS jitter of 1REC in the lowest half of $(|m_c|^2+\sigma_c^2)E_b/N_0$. 3REC and TFM are not shown because of poor power in the periodic component after $(\cdot)^M$. On the other hand, 2REC has acceptable power but the four phases of the tones result in destructive interference for the tone at $1/T$ after the squared envelope detector. In the FFF channel, 2RC and 3N3CR suffer major degradation compared to binary

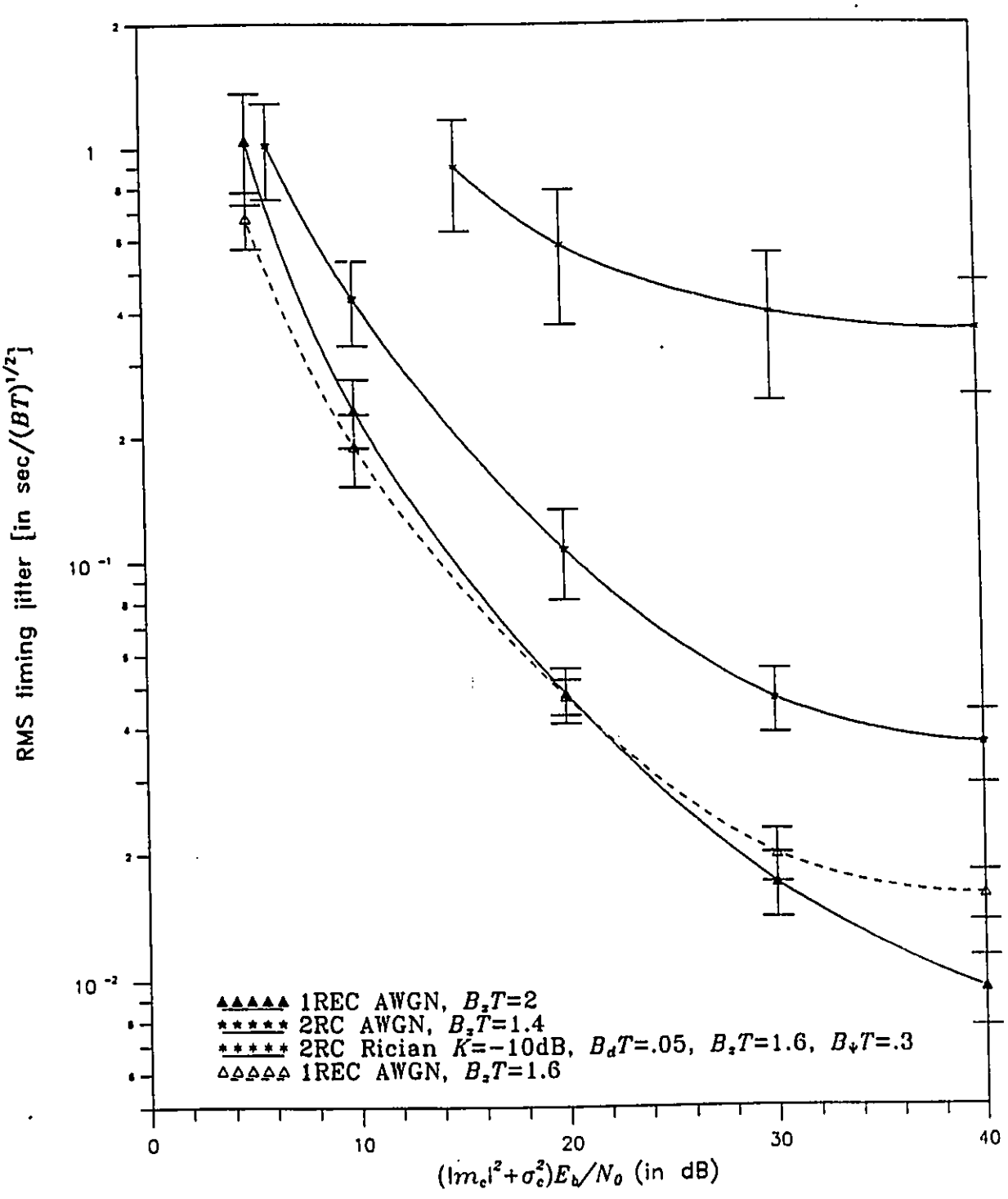

Fig. 4.8. Quaternary 1REC and 2RC RMS timing jitter.

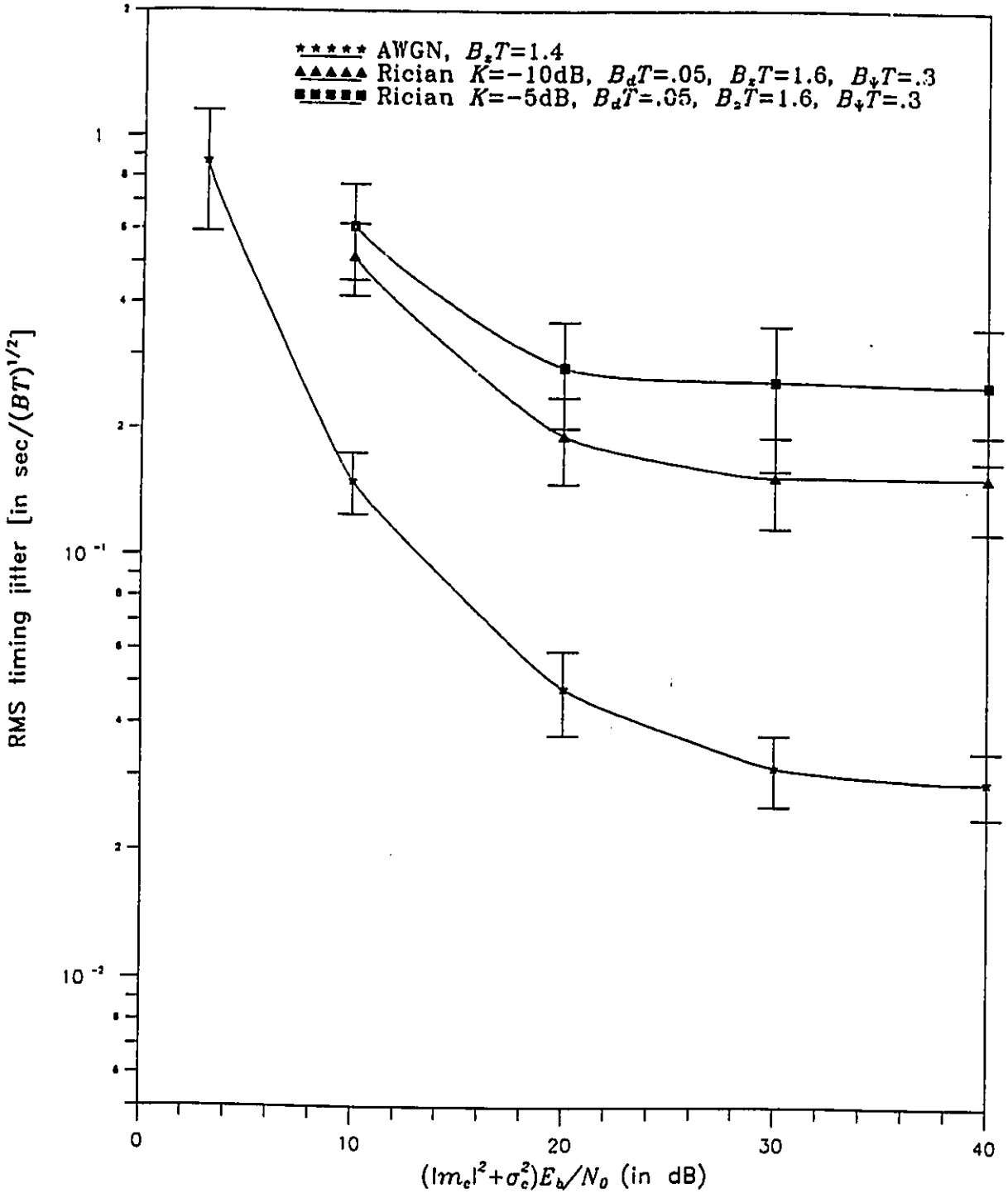

Fig. 4.9. Quaternary 3N3CR RMS timing jitter.

performance and compared to the AWGN channel. For the small K factors used here, where most of the received signal power is from the direct path, better results can probably be obtain by choosing the bandwidth of the multiband filter based on the direct path only. 3N3CR is now better than 2RC for comparable channel distortion. A semi-analytic trial was made for 3N3CR in the Rayleigh channel and although the jitter was still acceptable ($\approx$2), the tone to noise ratio in the inphase component of (4.2.2) was very low making the small angle assumption unrealistic. The effects of the envelope variations at the system output must be reduced by averaging the inphase noise in addition to only the quadrature noise in the preceding cases.

Eighth-order modulation suffers a major loss in performance. The increase from order 4 to order 8 has dramatically affected both 1REC and 2RC shown in Fig. 4.10. 2RC degradation is due to partial destructive behavior in the construction of the $1/T$ tone from the seven tones present at the M-law device output, combined with weak discrete frequency component power. 1REC is less affected because of better periodic component power and full constructive interference. For 3N3CR, the degradation is not drastic for medium and high E_b/N_0 in the AWGN channel. The tendency observed for M=2 and 4 at low and high E_b/N_0 is now clearly apparent. A semi-analytic trial leads to an unacceptable timing jitter for 3N3CR in the Rayleigh channel (B_dT=0.04). Also, all the trials in the Rician channel failed to permit the computation of reliable estimates of the timing jitter for the large fading bandwidths of interest here. This is an indication that the self-noise passed through the multitone filter, $\Psi(f)$, is the dominating factor in the jitter computation for eighth-order modulation.

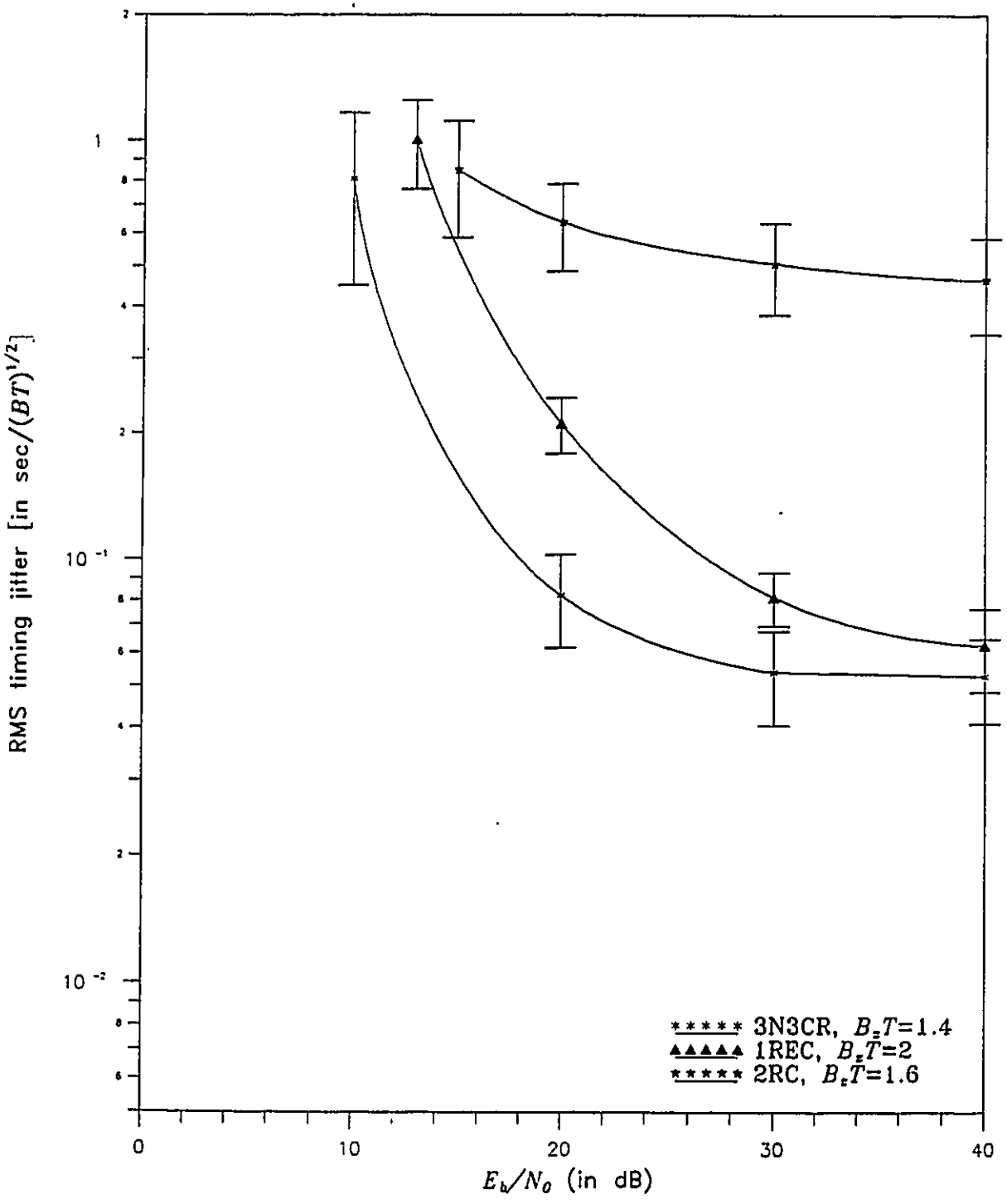

Fig. 4.10. 8-ary 3N3CR, 1REC and 2RC RMS timing jitter in an AWGN channel.

To conclude this section, the design example has been carried on for several of the CPM schemes studied above. The different filter bandwidths, B_z, B_ψ, and B are given below:

Binary

AWGN (B_ψ=24 Hz)

MSK:	B_z=4800 Hz	$B\simeq$49 Hz ($\hat{\sigma}_\epsilon\simeq$.21)
2RC:	B_z=2880 Hz	$B\simeq$63 Hz ($\hat{\sigma}_\epsilon\simeq$.185)
TFM:	B_z=2880 Hz	$B\simeq$13.5 Hz ($\hat{\sigma}_\epsilon\simeq$.4)
3N3CR:	B_z=2880 Hz	$B\simeq$110 Hz ($\hat{\sigma}_\epsilon\simeq$.14)

Rayleigh (B_d=240 Hz, B_ψ=912 Hz)

2RC:	B_z=3600 Hz	$B\simeq$12 Hz ($\hat{\sigma}_\epsilon\simeq$.43)
3N3CR:	B_z=3600 Hz	$B\simeq$18 Hz ($\hat{\sigma}_\epsilon\simeq$.35)

Quaternary

AWGN (B_ψ=24 Hz)

1REC:	B_z=4800 Hz	$B\simeq$45 Hz ($\hat{\sigma}_\epsilon\simeq$.22)
2RC:	B_z=3360 Hz	$B\simeq$12 Hz ($\hat{\sigma}_\epsilon\simeq$.42)
3N3CR:	B_z=3360 Hz	$B\simeq$110 Hz ($\hat{\sigma}_\epsilon\simeq$.14)

Rician (B_d=120 Hz, K=$-$5 dB, B_ψ=720 Hz)

3N3CR:	B_z=3840 Hz	$B\simeq$3.3 Hz ($\hat{\sigma}_\epsilon\simeq$.81)

8-ary

AWGN (B_ψ=24 Hz)

3N3CR:	B_z=3360 Hz	$B\simeq$3.3 Hz ($\hat{\sigma}_\epsilon\simeq$.82)

In the cases where $B>B_\psi$ the actual RMS timing jitter is going to be smaller then the specified value of 0.03 since the assumptions made to derived the results are not fully satisfied (see preceding section).

4.3 Practical Considerations

The baseband synchronizer studied so far has been described in terms of analog signals. For low symbol rates, the synchronizer is well suited for implementation in the discrete-time domain. Such a realization has little impact on the synchronizer performance for appropriate modulation schemes. The complexity of the synchronizer can be significantly reduced if some of the blocks in Fig. 3.1 are well designed, for instance the multitone filter and the NBPF. To give a brief idea of the importance of such a design, I will point out two possible techniques appropriate for efficient implementation. There are also a few other aspects of the system that have to be mentioned such as oscillator accuracy, sampling shifting devices and signal dynamic range.

4.3.1 Multitone Filter Design

The multitone filter has M bandpass regions of bandwidth B_ψ centered at odd multiples of $1/2T$ from $-(M-1)/2T$ to $(M-1)/2T$. The design of such a digital linear phase filter can be carried out using standard techniques like windowing, frequency sampling, and equiripple approximation [46]. While each of these techniques have their respective advantages and disadvantages, the direct structure filter tap length of the designed filter is inversely proportional to the transition bandwidth. Since it has been decided to use a bandpass shape approximating the ideal bandpass filter, the resulting filter impulse response $\psi(t)$ may end up with an unreasonable number of taps, especially for the AWGN channel or when M gets large. To reduce the computational requirements, a filter structure based on multirate digital signal processing [47][48] may be used. This structure reduces the proportionality between the transition bandwidth and the number of tap multiplications to get acceptable computing effort. Fig. 4.11 shows the basic idea in a block diagram form. The complex sequence $y(n)$ coming from the M-law nonlinearity is first decimated by 2. The decimation filter will in most cases be a very simple filter, in particular if halfband filter design is used (allowing aliasing in the transition region of the decimated signal). For a filter length of N_1 taps, the number of multiply and add computations per second is $(N_1+3)\,F_s/2$ where $F_s=\frac{1}{T_s}=\frac{2M}{T}$. The decimation filter will simply attenuates the frequency

Fig. 4.11. Multirate multitone filter structure.

components above $\frac{F_s}{4}+\delta f$ such that the decimated signal $y'(n)$ does not have significant aliasing in the region below $\frac{F_s}{4}-\delta f$. The next filter is a multiband filter which can efficiently be implemented by using the property of an upsampled sequence. To show this, a design procedure is given and illustrated in Fig. 4.12. First, the design of a highpass filter with appropriate shape and bandwidth B_ψ is performed at the sampling rate of $1/T$. The bandpass region of the filter is then at $1/2T$ [Fig. 4.12 a) and b)]. Now, by inserting $(M-1)$ zeros between the N_2 taps of the designed highpass filter, the sampling rate is increased to M/T with bandpass region at odd multiples of $1/2T$. This is the desired frequency response for the multitone filter at sampling rate $F_s/2$. It is this zero padded impulse response that is used to filter $y'(n)$. The computational effort is therefore $2N_2$ multiply-add operations per sample at a sampling rate of $F_s/2$. The implementation would involve M input buffers of length N_2 filled sample by sample alternatively and convoluted at there respective filling instant. This is simply expressed as

$$x'(n) = \sum_{i=1}^{N} \psi(i)\; y'(n - iM). \tag{4.3.1}$$

The signal $x'(n)$ is then send to an interpolator to get back to the original sampling rate for the next operation. The interpolation filter therefore operates or an input signal with every second sample set to zero. Again, halfband filter can be used to further reduce the computational effort. Doing so we find that $(N_3+3)\,F_s/2$ multiply-add per second must be computed for this filter where N_3 is the filter length in tap. The overall computational effort is then

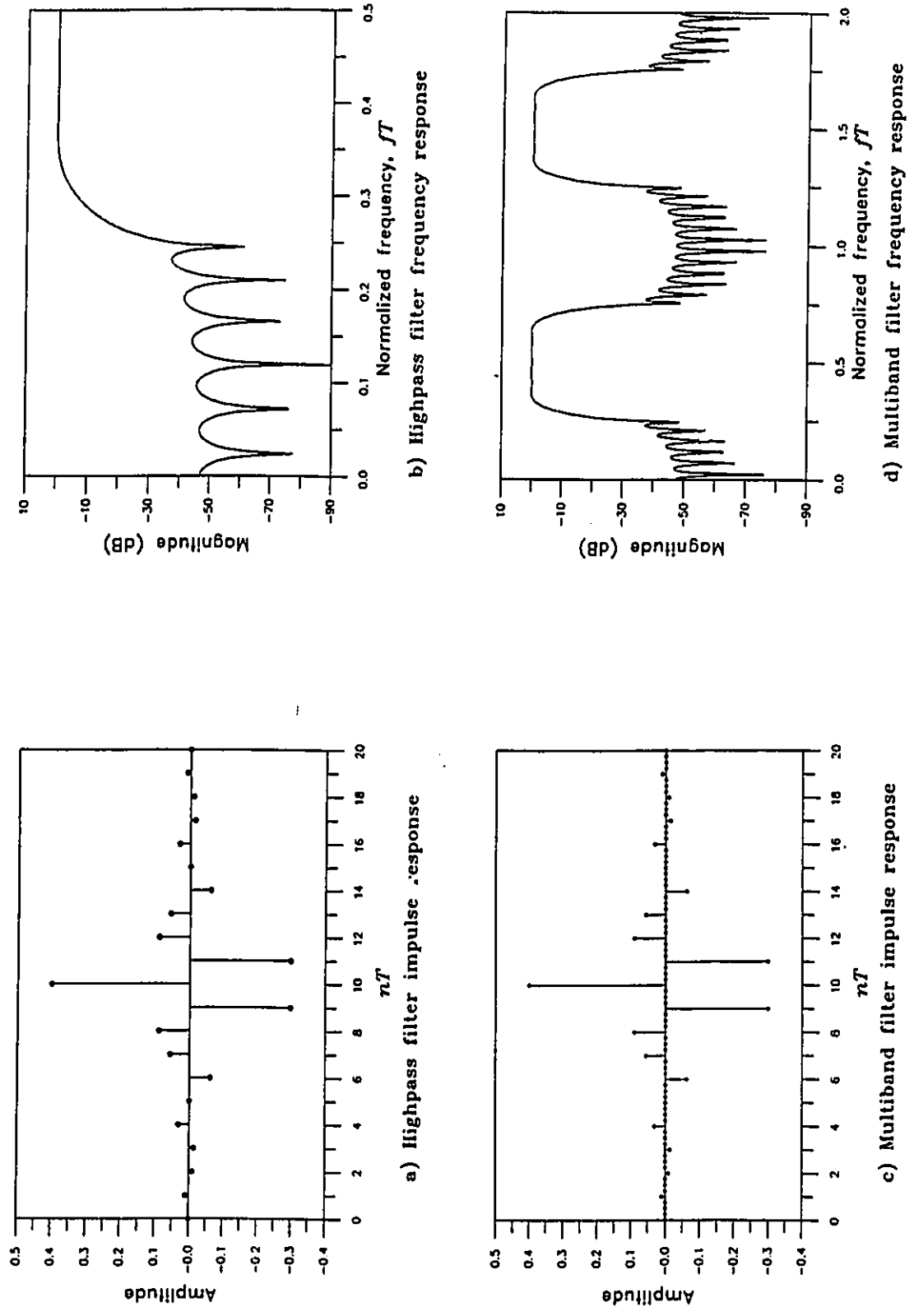

Fig. 4.12. Design example of multiband filter.

$$\#\text{ multiply-add/sec} = \left(N_1 + 2N_2 + N_3 + 6\right)\frac{F_s}{2}. \tag{4.3.2}$$

To give an idea of the savings achievable, an example is now provided. The bandpass shape has bandwidth $B_\psi T$=0.2 with transition bandwidth of $1/10T$ on each side. The desirable ripple is of 0.05 in the stopband and passband region. Note that the decimation filter, the multitone filter, and the interpolation filter would have to have ripple of 0.05/3 to get an overall ripple of 0.05 in the passband region. Using for this example the Kaiser window design method, it was found that the saving increases with M as shown in Table 8.

Table 8. Computation comparison between direct and multirate filter structure.

	#multiply-add/sec		
Level	Direct structure	Multirate structure	Gain
M=2	110	39	2.8
M=4	222	55	4.0
M=8	446	79	5.6

As one can see, the gain over the direct structure is substantial and can easily be larger for very small transition bandwidths, particularly for the AWGN channel. This saving in #multiply-add/sec is achieved at the expense of a more complex filter architecture but it is felt that the price is sufficiently low to favor the multirate structure for most applications.

4.3.2 Narrowband Filter Design

The timing jitter of the sampling clock is directly proportional to the bandwidth of the NBPF at $1/T$. For acceptable jitter, we face the problem of designing a filter with a very narrow bandwidth and a very narrow transition band. As was mentioned in the previous section, a direct structure to this filter design problem will lead to a filter with a very large number of taps which would require

intensive computational effort. To reduce the computational burden, other structures have to be examined. The multirate structure combined with digital down conversion is an elegant solution to the stated problem, that provides narrowband filtering with a constant delay (i.e., linear phase). The basic idea is illustrated in Fig. 4.13. The down conversion will shift the tone at $1/T$ to DC along with the signal components surrounding it. The complex signal generated is then feed through a chain of decimation filters. An efficient realization of this chain would consist of several stages of decimation-by-2 using halfband filters. The output signal $\tilde{\beta}(n)$ is simply a noisy DC phasor with an angle (assuming that the phase corresponding to the synchronizer's filter delay has been removed) proportional to an average sampling misadjustment. This angle can then be used to delay or advance the sampling clock.

This structure is found to be very simple, linear and computationally efficient. The computational efficiency compared to the direct structure can be appreciated by looking at an example with specification:

normalized bandwidth BT :	0.001
normalized one sided transition bandwidth :	0.0005
stopband and passband ripple :	0.01.

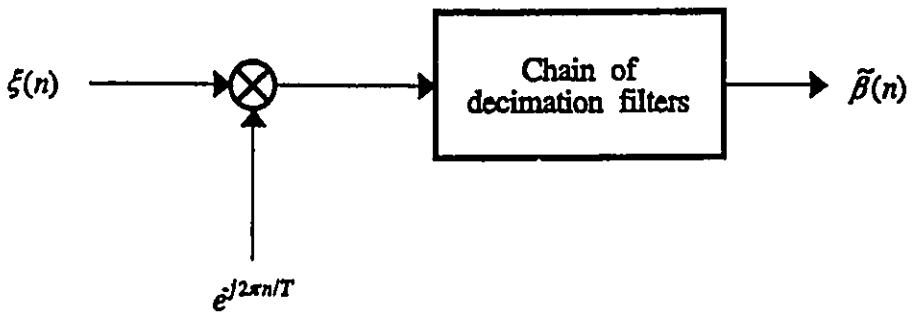

Fig. 4.13. Down conversion and multirate filter structure.

With the direct structure it is found that the number of multiply-add/sec (Kaiser window design) is $35718\,F_s$, which does not make sense from the practical point of view. The same filter specifications can be met using the multirate structure with a computational effort of $14.09F_s$ (10 stages of filtering). This approach results in significant savings in both computational effort and memory requirements. The filter structure can easily be made modular so that modification to increase or decrease the number of stages is straightforward. Therefore, the filtering of the timing tone does not represent a major problem in an efficient implementation of the studied synchronizer.

4.3.3 Practical Devices

• The results shown in §4.2 and the previous section suggest that the timing clock jitter can be specified just by specifying the bandwidth of the narrowband filter. However, practical clock accuracies are not unlimited and the filter bandwidth must reflect the constraint imposed by a particular system clock accuracy. It is fairly common to deal with clock accuracies in the order of 10^{-5} so that averaging over up to 1000 symbols (BT=0.001) will not cause an error larger than $\approx$1% of the symbol period. If larger averaging periods are required, a clock accuracy of up to 10^{-8} and more can be achieved. However, oscillator costs escalate with increasing accuracy. For fading channels, a highly stable clock would also be appropriate to keep clock synchronization after moments of deep fade.

• The phasor at the output of the narrowband filter could be used as a means to correct the sampling clock. This operation is not trivial to perform if small corrections are necessary. Several techniques may be employed but recent data acquisition products with interesting features are now available for low data rate transmission. The Texas Instruments TLC32040 chip family [49] allows the analog-to-digital conversion timing to be advanced or retarded by an amount much smaller than the sampling period, appropriate for timing tracking purposes. The device also integrates a bandpass switched capacitor antialiasing input filter, a 14-bit resolution analog-to-digital converter, a 14-bit resolution digital-to-analog converter and a lowpass switched capacitor output reconstruction filter.

• The analysis made in Chapter 3 assumed that the received signal has been down converted to baseband. A carrier frequency misadjusment will lead to a frequency offset at baseband that may disturb the synchronizer performance. The offset tones at baseband must be able to pass through the multitone filter for proper operation. To get close to the predicted performance of §4.2 the offset must to be very small so that B_ψ does not need to be increased significantly. This can be achieve through system specification with very stable carrier frequency oscillators or with tight down-converter and automatic frequency control performance in terms of frequency stability requirements.

• The output signal of the $(\cdot)^M$ and $|\cdot|^2$ nonlinearities will exhibit a high dynamic range, particularly for large M in a fading channel. If implemented with a fixed-point arithmetic digital signal processor[11], the internal representation would have to be performed with a sufficient resolution such that the dynamic range is preserved and that rounding or truncation does not significantly alter the signal. This can increase the computational requirements if extended-precision arithmetic has to be used. Fortunately, general purpose floating-point digital signal processors exist for which high dynamic range requirements are not a problem. ■

[11] Similar remark for analog implementation.

Chapter 5

CONCLUSIONS

Various aspects of symbol synchronization for CPM have been studied in this thesis. The power available for timing purposes when a CPM signal with modulation index $1/M$ is passed through an M-law device has been investigated for several types of pulse shapes. In general, this power decreases as the pulse shape length and the symbol set size increase. For pulse shapes satisfying Nyquist III criterion, results indicate that the reduction of the discrete tone power is primarily a function of M, instead of M and L. Also, the Nyquist III pulse shapes have good timing properties in the context of CPM because they are free of intersymbol interference at the sampling instant. Then in Chapter 3, a study of a synchronizer making efficient use of the timing information was made. The synchronizer processes a signal disturbed by multiplicative and additive noise to recover a sinusoidal signal at the symbol rate related to the sampling instant. Analysis has shown the important design and signal characteristics, i.e., the multitone filter, the phase relationships between the discrete tones for M-ary signalling, and the envelope fluctuations at the system output, throughout the synchronizer path. The analysis did not permit a complete statistical characterization of the timing signal. Therefore a simulation method, found in Chapter 4, was used to quantify the synchronizer behavior for several known CPM schemes by estimating the RMS timing jitter. For binary signalling, a variety of CPM schemes to be used in the AWGN and fast flat-fading channel have been compared, from the symbol timing tracking point of view. From the results obtained, it is believed that the studied synchronizer will give adequate performances for any binary CPM scheme with good power in its discrete components after the $(\cdot)^2$ device, and this over a static or fading channel. For quaternary schemes, Nyquist III pulses have good timing properties over the AWGN channel, and potential self-timing

capabilities for moderately severe fast flat Rician channels. Other type of pulses must be studied more carefully to find the phase relationships and the power of the discrete components. As an example, 2RC gives results comparable to 3N3CR but 2REC does not show acceptable performance. For eighth-order modulation, application of this approach appears to be limited to AWGN and Rician (small K values) channels with CPM schemes using Nyquist III pulse shapes for this synchronizer structure. Finally, practical considerations concerning the implementation of the filters found in the synchronizer has been discussed. In general, the synchronizer is well suited for implementation using digital signal processing techniques.

Research in the domain of symbol synchronization is an important area for future work in digital communications. Previous symbol synchronization techniques based on analogue signal processing are not always attractive or suitable for digital implementation. Also, new or sophisticated modulation schemes require symbol synchronization. Unfortunately, new synchronization algorithms are often relegated to a secondary position, relative to symbol detection algorithms, in the study of digital communication systems. The use of well-known modulation schemes transmitted over different types of disturbing channels is also a potential area for future research. A general approach applicable for the particular case of CPM is a statistical characterization of the timing error ϵ for a given synchronizer structure. In many cases (as in this thesis), the measured quantity is the variance of ϵ. Ideally, the characterization would be the probability density function of ϵ. With this function, many other aspects of a communication system could be studied. As an example symbol error rate found with ideal synchronization may be updated to account for the symbol timing error. Another important characterization of ϵ is the renewal phase distribution which is used to study phenomena like cycle slips [43] that are occurring at a very low rate (hours or days). The occurrence of a cycle slip results in a burst of errors, and this phenomena is often not consider in the evaluation of a complete system symbol error rate. However, this is generally, a very hard task to achieve. More specifically for this synchronizer, three topics can be pointed out for future research work. First, it would be interesting to derive an analytic approximation to verify the simulation results. This would probably require very

good mathematical skill. Secondly, improvements in the synchronizer may be found by designing the multitone filter according to some optimum criterion like the minimum mean square error criterion. Thirdly, an investigation can be performed to determine if it is possible to make efficient use of the timing information in the tone at multiples of $1/T$ at the output of the squared envelope detector. This could improve the synchronizer performance, at the expense of a more complicated structure. ■

APPENDIX A

List of Pulse Shapes

We assume for the present pulse shape definition that $g(t)$ is real. The pulse shape are divided in two categories: band-limited and time-limited. The first category are pulse shape defined in the frequency domain and have therefore to be inverse Fourier transformed following by truncation to evaluate $g(t)$. The frequency domain filters are zero phase unless otherwise stated. The second category are time domain defined with an analytic expression for $g(t)$. These pulse shapes definitions are extracted from [22], [24] and, [26].

• Band-limited pulse shapes

Nyquist 1 Modified Cosine Rolloff (N1MCR)

$$G_{N1MCR}(f) = \begin{cases} \frac{1}{2}, & |f| < \frac{1-\alpha}{2T}; \\ \frac{1}{2}\cos^2\left(\frac{\pi f T}{2}\right), & \frac{1-\alpha}{2T} \le |f| \le \frac{1+\alpha}{2T}; \\ 0, & \text{elsewhere.} \end{cases}$$

Nyquist 1 Linear Rolloff (N1LR)

$$G_{N1LR}(f) = \begin{cases} \frac{1}{2}, & |f| \le \frac{1-\alpha}{2T}; \\ \frac{1}{2}\left[1-\frac{T}{\alpha}(f-\frac{1-\alpha}{2T})\right], & \frac{1-\alpha}{2T} \le |f| \le \frac{1+\alpha}{2T}; \\ 0, & \text{elsewhere.} \end{cases}$$

Nyquist 1 Modified Linear Rolloff (N1MLR)

$$G_{N1MLR}(f) = \begin{cases} \frac{1}{2}, & |f| < \frac{1-\alpha}{2T}; \\ \frac{1}{2}(1-fT), & \frac{1-\alpha}{2T} \le |f| \le \frac{1+\alpha}{2T}; \\ 0, & \text{elsewhere.} \end{cases}$$

Minimum Energy Nyquist 1 (ME1)

$$G_{ME1}(f) = \begin{cases} \frac{1}{2}, & |f| < \frac{1-\alpha}{2T}; \\ \frac{1}{4}, & \frac{1-\alpha}{2T} \le |f| \le \frac{1+\alpha}{2T}; \\ 0, & \text{elsewhere.} \end{cases}$$

Nyquist 1 Minimum Energy Nyquist 3 (N1ME3)

$$G_{N1ME3}(f) = \begin{cases} \frac{1}{2}, & |f| < \frac{1-\alpha}{2T}; \\ \frac{(1-fT)^2}{2\left[(1-fT)^2+(fT)^2\right]}, & \frac{1-\alpha}{2T} \le |f| \le \frac{1+\alpha}{2T}; \\ 0, & \text{elsewhere.} \end{cases}$$

Nyquist 3 & 2 (N32)

$$G_{N32}(f) = \begin{cases} \frac{\left(1+T|f|\left[\text{sinc}(2fT)-1\right]\right)}{2\ \text{sinc}(fT)}, & |f| \le \frac{1}{T}; \\ 0, & \text{elsewhere.} \end{cases}$$

Nyquist 3 Modified Cosine Rolloff (N3MCR)

$$G_{N3MCR}(f) = \frac{G_{N1MCR}(f)}{\text{sinc}(fT)}$$

Nyquist 3 Linear Rolloff (N3LR)

$$G_{N3LR}(f) = \frac{G_{N1LR}(f)}{\text{sinc}(fT)}$$

Nyquist 3 Modified Linear Rolloff (N3MLR)

$$G_{N3MLR}(f) = \frac{G_{N1MLR}(f)}{\text{sinc}(fT)}$$

Nyquist 3 Minimum Energy Nyquist 1 (N3ME1)

$$G_{N3ME1}(f) = \frac{G_{ME1}(f)}{\mathrm{sinc}(fT)}$$

Mnimum Energy Nyquist 3 (ME3)

$$G_{ME3}(f) = \frac{G_{N1ME3}(f)}{\mathrm{sinc}(fT)}$$

TFM (Tamed Frequency Modulation with a pulse shape truncated to $L=5$)

$$g(t) = \mathcal{F}^{-1}\left\{\frac{\cos^2(\pi fT)}{2\ \mathrm{sinc}(fT)}\right\}, \quad \text{for } |f|<1/2T \text{ and zero elsewhere.}$$

• Time-limited pulse shapes

L Half Cycle Sine (LHCS)

$$g_{LHCS}(t) = \begin{cases} \frac{\pi}{4LT}\sin\left(\frac{\pi t}{LT}\right), & 0 \le t \le LT; \\ 0, & \text{elsewhere.} \end{cases}$$

L TRIangular (LTRI)

$$g_{LTRI}(t) = \begin{cases} \frac{2t}{(LT)^2}, & 0 \le t \le \frac{LT}{2}; \\ \frac{1}{LT}\left(2-\frac{2t}{LT}\right), & \frac{LT}{2} \le t \le LT; \\ 0, & \text{elsewhere.} \end{cases}$$

L Cosine Rolloff (LCR)

$$g_{LCR}(t) = \begin{cases} \frac{1}{2LT}\left[1-\cos\left(\frac{2\pi t}{LT}\right)\right], & 0 \le t \le LT; \\ 0, & \text{elsewhere.} \end{cases}$$

L Convolved Raised Cosine (LCRC)

$$g_{LCRC}(t) = \begin{cases} \frac{1}{LT}\left[\frac{2t}{LT} - \frac{1}{2\pi}\sin\left(\frac{4\pi t}{LT}\right)\right], & 0 \le t \le \frac{LT}{2}; \\ \frac{1}{LT}\left[2 - \frac{2t}{LT} + \frac{1}{2\pi}\sin\left(\frac{4\pi t}{LT}\right)\right], & \frac{LT}{2} \le t \le LT; \\ 0, & \text{elsewhere.} \end{cases}$$

APPENDIX B

Joint Moment of two Complex Gaussian Random Variables

The derivation of the joint moment $\mathbf{E}\{z_1^{\iota} z_2^{*\eta}\}$ of two zero mean complex Gaussian random variables of order $\iota+\eta=c$ where $\iota,\eta \in \mathbf{N}$ is consider. The result is expressed in terms of the autocorrelation function of those two random variables. It is known that for two real random variables x and y, there joint moment of order $\iota+\eta=c$ where $\iota,\eta \in \mathbf{N}$ is given by [19]

$$\frac{\partial^{\iota}\partial^{\eta}}{\partial s_1^{\iota}\partial s_2^{\eta}}\,\Phi(s_1,s_2)\bigg|_{s_1=s_2=0}, \tag{B.1}$$

where $\Phi(s_1,s_2)$ is the moment generating function of x and y defined as $\Phi(s_1,s_2)=\mathbf{E}\left\{e^{s_1 x+s_2 y}\right\}$. This result has been applied to the special case of a $2n$-dimensional complex Gaussian random vector

$$\underline{Z}^{\mathrm{T}} = \{z_1,\cdots,z_n\}. \tag{B.2}$$

where the superscript $^{\mathrm{T}}$ denotes transpose. Defining a new vector

$$\underline{Z}'^{\mathrm{T}} = \left\{z_1^{\iota_1} z_1^{*\eta_1}\cdots z_n^{\iota_n} z_n^{*\eta_n}\right\},$$

it has been shown [44] that

$$\mathbf{E}\left\{\underline{Z}'\right\} = \frac{\partial^{\iota_1+\cdots+\iota_n+\eta_1+\cdots+\eta_n}}{\partial s_1^{\iota_1}\cdots\partial s_n^{\iota_n}\partial s_{n+1}^{\eta_1}\cdots\partial s_{2n}^{\eta_n}}\, e^{\frac{1}{2}\underline{S}^{\mathrm{T}}\underline{\Sigma}\,\underline{S}+\underline{S}^{\mathrm{T}}\underline{C}}\bigg|_{\underline{S}=0}, \tag{B.3}$$

where $\underline{C}=\mathbf{E}\{\underline{Z}\}$, $\underline{\Sigma}=\begin{bmatrix} 0 & \underline{R} \\ \underline{R}^{*} & 0 \end{bmatrix}$ with $\underline{R}=\mathbf{E}\left\{(\underline{Z}-\underline{C})(\underline{Z}-\underline{C})^{*\mathrm{T}}\right\}$, and $\underline{S}^{\mathrm{T}}=\{s_1,\cdots,s_{2n}\}$ is a real $2n$-dimensional vector. In the particular case of interest here, $\underline{S}$ is a four-dimensional vector ($n=2$) and $\underline{C}=0$. Under those conditions, the autocorrelation matrix $\underline{R}$ is simply

$$R = \mathbb{E}\left\{ \begin{pmatrix} z_1 \\ z_2 \end{pmatrix} \quad (z_1^* z_2^*) \right\} = \begin{bmatrix} \sigma_{z_1}^2 & R_{zz}(t_1,t_2) \\ R_{zz}^*(t_1,t_2) & \sigma_{z_2}^2 \end{bmatrix}, \tag{B.4}$$

and after a few steps the exponent in (B.3) is found to be

$$\tfrac{1}{2}\,\underline{S}^{\mathrm{T}}\underline{\Sigma}\,\underline{S} = s_1\left(s_3\sigma_{z_1}^2 + s_4 R_{zz}(t_1,t_2)\right) + s_2\left(s_4\sigma_{z_2}^2 + s_3 R_{zz}^*(t_1,t_2)\right). \tag{B.5}$$

Thus, for this particular case

$$\mathbb{E}\left\{z_1^i z_2^{*\eta}\right\} = \frac{\partial^{i+\eta}}{\partial s_1^i \partial s_4^\eta}\, e^{\left[s_1(s_3\sigma_{z_1}^2 + s_4 R_{zz}(t_1,t_2)) + s_2(s_4\sigma_{z_2}^2 + s_3 R_{zz}^*(t_1,t_2))\right]}\Big|_{\underline{S}=0}, \tag{B.6}$$

and differentiating first with respect to s_1 gives

$$\frac{\partial^i}{\partial s_1^i}\, e^{\frac{1}{2}\underline{S}^{\mathrm{T}}\underline{\Sigma}\,\underline{S}} = \left(\sum_{i=0}^{i}\binom{i}{i}\left[s_3\sigma_{z_1}^2\right]^{i-i}\left[s_4 R_{zz}(t_1,t_2)\right]^i\right) e^{\frac{1}{2}\underline{S}^{\mathrm{T}}\underline{\Sigma}\,\underline{S}}. \tag{B.7}$$

Since the final solution is the evaluation of (B.6) at $\underline{S}=0$, all the terms with $\left[s_3\sigma_{z_1}^2\right]^{i-i}$ $(i \neq \imath)$ will go to zero because the derivative with respect to s_3 is not taken. Rearranging the exponent of (B.6), it is necessary to solve

$$\frac{\partial^\eta}{\partial s_4^\eta}\left(s_4^i\, R_{zz}^i(t_1,t_2)\, e^{\left[s_4(s_2\sigma_{z_2}^2 + s_1 R_{zz}(t_1,t_2)) + s_3(s_1\sigma_{z_1}^2 + s_2 R_{zz}^*(t_1,t_2))\right]}\right)\Big|_{\underline{S}=0}. \tag{B.8}$$

Now, using $\frac{d^\eta uv}{ds^\eta} = \sum_{i=0}^{\eta}\binom{\eta}{i}\frac{d^i u}{ds^i}\frac{d^{\eta-i}v}{ds^{\eta-i}}$ and keeping only the term $i=n$ $\left(u = s_4^i\, R_{zz}^i(t_1,t_2)\right)$ for the same reason as above, yields

$$\mathbb{E}\left\{z_1^i z_2^{*\eta}\right\} = R_{zz}^i(t_1,t_2)\, e^{\frac{1}{2}\underline{S}^{\mathrm{T}}\underline{\Sigma}\,\underline{S}}\,\frac{d^\eta s_4^i}{ds_4^\eta}\Big|_{\underline{S}=0}. \tag{B.9}$$

Noting that

$$\frac{d^{\eta} s_4^{\iota}}{ds_4^{\eta}} = \begin{cases} \frac{\iota!}{(\iota-\eta)!}\, s_4^{(\iota-\eta)}, & \iota > \eta; \\ \iota!, & \iota = \eta; \\ 0, & \iota < \eta, \end{cases}$$

it can easily be seen that (B.9) reduces to the final result

$$\mathbb{E}\left\{z_1^{\iota} z_2^{*\eta}\right\} = \begin{cases} \eta!\; R_{zz}^{\eta}(t_1,t_2), & \iota = \eta; \\ 0, & \iota \neq \eta. \end{cases} \tag{B.10}$$

APPENDIX C

Joint Moment of two Complex CPM Signals

The derivation of the joint moment $\mathbf{E}\left\{e^{j\iota\phi(t_1,\underline{a})}\, e^{-j\eta\phi(t_2,\underline{a})}\right\}$ of two complex CPM signals of order $\iota+\eta=c$ where $\iota,\eta \in \mathbf{Z}$ is consider. It is assumed here, as in §2.3, that the frequency pulse shape satisfies the constraint given in (2.3.3). The approach follows [33] with the cyclostationary version of the joint moment instead of the stationarized version. The case where $\iota=\eta$ is simply the autocorrelation (or its complex conjugate) of a complex CPM signal raised to the power η, and it will be denoted ${}_{\eta}R_{uu}(t_1,t_2)$ (see §2.3.4). For the other cases, we know that (see equations 2.3.22 and 2.3.23)

$$\mathbf{E}\left\{e^{j\iota\phi(t_1,\underline{a})}\, e^{-j\eta\phi(t_2,\underline{a})}\right\} = \prod_i \sum_{\substack{k=-(M-1)\\ k\ \text{odd}}}^{M-1} P_k\, e^{j2\pi hk[\iota q(t_1-iT)-\eta q(t_2-iT)]} \tag{C.1}$$

and restricting t_1 to be greater or equal to t_2 (the reverse condition is related to the complex conjugate of the present development), use can be made of the constraint (2.3.3) to find the range over which the product takes place.

In order to simplify the expression for $\mathbf{E}\left\{e^{j\iota\phi(t_1,\underline{a})}\, e^{-j\eta\phi(t_2,\underline{a})}\right\}$, the largest i for which $t_2-iT\geq LT$ is of importance and will be denote i_2. Since $t_1\geq t_2$ it is clear that $t_1-iT\geq LT$ when $i\geq i_2$ and

$$\iota q(t-iT)-\eta q(t-iT)=\tfrac{1}{2}(\iota-\eta), \qquad i\leq i_2=\left\lfloor\frac{t_2}{T}\right\rfloor-L. \tag{C.2}$$

Thus

$$\mathbf{E}\left\{e^{j\iota\phi(t_1,\underline{a})}\, e^{-j\eta\phi(t_2,\underline{a})}\right\} = \prod_{i>i_2} \sum_{\substack{k=-(M-1)\\ k\ \text{odd}}}^{M-1} P_k\, e^{j2\pi hk[\iota q(t_1-iT)-\eta q(t_2-iT)]} \times$$

$$\prod_{i\leq i_2} \sum_{\substack{k=-(M-1)\\ k\ \text{odd}}}^{M-1} P_k\, e^{j\pi k\left(\frac{n-m}{M}\right)}. \tag{C.3}$$

As can be seen from (C.3), if $n-m$ is not a multiple of M, the limit of the second product of (C.3) goes to zero as i decreases. If however $n-m$ is a multiple of M, then the second product of (C.3) is one. Finally the smallest i for which $t_1-iT\leq 0$ is named i_1. Since $t_1\geq t_2$, t_2-iT will also be smaller than zero when $i\geq i_1$. Thus

$$\iota q(t-iT)-\eta q(t-iT)=0, \qquad i\geq i_1=\left\lfloor\frac{t_1}{T}\right\rfloor+1 \tag{C.4}$$

and therefore

$$\mathbb{E}\left\{e^{j\iota\phi(t_1,\underline{a})}\,e^{-j\eta\phi(t_2,\underline{a})}\right\}=\prod_{i>i_2}^{i<i_1}\sum_{\substack{k=-(M-1)\\ k\text{ odd}}}^{M-1}P_k\;e^{j2\pi hk[\iota q(t_1-iT)-\eta q(t_2-iT)]} \tag{C.5}$$

when $\iota+\eta$ multiple of M and 0 otherwise. Substituting the value of i_1 (C.4) and i_2 (C.2) into (C.5) gives the result of (3.2.14).

APPENDIX D

Squared Envelope Detector Autocovariance Function

To evaluate $\xi(t)$ autocovariance function, we start by looking at its autocorrelation. Using basic definition, we get

$$\begin{aligned} R_{\xi\xi}(t_1,t_2) = \mathbb{E}\Big\{\xi(t_1)\,\xi(t_2)^*\Big\} = \mathbb{E}\Big\{ & |b(t_1)|^2\,|b(t_2)|^2 + 2\,|b(t_1)|^2\,\Re\big[b(t_2)\,\gamma(t_2)^*\big] \\ & + |b(t_1)|^2\,|\gamma(t_2)|^2 + 2\,|b(t_2)|^2\,\Re\big[b(t_1)\,\gamma(t_1)^*\big] \\ & + 4\,\Re\big[b(t_1)\,\gamma(t_1)^*\big]\Re\big[b(t_2)\,\gamma(t_2)^*\big] + 2\,|\gamma(t_2)|^2\,\Re\big[b(t_1)\,\gamma(t_1)^*\big] \\ & + |\gamma(t_1)|^2\,|b(t_2)|^2 + 2\,|\gamma(t_1)|^2\,\Re\big[b(t_2)\,\gamma(t_2)^*\big] + |\gamma(t_1)|^2\,|\gamma(t_2)|^2\Big\}. \end{aligned} \tag{D.1}$$

As was mentioned in Chapter 3, $\mathbb{E}\Big\{b(t)\Big\}=\mathbb{E}\Big\{\gamma(t)\Big\}=0$ and $b(t)$ is independent of $\gamma(t)$, so the second, fourth, sixth and eighth terms of (D.1) are 0. The remaining terms will be studied individually in order to understand their effect in the summation. Starting with the first term

$$\mathbb{E}\Big\{|b(t_1)|^2\,|b(t_2)|^2\Big\} = \mathbb{E}\Big\{|c(t_1)|^{2M}|c(t_2)|^{2M}\Big\} \times \sum_{\substack{k=-(M-1)\\ k\ \text{even}}}^{M-1}\ \sum_{\substack{l=-(M-1)\\ l\ \text{even}}}^{M-1} 4D_k\,D_l\,\cos(2\pi f_k t_1)\cos(2\pi f_l t_2) \tag{D.2}$$

$$\simeq \mathbb{E}\Big\{|c(t_1)|^{2M}|c(t_2)|^{2M}\Big\}\,R_{dis}(t_1,t_1)\,R_{dis}(t_2,t_2),$$

with $f_k=\frac{k}{2T}$ and $f_l=\frac{l}{2T}$. This term represents the spectrum of the timing information signal amplitude modulated. It can be completely determined from the statistics of $c(t)$ and $u(t,\underline{a})$. The third and seventh (interchange t_1 and t_2) are simply

$$\mathbb{E}\Big\{|b(t_1)|^2\,|\gamma(t_2)|^2\Big\} = \mathbb{E}\Big\{|b(t_1)|^2\Big\}\,\mathbb{E}\Big\{|\gamma(t_2)|^2\Big\} \tag{D.3}$$

with both right side expectations given by (3.3.17) and (3.3.18). The fifth term can be rewritten as a

sum of 2 terms, i.e.,

$$\mathbf{E}\Big\{4\,\Re\big[b(t_1)\,\gamma(t_1)^*\big]\,\Re\big[b(t_2)\,\gamma(t_2)^*\big]\Big\} = \mathbf{E}\Big\{2\,\Re\big[b(t_1)\,b(t_2)^*\;\gamma(t_1)^*\gamma(t_2)\big]+2\,\Re\big[b(t_1)\,b(t_2)\;\gamma(t_1)^*\gamma(t_2)^*\big]\Big\}. \tag{D.4}$$

The first term in (D.4) left side is simply

$$\mathbf{E}\Big\{2\,\Re\big[b(t_1)\,b(t_2)^*\;\gamma(t_1)^*\,\gamma(t_2)\big]\Big\} = 2\,\Re\Big[\mathbf{E}\big\{b(t_1)\,b(t_2)^*\big\}\;\mathbf{E}\big\{\gamma(t_1)^*\,\gamma(t_2)\big\}\Big]$$

$$= 2\,\Re\big[R_{bb}(t_1,t_2)\;R_{\gamma\gamma}(t_1,t_2)^*\big], \tag{D.5}$$

because of independence, while the second term reduces to

$$\mathbf{E}\Big\{2\,\Re\big[b(t_1)\,b(t_2)\;\gamma(t_1)^*\,\gamma(t_2)^*\big]\Big\} = 2\,\Re\Bigg[\mathbf{E}\big\{|c(t_1)|^M|c(t_2)|^M\big\}\;\mathbf{E}\big\{e^{jM\theta(t_1)}\,e^{jM\theta(t_2)}\big\}\;\mathbf{E}\big\{\gamma(t_1)^*\,\gamma(t_2)^*\big\}$$

$$\times\sum_{\substack{n=-(M-1)\\ n\text{ odd}}}^{M-1}\;\sum_{\substack{m=-(M-1)\\ m\text{ odd}}}^{M-1} d_n d_m\; e^{j2\pi(f_n t_1+f_m t_2)}\Bigg]$$

$$= 0, \tag{D.6}$$

because the $\mathbf{E}\big\{e^{jM\theta(t_1)}\,e^{jM\theta(t_2)}\big\}=0$ [44]. So the fifth term of (D.1) is simply (D.5). Up to this point every term of $\xi(t)$ autocorrelation function can be computed from the autocorrelation function of the input $x(t)$. The last term of (D.1) is given by

$$\mathbf{E}\big\{|\gamma(t_1)|^2\,|\gamma(t_2)|^2\big\}, \tag{D.7}$$

and from the writer's knowledge, there is no analytical or exact numerical solution for the above expression. The problem is closely related to the problem of finding the autocorrelation function of the envelope of a CPM signal after filtering and nonlinear processing. It can be concluded, from this fact, that no exact expression can be given for the autocorrelation function of $\xi(t)$, and by the very fact, neither can an expression for the spectrum of $\xi(t)$ be given. However, the autocorrelation function of $\xi(t)$ can be written as

$$R_{\xi\xi}(t_1,t_2) = \mathbb{E}\Big\{|b(t_1)|^2\,|b(t_2)|^2 + |b(t_1)|^2\,|\gamma(t_2)|^2\Big\} + 2\Re\Big[R_{bb}(t_1,t_2)\;R_{\gamma\gamma}(t_1,t_2)^*\Big]$$

$$+ \mathbb{E}\Big\{|\gamma(t_1)|^2\,|b(t_2)|^2 + |\gamma(t_1)|^2\,|\gamma(t_2)|^2\Big\}. \tag{D.8}$$

Since $C_{\xi\xi}(t_1,t_2)=R_{\xi\xi}(t_1,t_2)-m_\xi(t_1)\,m_\xi(t_2)^*$, (3.3.15) can be used to get

$$C_{\xi\xi}(t_1,t_2) = C_{|b|^2|b|^2}(t_1,t_2) + 2\Re\Big[R_{bb}(t_1,t_2)\;R_{\gamma\gamma}(t_1,t_2)^*\Big] + C_{|\gamma|^2|\gamma|^2}(t_1,t_2). \tag{D.9}$$

The stationary version of (D.9) yields (3.3.18).

REFERENCES

[1] C.E. Shannon, "A mathematical theory of communication," *Bell Syst. Tech. Jour.*, vol. 27, pp. 379-423, July 1948.

[2] C.E. Shannon, "A mathematical theory of communication," *Bell Syst. Tech. Jour.*, vol. 27, pp. 623-656, October 1948.

[3] C.E. Shannon, "Communication in the presence of noise," *Proc. IRE*, vol. 37, pp. 10-21, January 1949.

[4] W.C.Y. Lee, *Mobile Communication Engineering*, McGraw-Hill, New-York, NY 1982.

[5] Special Issue on "Satellite cummunications toward the year 2000," *IEEE Jour. on Selected Areas in Comm.*, vol. SAC-5, no. 4, May 1987.

[6] R.W. Huck, "The Canadien MSAT program," Presented at the 1987 Satellite Communication Conference, San Paolo, Bresil. (Available at DOC, CRC Library).

[7] G.A. Arradendo, J.C. Feggeler, and J.I. Smith, "Voice and data transmission," *Bell Syst. Tech. Jour.*, vol. 58, no.1, pp. 97-123, January 1979.

[8] R.H. Clarke, "A statistical theory of mobile radio reception," *Bell Syst. Tech. Jour.*, vol. 47, pp. 957-1000, July 1968.

[9] M. Schwarty, W.R. Bennett, and S. Stein, *Communication Systems and Techniques, part III*, McGraw-Hill, New York, NY 1966.

[10] S.C. Gupta, R. Viswanathan, and R. Muammar, "Land mobile radio systems - A tutorial exposition," *IEEE Communications Magazine*, vol. 23, no. 6, pp. 34-45, June 1985.

[11] C.-E. Sundberg, "Continuous phase modulation," *IEEE Communications Magazine*, vol. 24, no.4, pp. 25-38, April 1986.

[12] J. Anderson, T. Aulin, and C.-E Sundberg, *Digital Phase Modulation*, Plenum, New York, NY 1986.

[13] H. Nyquist, "Certain topics in telegraph transmission theory," *Trans. AIEE*, vol. 47, pp. 617-644, April 1928.

[14] R. de Buda, "Coherent demodulation of frequency shift keying with low deviation ratio," *IEEE Trans. Commun.*, vol. COM-20, no. 6, pp. 429-435, June 1972.

[15] J.G. Proakis, *Digital Communications*, McGraw-Hill, New York 1983.

[16] N. Ekanayake, "*M*-ary continuous phase frequency shift keying with modulation index $1/M$," *IEE Proc., Part F, Communications, Radar and Signal Processing*, vol. 131, no. 2, pp. 173-178, April 1984.

[17] T. Aulin and C.-E. Sundberg, "Continuous phase modulation-Part I: Full response signaling," *IEEE Trans. Commun.*, vol. COM-29, no. 3, pp. 196-209, March 1981.

[18] T. Aulin, R. Rydbeck and C.-E. Sundberg, "Continuous phase modulation-Part II: Partial response signaling," *IEEE Trans. Commun.*, vol. COM-29, no. 3, pp. 210-225, March 1981.

[19] A. Papoulis, *Probability, Random Variables, and Stochastic Processes*, McGraw-Hill, New York 1984.

[20] O.B.P. Rikkert De Koe and P. Van der Wurf, "On some extensions of Nyquist's telegraph transmission theory," *Proc. IEEE*, vol. 57, pp. 701-702, April 1969.

[21] S. Pasupathy, "Nyquist's third criterion," *Proc. IEEE*, vol. 62, pp. 860-861, June 1974.

[22] B. Sayar and S. Pasupathy, "Nyquist 3 pulse shaping in continuous phase modulation," *IEEE Trans. Commun.*, vol. COM-35, no. 1, pp. 57-67, January 1987.

[23] B. Sayar, "Nyquist 3 pulse shaping in continuous phase modulation," M.A.Sc. thesis, Dep. Elec. Eng., Univ. Toronto, Toronto, Ont., Canada, December 1984.

[24] T. Aulin, G. Lindell, and C.-E. Sundberg, "Selecting smoothing pulses for partial-response digital FM," *IEE Proc., Part F, Communications, Radar and Signal Processing*, vol. 128, no. 4, pp. 237-244, August 1981.

[25] P. Galko and S. Pasupathy, "Linear receivers for correlatively coded MSK," *IEEE Trans. Commun.*, vol. COM-33, no. 4, pp. 338-347, April 1985.

[26] F. de Jager and C. B. Dekker, "Tamed frequency modulation, a novel method to achieve spectrum economy in digital transmission," *IEEE Trans. Commun.*, vol. COM-26, no. 5, pp. 534-542, May 1978.

[27] K. S. Chung and L.E. Zegers, "Generalized tamed frequency modulation," *Philips J. Res.*, vol. 37, no. 4, pp. 165-177, 1982.

[28] K.S. Chung, "Generalized tamed modulation and its application for mobile radio communications," *Jour. on Selected Areas in Comm.*, vol. 2, no. SAC-4, pp. 487-497, July 1984.

[29] P. Galko, "Signal modelling and coding for linearly detectable CPM," To appear in the *Journal of the Franklin Institute.*

[30] H.L. Van Trees, *Detection, Estimation, and Modulation, part III* , John Wiley & Sons, New York 1971.

[31] R.R. Anderson and J. Salz, "Spectra of digital FM," *Bell Syst. Tech. Jour.*, vol. 44, pp. 1165-1189, July-August 1965.

[32] H.E. Rowe, and V.K. Prabhu, "Power spectrum of a digital frequency-modulation signal," *Bell Syst. Tech. Jour.*, vol. 53, no. 6, pp. 1095-1125, July-August 1975.

[33] T. Aulin and C.-E. Sundberg, "Calculating digital FM spectra by means of autocorrelation," *IEEE Trans. Commun.*, vol. COM-30, no. 5, pp. 1199-1208, May 1982.

[34] T. Aulin and C.-E. Sundberg, "An easy way to calculate power spectrum of digital FM," *IEE Proc., Part F, Communications, Radar and Signal Processing*, vol. 130, no. 6, pp. 519-526, October 1983.

[35] H.L. Hurd, "Stationarizing properties of random shifts," *SIAM Jour. Appl. Math.*, vol. 26, no. 1, pp. 203-212, January 1974.

[36] S.G. Glišić, "Symbol synchronization in digital communication systems using partial response CPM signaling," *IEEE Trans. Commun.*, vol. COM-37, no. 3, pp. 298-308, March 1989.

[37] T. Aulin and C.-E. Sundberg, "Synchronization properties of continuous phase modulation," *Proc. Global Telecommunications Conference*, Miami, FL, USA, pp. D7.1.1-D7.1.7, November 1982.

[38] A.N. D'Andrea, U. Mengali, and R. Reggiannini, "Carrier phase and clock recovery for continuous phase modulated signals," *IEEE Trans. Commun.*, vol. COM-35, no. 10, pp. 1095-1101, October 1987.

[39] M. Moeneclaey, "The influence of cycle slipping on the error probability of a PAM receiver," *IEEE Trans. Commun.*, vol. COM-35, no. 9, pp. 961-968, September 1987.

[40] J.R. Ball, "A real-time fading simulator for mobile radio," *The Radio and Electronic Engineer*, vol. 52, no. 10, pp. 475-478, October 1982.

[41] P.A. Bello, "Aeronautical channel characterization," *IEEE Trans. Commun.*, vol. COM-21, no. 5, pp. 548-563, May 1973.

[42] F.M. Gardner, "Self-noise in synchronizers," *IEEE Trans. Commun.*, vol. COM-28, no. 8, pp. 1159-1103, August 1980.

[43] T.T. Fang, "I and Q decomposition of self-noise in square-law clock regenerators," *IEEE Trans. Commun.*, vol. COM-36, no. 9, pp. 1044-1052, September 1988.

[44] K.S. Miller, *Complex Stochastic Processes: An introduction to theory and application*, Addison-Wesley, 1974.

[45] K.S. Miller, "Moments of complex Gaussian processes," *Proc. IEEE*, vol. 56, no. 1, pp. 83-84, January 1968.

[46] A.V. Oppenheim and R.W. Schafer, *Digital Signal Processing*, Prentice-Hall, 1975.

[47] R.E. Crochiere and L.R. Rabiner, "Interpolation and decimation of digital signals—A tutorial review," *Proc. IEEE*, vol. 69, no. 3, pp. 300-331, March 1981.

[48] R.E. Crochiere and L.R. Rabiner, *Multirate Digital Signal Processing*, Prentice-Hall, 1983.

[49] Texas Instrument, *Linear Circuits Data Acquisition and Conversion*, Data book volume 2, 1989.